

Politecnico di Torino

Department of Mechanical and Aerospace Engineering
Master Degree Course in Aerospace Engineering

Master's Degree Thesis

Experimental characterization of Vortex Gust using Event-Based Imaging Velocimetry

Supervisors:
Prof. Gioacchino Cafiero
Eng. Sara Montagner

Candidate:
Gabriele Papalia
Matr.: 327851

July 2026

Abstract

In the recent decades, interest in Unmanned Aerial Vehicle (UAV) technology has grown significantly, making the study of gust encounters a prominent research topic. Since these vehicles operate at low altitudes, they are constantly exposed to highly non-uniform and unsteady flows characterized by severe atmospheric disturbances, such as vortex gusts. They can severely affect flight stability when the gust velocity exceeds the free-stream velocity; here the ratio between these two quantities is denoted as the gust ratio. However, their characterization has so far been investigated only in water towing tanks or modelled numerically; to fill the gap, the present work introduces a new experimental set-up designed to generate isolated vortex gusts in a wind tunnel.

A 180° clockwise rotation of a flat plate — which is the vortex gust generator — causes vortex shedding from both the leading and trailing edges. The study focuses exclusively on the characterization of the vortex shed from the trailing edge, which was found to be a coherent structure. On the other hand, the second vortex released from the leading edge was found to be weak and unstructured. The experimental campaign was conducted by varying the free-stream velocity across three different values, while keeping the rotation speed of the gust generator constant. The experimental set-up proved capable of generating repeatable experiments. The characterization of the vortex gust was performed through time-resolved *Event-Based Imaging Velocimetry* (EBIV) technique; by varying the free-stream velocity, three different gust ratios were achieved, simulating conditions from mild to severe gust. The obtained results show that the gust ratio decreases as the free-stream velocity increases. Therefore, the free-stream velocity directly affects the intensity of the vortex.

To further examine the aerodynamic impact in applications, a flat plate equipped with five pressure sensors properly synchronized with the Event-Based cameras, was positioned downstream of the vortex gust generator to analyze the interaction of the isolated vortex gust with the boundary layer. The deployed set-up allows to properly sample the vortex evolution, thus confirming that it will represent a suitable platform to study the aerodynamic interaction of vortex gusts on aerodynamic surfaces.

Contents

Abstract i

List of Figures iv

List of Tables viii

List of Symbols ix

List of Acronyms x

Introduction 1

1 Physical framework of atmospheric gusts 2
- 1.1 Introduction to the problem . . . 2
- 1.2 Atmospheric Boundary Layer . . . 3
- 1.3 The UAV Operational Environment . . . 3
- 1.4 Classification of the gust types . . . 5
  - 1.4.1 Characterization Parameters . . . 6
  - 1.4.2 Streamwise gust . . . 7
  - 1.4.3 Transverse gust . . . 7
  - 1.4.4 Vortex gust . . . 8
- 1.5 Theoretical background . . . 9
- 1.6 Gust generation: current state-of-the-art . . . 11
  - 1.6.1 Test Facilities . . . 11
  - 1.6.2 Techniques for Gust Generation . . . 12
- 1.7 Identification of the research gap . . . 14

2 Event-Based Imaging Velocimetry 16
- 2.1 Introduction . . . 16
  - 2.1.1 Operating principles between FB and EB sensors . . . 17
  - 2.1.2 Rewards of Event Cameras . . . 18
  - 2.1.3 Drawbacks of Event Cameras . . . 18
- 2.2 Event generation basis and signal processing . . . 19
  - 2.2.1 Latency in EBV Sensors . . . 21
- 2.3 Processing of event-data . . . 21

3 Experimental set-up **23**
3.1 Wind tunnel and vortex gust generator . . . 23
3.2 Control and acquisition systems . . . 24
3.3 Flowfield measurements . . . 27
3.3.1 Triggering . . . 30
3.3.2 Image processing for vortex characterization . . . 30
3.4 Pressure acquisition system . . . 31
3.4.1 Image Processing for vortex–aerodynamic surface interaction . 33

4 Facility characterization **35**
4.1 Hot-wire calibration for flow characterization . . . 35
4.2 Flow field characterization . . . 36
4.3 Optimization actuation system . . . 38

5 Experimental results **41**
5.1 Elliptical Lamb-Oseen Vortex Model . . . 41
5.1.1 Model formulation . . . 42
5.1.2 Vortex centre detection and initial parameter estimation . . . 43
5.1.3 Model Fitting and Optimisation . . . 43
5.1.4 Circulation measurments . . . 44
5.2 Isolated Vortex Gust . . . 45
5.2.1 Results overview . . . 46
5.2.2 Model validation . . . 57
5.3 Vortex-aerodynamic surface interaction . . . 59
5.3.1 Data post-processing . . . 59
5.3.2 Results . . . 62

6 Conclusions **72**

Bibliography **73**

List of Figures

1.1 Gusts in the Atmospheric Boundary Layer (ABL) from [1]. 4
1.2 Trendlines shows how the turbulence intensity descreases with freestream velocity along all directions [7]. 4
1.3 Temporal variation of the overall pitch angle from [7]. 5
1.4 Temporal variation of the overall pitch angle from [7]. 6
1.5 Streamwise gust frame from [2]. 7
1.6 Transverse gust frame from [2]. 8
1.7 Vortex gust frame from [2]. 8
1.8 Two-dimensional frame of the experimental set-up. 11
1.9 Sketch for vortex gusts generation carried out by [13, modified]. . . . 13
1.10 Sketch for transverse gusts generation carried out by [3, modified]. . . 13
1.11 Sketch for vertical and longitudinal gusts generation carried out by [23, modified]. 14

2.1 Comparison on operating principles between frame-based and event-based cameras [29]. 17
2.2 Simplified schematic of an Event-Based Vision pixel and associated signals processing at each step [31]. 19
2.3 Sketch of the event generation process for a single pixel of the sensor: **(1)** time-varying intensity Gaussian signal seen by the photodiode, **(2,3)** log intensity signal, **(4)** asynchronous event stream produced by the pixel. 20
2.4 Histograms of recorded event times for pulsed-EBIV measurements. The green lines indicate the actual time and width of the laser trigger pulses. The top row (a, b) shows a random sample within the record , whereas the lower row (c, d) provides the averaged temporal distribution of events. The vertical red line marks the peak of the event distribution [31]. 21

3.1 Isometric view of the wind tunnel facility and experimental vortex-gust generator setup. 23
3.2 Isometric view of vortex-gust generator. 24
3.3 Feedback loop line: the encoder digital signals flows to the DAQ through TTL sensors, which transform the differential quadrature signals into a single-ended quadrature signals. 25
3.4 Architectural scheme of the Control System and the Acquisition System for the experimental set-up. 26

3.5 Side (top) and upper (bottom) views of the vortex gust generator and EBIV set-up for the characterization of the isolated vortex gust. . . . 28
3.6 Overall field of view of both cameras; the region within dashed lines represents the overlapped region (left). Cross-correlation map $\gamma(\Delta x, \Delta y)$ between cameras (right). 29
3.7 Merged raw pseudo-snapshot of the flow field captured by the (two) event cameras vertical stacked at a laser pulsing frequency of 500 Hz and $U_\infty \approx 1\,\mathrm{ms}^{-1}$. White spots illustrates the distribution of HFSB acting as flow tracers. 29
3.8 Timing diagram of the acquisition system for synchronization among trigger, laser and event-based cameras. 30
3.9 Side view (top) of the vortex gust generator and the pressure acquisition system. Upper side (bottom) of the flat plate equipped with 5 pressure sensors. It is worth noting that the high-frequency transducers are located in streamwise direction in the centreline. 32
3.10 Representative raw seeding images before (top) and after (bottom) the stitching procedure. 33

4.1 Calibration curve for the hot-wire probe. 35
4.2 For each plane (i.e., x_1, x_2 and x_3), a grid of 55 measurement points was acquired to monitor both flow uniformity and turbulence levels ($t_s = 45$ s, $f_s = 10$ kHz). The vertical measurement points (y_1 to y_5) were spaced 5 cm apart, with y_5 being the closest coordinate to the wind tunnel lower wall. 36
4.3 Profiles of mean velocity U (top, within each subfigure) and turbulence intensity u'/U (bottom, within each subfigure) at three axial planes x_1, x_2, x_3. Furthermore, other tests were performed respectively at $U_{\infty,hw} \approx 3\,\mathrm{ms}^{-1}$ and $U_{\infty,hw} \approx 3.5\,\mathrm{ms}^{-1}$ only for the first longitudinal plane x_1 (i.e., 85 cm downstream the test section inlet) and for both cases, the level of TI was found to be $< 5\%$. Ambient conditions: $T_{amb} = 20$ °C, $\rho_{amb} = 1.225$ kg/m^3. 37
4.4 Dynamic response $\varphi(t)$ of the system during the optimization campaign. Each trajectory is time-shifted and aligned to the origin to evaluate the repeatability of the motor's dynamic response. 38
4.5 Flowchart of the decoding algorithm for dynamic response. Rotation direction is determined by the phase lead between A and B. If A leads over B the rotation will be clockwise (CW), otherwise will be counterclockwise (CCW). PPR represents the pulse per revolution. . 39

5.1 Normalized out of plane vorticity contourplots at the coordinate $x/c = 0.6$: comparison between the experimental phase-averaged field (top, one velocity vector plotted every 4 grid points) and the fitted elliptical model (bottom) for $U_\infty \approx 1.0\,\mathrm{ms}^{-1}$ and $Re \approx 2 \times 10^4$. 47
5.2 Normalized longitudinal gust velocity U_g/U_∞ (•) and normalized transversal gust velocity V_g/U_∞ (•) at $x/c = 0.6$ for $U_\infty \approx 1.0\,\mathrm{ms}^{-1}$ and $Re \approx 2 \times 10^4$. 48

5.3 Experimental and numerical gust ratio $GR(\vartheta)$ (top) and normalized vortex core diameter D_c/c (bottom) during their spatio-temporal evolution for $U_\infty \approx 1.0\,\mathrm{ms}^{-1}$ and $Re \approx 2 \times 10^4$. 49
5.4 Normalized out of plane vorticity contourplots at $x/c = 0.6$: comparison between the experimental phase-averaged field (top, one velocity vector plotted every 4 grid points) and the fitted elliptical model (bottom) for $U_\infty \approx 1.4\,\mathrm{ms}^{-1}$ and $Re \approx 2.8 \times 10^4$. 50
5.5 Normalized longitudinal gust velocity U_g/U_∞ (▲) and normalized transversal gust velocity V_g/U_∞ (▲) at $x/c = 0.6$ for $U_\infty \approx 1.4\,\mathrm{ms}^{-1}$ and $Re \approx 2.8 \times 10^4$. 51
5.6 Experimental and numerical gust ratio $GR(\vartheta)$ (top) and normalized vortex core diameter D_c/c (bottom) during their spatio-temporal evolution for $U_\infty \approx 1.4\,\mathrm{ms}^{-1}$ and $Re \approx 2.8 \times 10^4$. 52
5.7 Normalized out of plane vorticity contourplots at $x/c = 0.6$: comparison between the experimental phase-averaged field (top, one velocity vector plotted every 4 grid points) and the fitted elliptical model (bottom) for $U_\infty \approx 1.8\,\mathrm{ms}^{-1}$ and $Re \approx 3.6 \times 10^4$. 53
5.8 Normalized longitudinal gust velocity U_g/U_∞ (■) and normalized transversal gust velocity V_g/U_∞ (■) at $x/c = 0.6$ for $U_\infty \approx 1.8\,\mathrm{ms}^{-1}$ and $Re \approx 3.6 \times 10^4$. 54
5.9 Experimental and numerical gust ratio $GR(\vartheta)$ (top) and normalized vortex core diameter D_c/c (bottom) during their spatio-temporal evolution for $U_\infty \approx 1.8\,\mathrm{ms}^{-1}$ and $Re \approx 3.6 \times 10^4$. 55
5.10 Evolution of gust ratio $GR(\vartheta)$ (top), vortex core diameter D_c/c (middle), and vortex core center trajectories (bottom) across all flow conditions. 56
5.11 Evolution of non-dimensionalized circulation $\Gamma/(cU_\infty)$ and its relative error ε_Γ for the following speeds: $U_\infty \approx 1.0\,\mathrm{ms}^{-1}$ (●, ●), $U_\infty \approx 1.4\,\mathrm{ms}^{-1}$ (▲, ▲) and $U_\infty \approx 1.8\,\mathrm{ms}^{-1}$ (■, ■). 58
5.12 Relative error for gust ratio computed for $U_\infty \approx 1.0\,\mathrm{ms}^{-1}$ (●), $U_\infty \approx 1.4\,\mathrm{ms}^{-1}$ (▲) and $U_\infty \approx 1.8\,\mathrm{ms}^{-1}$ (■). 60
5.13 Pressure coefficient $c_p(t^*)$ for gust ratios $GR_{\mathrm{exp}}(\vartheta) = 1.295$. 63
5.14 Pressure coefficient $c_p(t^*)$ for gust ratios $GR_{\mathrm{exp}}(\vartheta) = 1.197$. 64
5.15 Pressure coefficient $c_p(t^*)$ for gust ratios $GR_{\mathrm{exp}}(\vartheta) = 1.003$. 64
5.16 Normalized pressure coefficient $\Delta C_p(t^*)/C_{p_0}$ for various gust ratios. The markers (●, ▲, ■) represents the absolute and local maximum values for each of gust ratios. 65
5.17 Slice of $\bar{U}/U_\infty$ and $\bar{V}/U_\infty$ (left) for $GR_{\mathrm{exp}} = 1.295$ at $t^* = 0.79$. Black solid and dashed lines are isolines of positive and negative vorticity ($\omega c/U_\infty$), respectively. It is possible to visualize the vorticity due to the recirculation bubble; its interaction with the vortex core is the physical cause for the second local peak of the integrated pressure coefficient. 66
5.18 Paths of vortex gust for various gust ratios when it encounters an aerodynamic surface, where its leading edge is located at $\Delta y/c = -0.45$. 68

5.19 Normalized out of plane vorticity contourplots $\omega c/U_\infty$ and slice of $\bar{U}/U_\infty$ and $\bar{V}/U_\infty$ (left) for $GR_{\text{exp}} = 1.295$ at $t^* = 1.12$. Black solid and dashed lines are isolines of positive and negative vorticity, respectively. 69
5.20 Normalized out of plane vorticity contourplots $\omega c/U_\infty$ and slice of $\bar{U}/U_\infty$ and $\bar{V}/U_\infty$ (left) for $GR_{\text{exp}} = 1.197$ at $t^* = 1.26$. Black solid and dashed lines are isolines of positive and negative vorticity, respectively. 70
5.21 Normalized out of plane vorticity contourplots $\omega c/U_\infty$ and slice of $\bar{U}/U_\infty$ and $\bar{V}/U_\infty$ (left) for $GR_{\text{exp}} = 1.003$ at $t^* = 1.37$. Black solid and dashed lines are isolines of positive and negative vorticity, respectively. 71

List of Tables

3.1 Positions of the 5 pressure transducers on the sensing flat plate, expressed relative to the origin of the reference frame. c is the chord of the gust generator. 31
3.2 Summary of the components for EBIV and pressure acquisition and synchronization. 34

4.1 Grid of measurement points in the y–z plane, common to the three planes $x_i = 85$, 115, and 145 cm ($i = 1, \ldots, 3$), where x is measured from the test section inlet. 40

5.1 Experimental test matrix for vortex gust characterization. 45
5.2 Comparison among vortex gust characterization results for all experiments. 46
5.3 RMSE for the different analyzed inflow conditions. 59
5.4 Summary of the first local pressure coefficient peaks and corresponding maximum effective local angle of attack at the leading edge. . . . 66

List of Symbols

Symbol	Description	Unit (SI)
AR	wing aspect ratio; b/c	-
b	wing span	m
c	wing chord	m
D_c	gust width (vortex core diameter)	m
GR	gust ratio; u_ϑ/U_∞	-
Re	Reynolds number; $U_\infty c/\nu$	-
t	time	s
t^*	convective time; $U_\infty t/c$	-
U_g	longitudinal gust velocity	ms^{-1}
U_p	peak longitudinal gust velocity	ms^{-1}
U_∞	freestream velocity	ms^{-1}
u_ϑ	maximun tangential gust velocity	ms^{-1}
V_g	transverse gust velocity	ms^{-1}
V_p	peak transverse gust velocity	ms^{-1}
Γ	circulation inside the elliptical core	$\mathrm{m}^2\mathrm{s}^{-1}$
ω	vorticity	s^{-1}

List of Acronyms

Acronym	Description
ABL	Atmospheric Boundary Layer
AER	Address Event Representation
BA	Background Activity
CC	Cross-Correlation
CCA	Constant Current Anemometer
CTA	Constant Temperature Anemometer
DAQ	Data Acquisition
EBIV	Event-Based Imaging Velocimetry
FOV	Field of View
HDR	High Dynamic Range
HFSB	Helium-Filled Soap Bubbles
HWA	Hot-Wire Anemometer
LESP	Leading Edge Suction Parameter
MAVs	Micro Air Vehicles
PAS	Pressure Acquisition System
PIV	Particle Image Velocimetry
PLA	Polylactic Acid
RMSE	Root Mean Square Error
TI	Turbulence Intensity
TTL	Transistor-Transistor Logic
UAVs	Unmanned Aerial Vehicles

Thesis outline

Vortex gust generation can be cumbersome. Generally speaking, the current state-of-the-art involves vortex gust generated using towing tanks facilities. To generate the vortex gust in a wind tunnel is a complex challenge. This work aims to close this gap and establish a bridge among the test facilities that are used currently and the future development for wind tunnel. This thesis is subdivided as follows:

- in the first chapter a general theoretical background is presented, with a main focus on the vortex gust;
- in the second chapter, the deployed measurment technique, nameli the Event-Based Imaging Velocimetry is presented;
- in the third chapter the experimental set-up is presented, with a detailed description of the test facility;
- the fourth chapter presents the results of characterization of the flow field for the wind tunnel. Furthermore, the optimization for the actuation system will be presented;
- the fifth chapter reports the experimental results;
- the last chapter explain the conclusion of this present work.

I hereby declare the use of Claude (Anthropic, 2026) as a support tool for optimizing the data processing code. Every generated output was subsequently verified and manually validated by the author.

Chapter 1

Physical framework of atmospheric gusts

This first chapter aims to briefly describe some fundamental concepts concerning the physical framework of atmospheric gusts. Firstly, a short introduction to the general problem explaining the context will be presented. Then, a short description of the different type of gusts will be presented. Furthermore, a general overview about the current state-of-the-art in the gust generation field will be introduced, and finally, the identification of the research gap will be offered in order to better understand the main goal of this present work.

1.1 Introduction to the problem

The Aviation Industry is rooted in the early 1900s, when the Wright brothers were able to make the first successful flight in human history, which ended soon because of a gust. The gust encounters were already a crucial issue back in the days that needed to be studied.

Later, the two World Wars shifted the core of aviation business towards the military field at first and then in civil sector. In these fields, flying in clear air became the standard. For conventional transport aircraft, regular wind gusts and atmospheric turbulence came to be regarded as relatively small and manageable disturbances [1]. In fact, for the conventional aviation, turbulence has typically been treated using statistical or averaged models that assume small deviations from a steady reference flow [2].

In the 1990s, interest in Unmanned Aerial Vehicle (UAVs) technology has grown significantly for intelligence tasks, reconnaissance, delivery and logistics support [1]. Because these vehicles fly at relatively low speeds and altitude, they often operate in conditions where atmospheric gusts are of the same order of magnitude as the vehicle's flight speed. In this regime, gusts cannot be viewed as simple small perturbations; instead, they can trigger extensive flow separation and the formation of energetic vortical structures over the lifting surfaces [2]. Urban environments present an especially challenging setting for such vehicles. When wind interacts with densely packed buildings, it generates highly complex and unsteady airwakes, characterized by strong velocity gradients, recirculating regions, and coherent flow structures [3].

It is therefore absolutely necessary to guarantee safe flights within complex airspace, without compromising people's safety. Thus, the problem of gust encounters and the study of highly unsteady flows are a trend topic nowadays. Among the various gust types encountered in real-world conditions, vortical gusts represent one of the most severe and least understood disturbances from an experimental perspective. The present thesis indeed focuses on the development of a novel experimental set-up for the controlled generation of vortical gusts for a deep investigation of the physical phenomena.

1.2 Atmospheric Boundary Layer

Before diving deep into the current state-of-the-art in gust generation techniques, it is important to highlight the metereological context within the UAVs operate.

Most of the highly non uniform and unsteady flows in atmosphere occur in the Atmospheric Boundary Layer (ABL), which extends up to 1-2 km of height [4]. Since UAVs operate entirely within the ABL, they are continuously subjected to these complex aerodynamic phenomena and for this reason it important to study the gust encounters. Yet, with the rise of severe storms, gusts may have economic and social impact [1]. Thus, in recent decades, the study of gust encounters has emerged as a prominent research topic from both a financial and engineering (i.e, numerical and experimental) wise. Generally speaking, a common approach adopted to model gusts is based on the estimation of the gust ratio, which is the ratio between the gust speed and the freestream velocity. Meteorological data indicate that the scales of unsteady flows in storms vary widely. For instance, high variability is observed in convective wind gusts and urban wind comfort assessments, where gust ratio typically range between 1 and 4 [5]. The fig. 1.1 shows how the orography has a direct impact on gusts formation. The thickness of the ABL increases with surface roughness, expanding progressively from rural landscapes to suburban and densely built urban centers. In these environments, both meteorological conditions and topographic features dictate flow separation and wake shedding. Consequently, unsteady separated flows are prevalent across diverse environments, including mountain ridges, coastal zones, urban areas, and the wakes of large anthropogenic structures.

Furthermore, Abdulghani et al. [4] have demonstrated that the urban environments generate such a wide turbulence spectrum that contains a huge range of lengths and scales. Specifically, urban environments give rise to coherent structures characterized by the same lengthscale of the buildings. Yet, suburban environments lead to homogeneous turbulence. This overall framework highlights the complexity of the operational airspace and underscores why studying it is so crucial.

1.3 The UAV Operational Environment

The operational envelope of air vehicles is strictly limited by structural loads during gust encounters. The most critical hazards are short-scale, highly unsteady flows, which generate large transient airloads. This is especially true during complex maneuvers like search-and-rescue in mountainous terrain or naval ship-deck landings.

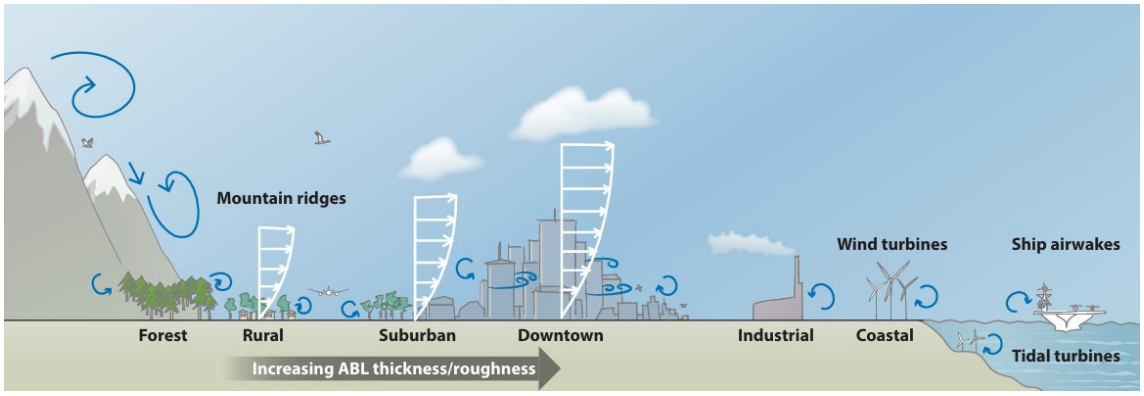


Figure 1.1: Gusts in the Atmospheric Boundary Layer (ABL) from [1].

Because UAVs have chord lengths and stall speeds approximately one-tenth (1/10) [6] those of manned aircraft, they are uniquely vulnerable to shed vortices and shear layers. Consequently, operating in urban canyons or structural wakes exposes these smaller vehicles to severe, multi-axis gusts across multiple timescales, tightly defining their safety limits [1].

However, Watkins et al. [7] demonstrated how the freestream velocity (i.e., the vehicle speed relative to the wind speed) provide a positive influence on the measured turbulence intensity. In fact, the more the relative speed increase, the less will be the turbulence intensity, as shown by the trendlines in fig. 1.2. This explains why an UAV facing atmospheric turbulence at a given forward speed experiences lower effective pitch and roll disturbances than it would when maintaining a stationary hover under identical wind conditions.

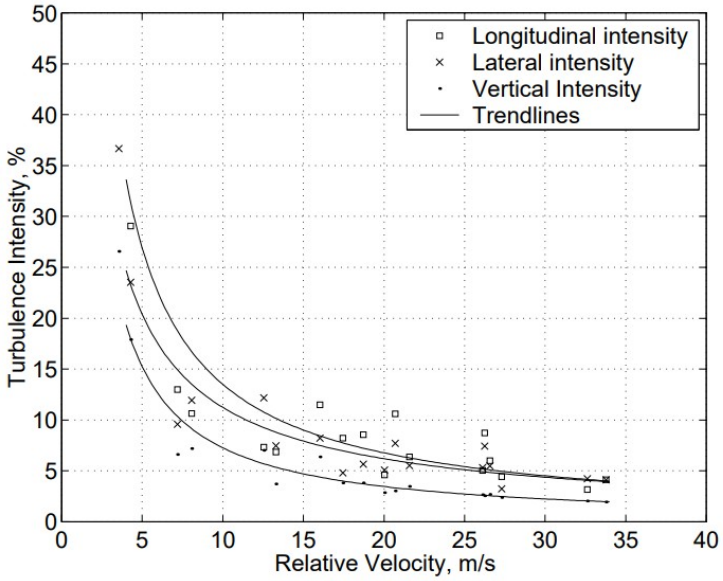


Figure 1.2: Trendlines shows how the turbulence intensity descreases with freestream velocity along all directions [7].

Another key factor that need to be analyzed is the effect of gusts on pitch vari-

ation. As a gust impacts the leading edge of a wing, the flow angle and velocity are altered, inducing variations in the load distribution. According to Abdulghani et al. [4] a large (i.e., the gust size is comparable with the length of the wing) gust induce heaving perturbation whenever it encounters a wing; yet a gust smaller than wingspan induce rolling perturbation. Watkins et al. [7] not only show how is relevant the absolute effect of gusts on pitch angle variation, but they demonstrate how strong is the effect of the direction. They carried out a campaign test by using 4 probes with a lateral separation of 50 mm from each other. At first glance, if we take a look at the overall variation of the pitch angle (fig. 1.3), it might seems that there is a strong correlation among all probes, showing a variation of $\pm 10°$.

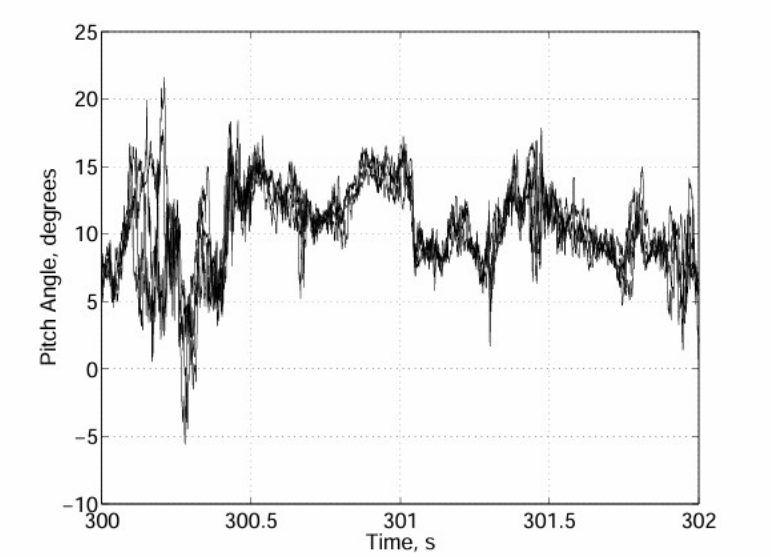


Figure 1.3: Temporal variation of the overall pitch angle from [7].

However, a closer esamination of the same sampling data in a restricted region (fig. 1.4) shows how there are such a great differences (up to $\approx 15°$ between the second and third probe) among sensors, showing up the relevance of the wind (i.e., the gust) direction.

1.4 Classification of the gust types

According to Jones et al. [1], a "gust" is simply a flow structure, which is a combination of shear layers, coherent vortices and turbulence, that exists in the environment and causes unsteadiness in the flow.

To study unsteady aerodynamic interactions in a clear and systematic way, it is helpful to first classify the types of disturbances that a lifting surface can experience. Although atmospheric turbulence is a complex, three-dimensional, and inherently random phenomena, researchers often represent it using simpler two-dimensional models. Within this framework, three main types of gusts are commonly identified: streamwise, transverse, and vortical with a remarkable attention to the last one [2]. Each of these gusts has distinct physical features and poses different challenges to flight stability.

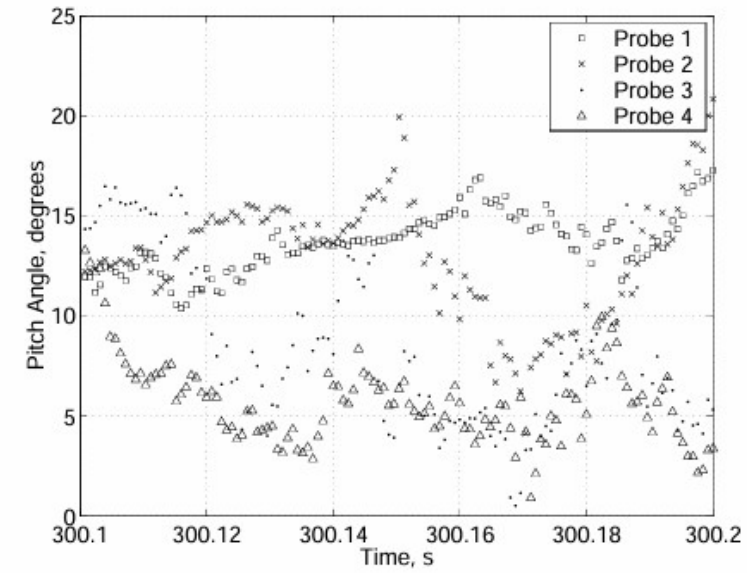


Figure 1.4: Temporal variation of the overall pitch angle from [7].

1.4.1 Characterization Parameters

To provide a rigorous analytical framework, it is necessary to move beyond the qualitative description of atmospheric disturbances and establish a set of non-dimensional parameters that govern the interaction. A discrete gust encounter is defined as a temporary deviation from steady flight conditions, caused by an external disturbance in the airflow rather than by the motion of the wing itself.

The most critical factor in determining the severity of this encounter is the gust ratio [8], defined as follows

$$GR \doteq \frac{u_\vartheta}{U_\infty} \tag{1.1}$$

where u_ϑ is the maximum gust velocity and U_∞ represents the free-stream velocity. In our context, the U_∞ might be interpreted as the vehicle's forward airspeed. This parameter serves as the primary threshold for aerodynamic linearity; while a ratio $GR \lesssim 0.1$ allows the flow to be approximated as a small perturbation, higher values indicate a regime dominated by massive flow separation and the emergence of nonlinear vortical structures that violate the assumptions of classical potential flow [2]: in this case, when $GR \geq 1$, we refer to extreme aerodynamics [9].

In addition to the size of the gust, the spatial scale of the event is described by the encounter width [2]

$$W_e \doteq \frac{w}{c} \tag{1.2}$$

which compares the gust's width w to the wing chord c, see also fig. 1.6. This ratio determines how the wing responds to the incoming airflow: very narrow gusts are often smoothed out by the wing's inertia, while very wide gusts cause a response similar to steady flow. The most difficult unsteady forces happen when the gust width is about the same as the chord, because the forces then become very sensitive to how vorticity develops and moves. Moreover, these forces don't depend only on the gust's maximum strength; they are also influenced by the gust's speed profile

and how quickly the wing moves through it. These factors control the effective pitch rate and the history of the wing's angle of attack, which are key to predicting the timing and size of peak loads.

1.4.2 Streamwise gust

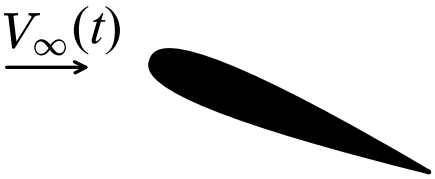


Figure 1.5: Streamwise gust frame from [2].

The first canonical type involves fluctuations along the direction of travel, where a stationary lifting surface encounters variations in longitudinal velocity as outlined in fig. 1.5. In this case, the inflow angle remains essentially constant, so the aerodynamic response is driven mainly by changes in dynamic pressure and the unsteady boundary layer, rather than sudden shifts in angle of attack [2]. Rapidly changing the flow speed in a wind tunnel is difficult, so researchers often move the wing through a stationary flow to mimic velocity changes [10]. This approach works but requires corrections for fluid inertia (added mass) and the missing pressure gradients of an accelerating freestream [10]. Alternative facilities have been developed to generate streamwise gusts directly without displacing the model: active-grid wind tunnels and programmable devices such as the WindShaper [11] can modulate the local flow velocity in real time.

Since the effective angle of attack stays nearly constant, the boundary layer usually remains attached even at high velocity fluctuations. Still, viscous effects make the flow behavior complex, and predicting stall under these unsteady conditions is challenging. Modern separation criteria, like the Leading Edge Suction Parameter (LESP), help identify whether the flow remains attached or separates, which is crucial for designing active control systems to regulate forces [10].

1.4.3 Transverse gust

The second category covers disturbances acting perpendicular to the flight path, often called transverse or normal gusts as sketched in fig. 1.6. These occur when a wing passes through a localized updraft or strong shear layer—common in turbulent wakes behind large structures, near ships, or in the uneven winds of mountains and cities [2]. In research, these are usually modeled by keeping a rigid wing at constant pitch as it moves steadily into a defined vertical flow. Two velocity profiles are most

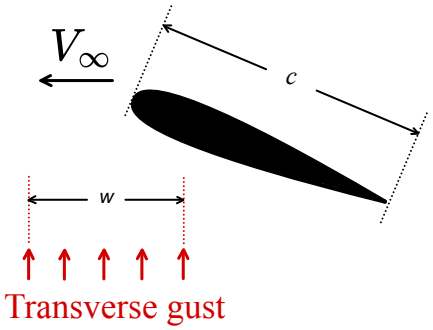


Figure 1.6: Transverse gust frame from [2].

commonly used: the top-hat, which follows classical theory, and the sine-squared (1-cosine), which better reflects how natural gusts develop gradually.

While the spatial extent of a gust is easy to define, measuring its intensity is more complex. Peak velocity is often used, since it sets the maximum angle of attack, but this alone can be misleading. Gusts with the same peak can produce different aerodynamic loads depending on their velocity distribution [2].

For instance, a top-hat and a sine-squared gust may trigger similar flow features, like the roll-up of a leading-edge vortex, but the rate of lift development differs. Comparing them by average velocity instead of peak brings the resulting lift closer, though the force progression remains profile-dependent. For moderate gusts, classical tools like the Küssner model work well, but at higher intensities, smooth sine-squared transitions are better captured than the abrupt changes of top-hat profiles [2].

1.4.4 Vortex gust

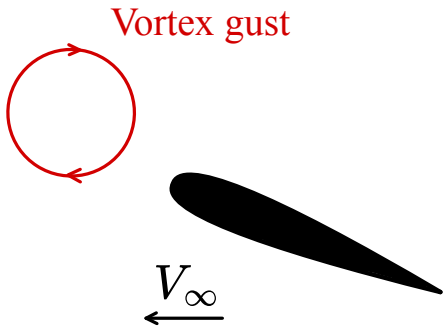


Figure 1.7: Vortex gust frame from [2].

Vortex gusts (fig. 1.7) occur when a vortex has a size comparable to the wing chord, creating strong and complex interactions with the wing. These phenomena are com-

monly observed in the wakes of other wings or rotor blades, such as in rotorcraft, wind and tidal turbines, or during formation flight. They also appear behind large structures like ships and buildings, and in naturally turbulent environments such as atmospheric flows. Recent studies have explored conditions of extreme aerodynamics of which $GR \geq 1$ that can emerge in urban canyons and severe atmospheric turbulence for MAVs [12].

Although idealized studies often consider a single, isolated vortex, real flows are usually irrotational, so vortices generally exist in pairs with opposite rotation. Much research has focused on vortices that are nearly two-dimensional, aligned with the leading edge of the wing, where the paired vortex is far enough away to have little effect [12].

The importance of vortex gusts [2, 9, 13, 14] for active control research lies in their richer set of governing parameters. Unlike a transverse gust, where the aerodynamic response is mainly dictated by the velocity distribution, the interaction with a vortex depends strongly on the exact path followed by its core as it moves toward the wing. In such conditions, the airfoil does not simply measure the incoming disturbance; instead, it actively influences the vortex trajectory. This two-way interaction implies that the induced flow field and the resulting aerodynamic loads are closely tied to how the vortex core approaches and evolves near the surface. When the core impinges on the leading edge, it can break apart or generate additional vortical structures, producing sudden and highly nonlinear load variations that are challenging to capture using conventional predictive approaches. In realistic atmospheric conditions, aircraft are often exposed to sequences of vortices with varying degrees of regularity. Nevertheless, studies indicate that analyzing the response to a single, well-defined transient event can offer valuable insight into the behavior observed in more complex, repeated encounters. For disturbances of limited strength, the resulting aerodynamic loads may be estimated by applying superposition principles. However, as the disturbance intensity grows, the recovery of the flow becomes increasingly dependent on how frequently these events occur. When the interval between successive disturbances is too short, the flow may not have sufficient time to reattach, resulting in persistent separation. For this reason, understanding how lift responds to both the strength of the vortex and its point of interaction with the wing is a fundamental step toward developing control strategies that remain effective under demanding aerodynamic conditions.

1.5 Theoretical background

Though this present work focuses on the generation of vortical gusts and interaction with aerodynamic surfaces, it is important to briefly introduce historical research on unsteady and highly non-uniform flows as well.

Generally speaking, it is possible to distinguish gusts in two big categories: discrete and continuous. For example, Federal Aviation Administration's defines gusts such as dicrete, simplifying in this way the approach to gust encounters for large airplanes. In the other hand, Dryden [15] and von Kármán [16] are became famous for their continuous turbulence model; specifically they described turbulence and unsteady flows such as stochastic process.

While inviscid linear models may vary in their application, they all include the same hypothesis of 2D thin aerodynamic airfoils, low angles of attack through the general assumption that the flow remains completely attached [1]. Although these methods have the limitation explained, they sketched the first path for numerical gust encounters modeling. Among the various mathematical functions used to describe how an airfoil responds to a sudden transverse gust, Miles's equation [17] is the most general. Specifically, he found a way to model a gust moving relative to an airfoil in a steady and uniform flow. By using a convolution integral, it is possible to combine the responses to multiple linear inputs and thus reconstruct the reaction to gusts of arbitrary shape. Miles's function includes a parameter λ that controls the gust velocity relative to the freestream. When $\lambda = 1$, the gust travels at the same speed and in the same direction as the freestream, which recovers the classical Küssner stationary gust scenario [18]. In this case, an airfoil entering a sharp-edged transverse gust experiences an effective change in camber (Sears and von Kármán [19]), and the circulatory lift can be expressed as $c_\ell = 2\pi w_0 \psi(s)/U_\infty$, where $\psi(s)$ is the Küssner function and s is the non-dimensional time

$$\psi(s) = \frac{1}{2\pi i} \int_{-\infty}^{\infty} \frac{C_g(k)}{k} e^{ik(s-1)} \, \mathrm{d}k$$

The Küssner function $\psi(s)$ is obtained by integrating the modified gust Theodorsen function $C_g(k)$ over all reduced frequencies $k = \omega b/U_\infty$, where $b = c/2$. The function $C_g(k)$ combines the Theodorsen function $C(k)$ with Bessel functions, and the gust velocity is estimated as a downwash $w_0 = -U_\infty \alpha$.

Miles's equation generalises this framework through the parameter λ. For $\lambda = -1$ the gust approaches from the trailing edge; for $\lambda = 0$ the model recovers Wagner's function [20], which describes the circulatory lift $c_\ell = -2\pi w_0 \phi(s)/U_\infty$

$$\phi(s) = \frac{1}{2\pi i} \int_{-\infty}^{\infty} \frac{C(k)}{k} e^{iks} \, \mathrm{d}k$$

due to a sudden change in angle of attack. For nonzero λ, the equation can model nonstationary gusts produced by upstream bodies or wakes. Recent studies have shown that Küssner's stationary-gust model is adequate for sharp-edged gusts without large-scale flow separation, though it loses accuracy for wide gusts ($w \approx c$) at high gust ratios [13].

For longitudinal gusts, an expansion of the Theodorsen's formulation to sinusoidal velocity variations and is valid as long as flow remains attached [1].

Vortex gusts are intrinsically more complex, as a passing vortex induces velocities in both directions simultaneously. Von Kármán and Sears [19] addressed combined transverse and arbitrary small motions. From the experimental perspective, it is tough generate vortical gusts and study their interaction with aerodynamic surfaces. To date, their characterization has relied almost exclusively on numerical simulations, like Fukami et al. did [9]. On the other hand, Biler et al. [13], Engin et al. [14], Hufstedler et al. [3], they all investigated vortical gusts in water tunnels. The present work instead introduces a new experimental set-up designed to generate isolated vortex gusts in a wind tunnel.

1.6 Gust generation: current state-of-the-art

In this section, we first examine the state-of-the-art of the experimental facilities currently available for generating vortex gusts, with a primary focus on tow tanks. While these are currently the predominant facilities for such studies, the present work aims to bridge this gap by providing experimental results obtained in a wind tunnel, as detailed in the following sections.

Subsequently, a detailed review of different gust generation techniques and methodologies is presented to establish a clear technical framework.

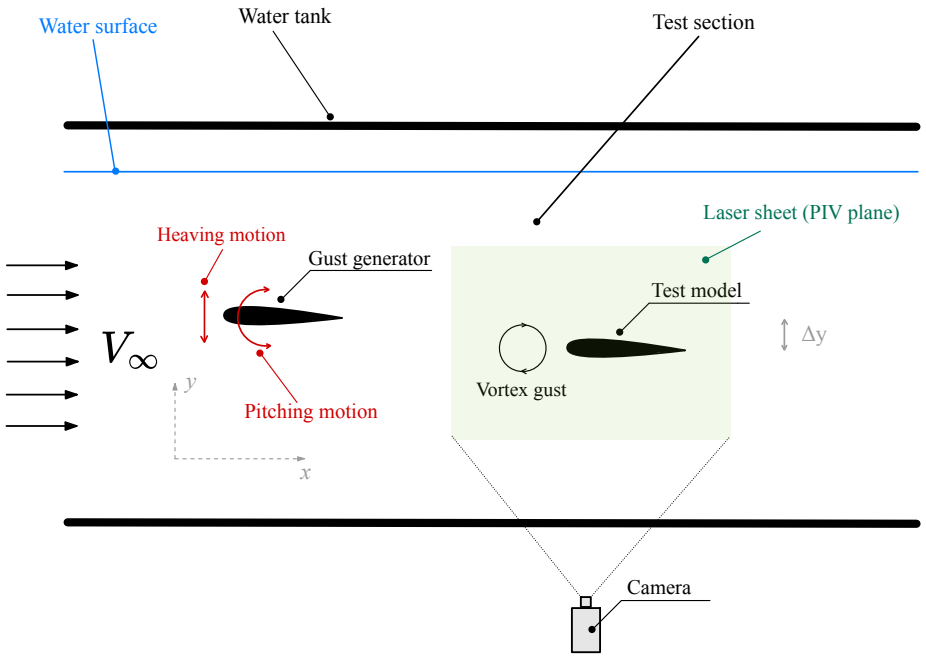


Figure 1.8: Two-dimensional frame of the experimental set-up.

1.6.1 Test Facilities

The current experimental state-of-the-art for vortex gust studies mainly relies on tow tanks and free-surface water channels (fig. 1.8). These facilities are chosen to provide a controlled environment for studying the interaction between generated vortices and downstream models. Most of these experiments are conducted at relatively low Reynolds numbers, typically ranging from $Re = 10^4$ [13, 14] to $Re = 2 \cdot 10^4$ [3, 22] up to $Re = 2,4 \cdot 10^4$ [23].

To achieve these conditions, the physical setup and the experimental hardware are generally organized as follows:

- gust generators are located upstream and consist of flat plates or airfoils mounted on high-precision actuation systems to create specific vortical disturbances;

- test model is positioned downstream to encounter the gust, usually held static or at specific angles of attack to measure the impact of the incoming vortex. To ensure the flow remains as two-dimensional as possible and to minimize tip-vortex interference, end-plates are frequently attached to both the generators and the test models.;

- Particle Image Velocimetry (PIV) is the standard tool for flow diagnostics, involving high-speed cameras synchronized with pulsed or continuous lasers to visualize the vortex evolution;

- aerodynamic loads are recorded using multi-axis force/torque sensors attached to the model's support beam.

1.6.2 Techniques for Gust Generation

In the following section a review of techniques for vortex gust generation will be presented. These methods focus on different ways to actuate the gust generator to achieve specific vortex characteristics and flow behaviors.

In the first example of gust generation carried out by Biler et al. [13] (fig. 1.9), a rotational technique is employed where the vortex is created by a one-half clockwise rotation of a flat-plate generator about its midchord. As the plate rotates it sheds a primary negative vortex from its leading edge, which is identified as the actual vortex gust. Although a positive vortex is initially shed from the trailing edge, it is considered too weak and distant from the test model to be part of the characterized gust. The methodology and experimental configuration adopted in this study are primarily inspired by the work of Biler et al. [13]; specifically, their approach to generating and characterizing vortex gusts serves as the baseline for our experimental framework.

In the approach described by Hufstedler et al. [3] outlined in fig. 1.10, the vortex gust is generated through the heaving motion of a pair of upstream flat plates. These plates are actuated to plunge vertically in a synchronized manner across the flow. By precisely controlling the transverse velocity of the heaving plates, specific vortical structures are shed and allowed to convect downstream toward the test model. This configuration is specifically designed to produce a transverse gust, creating a controlled velocity profile that allows for the study of unsteady aerodynamic responses as the generated vortex interacts with the stationary wing.

A third example of gust generation carried out by Wang et al. [23] (fig. 1.11) involves the use of pitching blades to create periodic perturbations. In this configuration, a pair of rigid blades are installed upstream of the test model. Driven by a servo motor, these blades are actuated to pitch about their central chord points following sinusoidal profiles. By using blades with a larger chord and thicker profile than the downstream model, it can generate more substantial gusts while maintaining a specific spacing between the blades to limit wake interference in the measurement area. This setup is designed to produce periodic vertical and longitudinal gusts.

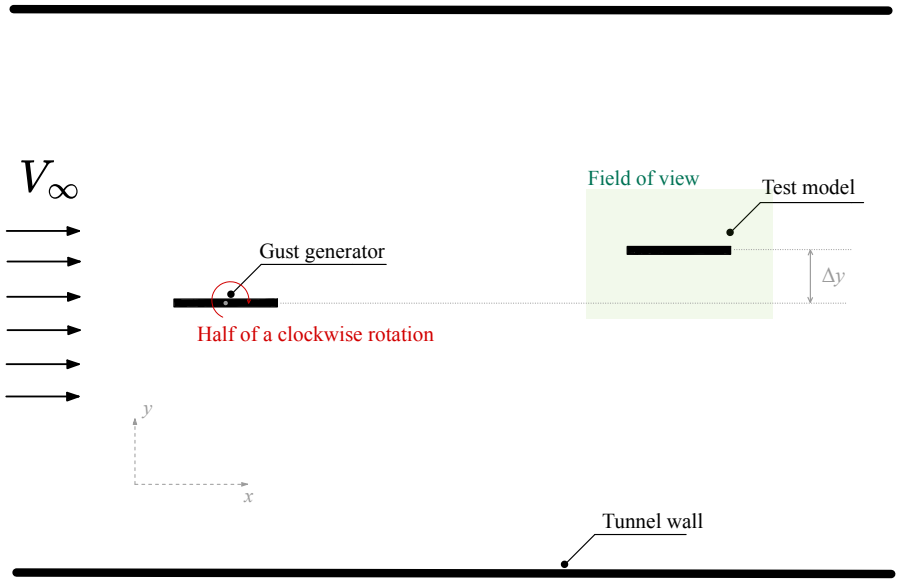


Figure 1.9: Sketch for vortex gusts generation carried out by [13, modified].

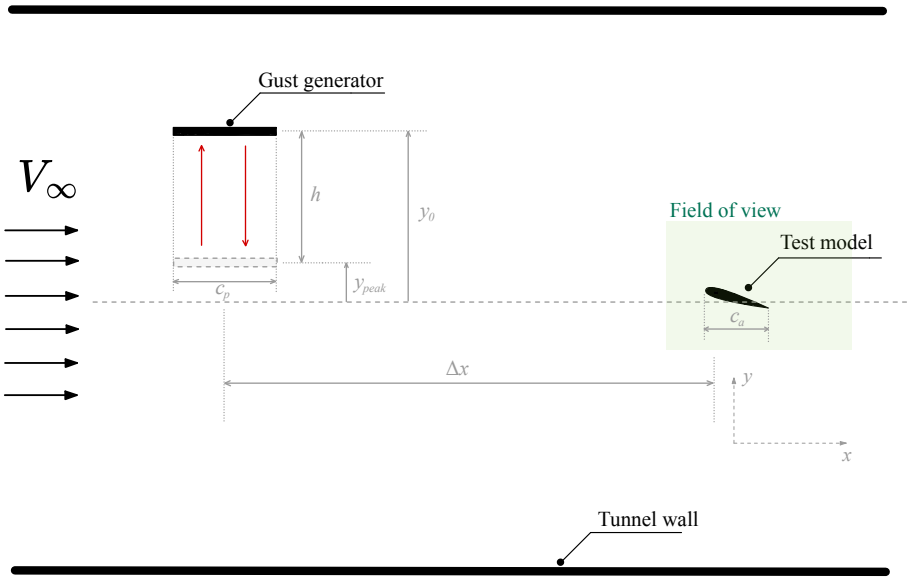


Figure 1.10: Sketch for transverse gusts generation carried out by [3, modified].

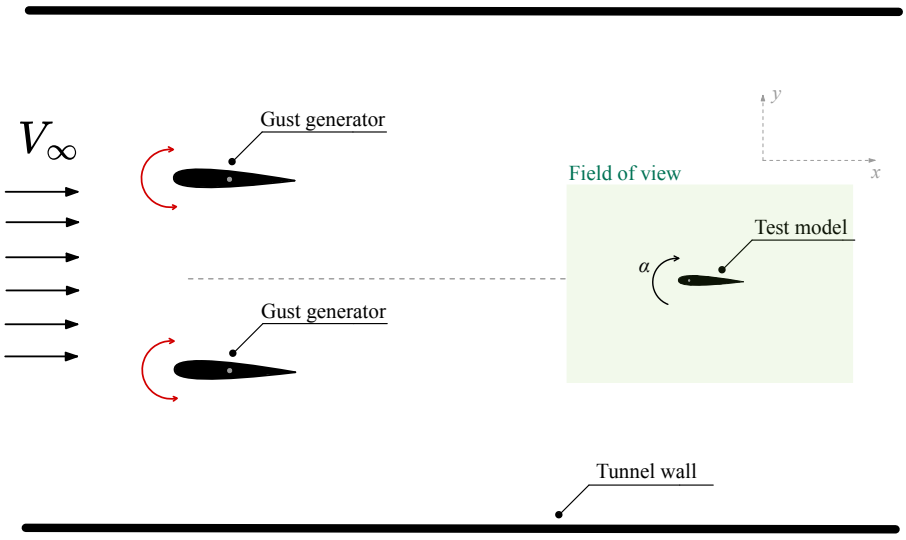


Figure 1.11: Sketch for vertical and longitudinal gusts generation carried out by [23, modified].

1.7 Identification of the research gap

From a numerical perspective, modeling a vortex gust is relatively simpler than the experimental methods, as the disturbance can be mathematically defined and directly superimposed onto the inflow velocity field without the need for complex mechanical actuation. The current state-of-the-art of the vortex gust generation relies on water tow tanks, low Reynolds number and slow actuation systems.

Numerical simulations are essential in this field, especially considering the significant technical challenges involved in generating a controlled vortex gust within a wind tunnel especially at high numbers of Reynolds. While experimental setups are often limited by mechanical issues, computational models provide a reliable way to investigate the complex physics of vortex-airfoil interactions under a wide range of conditions.

In recent years, the study of these interactions has increasingly shifted towards data-driven perspectives to overcome the limitations of traditional computational fluid dynamics. Given the high dimensionality and non-linear nature of extreme vortex-gust encounters, these methods aim to simplify the complex evolution of vortical structures into more manageable, low-order representations using machine learning techniques [24].

The present work instead introduces a new experimental set-up designed to generate isolated vortex gusts in a wind tunnel. A 180° clockwise rotation of a flat plate induces vortex shedding from both the leading and trailing edges. The present study focuses exclusively on the characterization of the vortex shed from the trailing edge and its interaction with an aerodynamic surface. The experiments were per-

formed at different freestream velocity, with Reynolds numbers ranging from 2×10^4 up to 3.6×10^4. Furthermore, the second step consists of observe how this kind of gust interacs with a sensins flat plate with zero pressure gradient and to model its behaviour.

Chapter 2

Event-Based Imaging Velocimetry

The study of highly unsteady aerodynamic phenomena, such as vortex gust characterization, demands diagnostic tools with extremely high temporal resolution. This chapter explain the key concepts of Event-Based Imaging Velocimetry technique.

2.1 Introduction

In the last couple of years, the neuromorphic event-based vision has been gaining regard in the research field [25, 26]. Compared to traditional frame-based imaging, event-based sensors introduce a new way for data acquisition, offering more elevated temporal performance compared to the traditional frame-based cameras. Commonly referred to as event cameras, these devices operate by detecting brightness variations asynchronously and independently at the individual pixel level across the entire sensor array. Every brightness change is referred as an event, which consists of four types of information, indicated as AER (address event representation) [27, 28]

$$e = f(t, x, y, p)$$

where

- t represents the event's microsecond-resolution timestamp of when the event itself was detected and recorded;
- (x, y) are the pixel's coordinates in which the event has occurred (see sec. **??** for sensor resolution employed for this present work);
- p is the polarity, which indicates the kind od brightness change. Typically when a positive event occurs $p = +1$ (i.e., increasing of brightness); when a negative event occurs $p = -1$ (i.e., decreasing of brightness).

Generally speaking, for a two dimensional-two components (2D-2C) analysis, the measurement process using the Event-Based Image Velocimetry (EBIV) technique is carried out as follows. The fluid is seeded with tracer particles that accurately follow the flow dynamics. To follow the fluid motion, tracer particles must satisfy two main conditions: their density should be as close as possible to the fluid density, minimizing or eliminating gravitational settling velocity; they must respond quickly

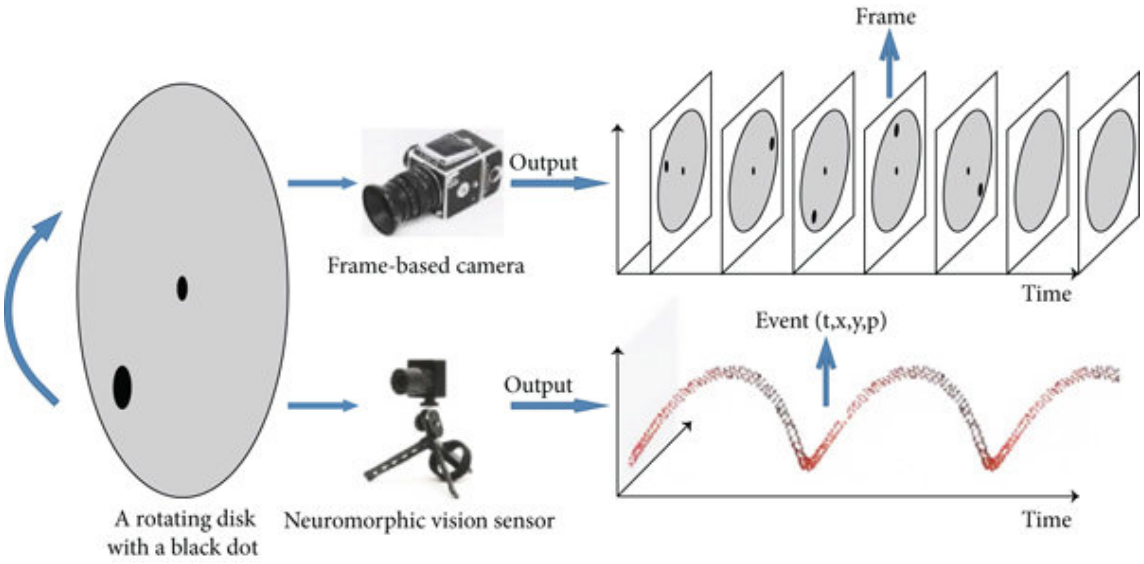


Figure 2.1: Comparison on operating principles between frame-based and event-based cameras [29].

to flow velocity variations [30]. The response time of the tracer particles is described by the relaxation time

$$t_p = \frac{\rho_p d_p^2}{\mu_f} \tag{2.1}$$

which measures how quickly a particle responds to changes in fluid velocity. By comparing t_p with a characteristic time scale of the flow t_0 (such as the convection time), it is possible to define the Stokes number:

$$\mathrm{St} = \frac{t_p}{t_0} \tag{2.2}$$

The condition $\mathrm{St} \ll 1$ ensures that tracer particles follow the fluid without perturbing their dynamics.

A laser source, either pulsed or continuous, is used to generate a thin light sheet that illuminates the target measurement plane.

As the tracer particles cross the illuminated plane, the event-based sensor detects localized changes in light intensity. Each pixel independently and asynchronously triggers a time-stamped event.

After that, the recorded asynchronous event stream is analyzed using optical flow algorithms to compute particle displacements. Validation criteria are applied to the computed vectors to reconstruct the instantaneous velocity fields for subsequent analysis.

2.1.1 Operating principles between FB and EB sensors

In order to better understand the differences on operating principles between Frame-Based (FB) and Event-Based (EB) sensors, we refer to fig. 2.1.

Once a standard camera (i.e., frame-based camera) faces a rotating disk with a black dot on the peripheral side, the output results in a series of different frames

at fixed rate, which is defined by the frame-per-seconds (fps) of the sensor. The sensor sends a redundant information when detects no motion in its field of view. On the other hand, during a transitory phase, for example a rapid acceleration of the rotating disk, standard cameras can suffer the motion blur as well, by missing the information between two consecutive frames [28]. These drawbacks can limitate the range of applications of standard cameras [29].

Since the use of standard cameras can lead to an important loss of information and a huge storage of stream data, the event-based cameras find a wide range of employing in research field. Event-based sensors respond asynchronously to pixel level of brightness with a tiny latency (on the order of microseconds). When no motion is recorded, the sensor capture no variation of brightness. This process can be described by a series of state changes (ON, OFF). In the specific case of rotating disk, the neuromorphic sensor detects an increasing level of brightness (i.e., $p = +1$, state ON) by following the black dot. The other part of the disk faces no state change, hence a decreasing of brightness is detected (i.e., $p = -1$, state OFF) [28, 29]. As we can observe in fig. 2.1, the resulting output will be a continuous flux of events in the data stream.

2.1.2 Rewards of Event Cameras

Event cameras offers numerous rewards over standard frame cameras [25]. Among these, we can find a high temporal resolution [25]. Since the sensor operates at 1 MHz of frequency, events are detected and timestamped with a microsecond resolution (i.e., $\Delta t = 1$ μs). Hence, event cameras are extremely fast and can resolve high-frequency dynamics without suffering blurring or information loss.

Since every pixel works asynchronously from each other, it transmits immediately the state of change whenever it is detected. On the other hand, conventional frame-based cameras needs the global exposure of the frame. For this reason, event cameras have a very low latency (on the order of sub-millisecond) [25].

As written above, event cameras detect only brightness change. Power is employed only to process the variation. For most cameras we have $\sim$ 10 mW, which means low power [25].

Event cameras present a very high dynamic range due to the working principles of indipendent pixels. Since the photoreceptors operate in logarithmic scale and they do not require for a shutter, they offer high-quality level [25].

2.1.3 Drawbacks of Event Cameras

As we explained above, event cameras offer several rewards useful for visualizing flows. However, they present different challenges which will be explained in the following.

Firstly, the output is a continuous asynchronous stream of events, which means that the end user may develop a specific algorithm for decoding the flux of events in order to preserve the physical space-time structure. In the most of cases, the stream of events is packed in tuples, which are a finite sequence of numbers [25].

In opposite to the conventional ones, the event-based cameras provide the information about the event state change (increasing or decreasing of brightness):

however, the illumination variations depend also on the current and past relative motion between the camera and the scene [25].

All vision sensors suffer from shot noise and thermal fluctuations due to the asynchronous nature of their pixel-level circuitry. The complex process of quantizing temporal generates Background Activity (BA), which are spurious events triggered by electronic noise rather than physical motion that can obscure small particles tracers. Lastly, analog comparator variations across the array cause threshold jitter, resulting in non-uniform pixel latencies that affect the overall precision of the event stream [25].

2.2 Event generation basis and signal processing

Each Event-Based Vision (EBV) pixel operates as an independent, autonomous unit comprising a photodiode, a dedicated contrast detection circuit, and a logical unit (fig. 2.2). When photons strike the photodiode, the induced photocurrent is converted into a voltage. By utilizing a logarithmic scale, the pixel can trigger contrast detection [31]. The contrast change, denoted as $C(t)$, evaluates the temporal derivative of the logarithmic light intensity $I(t)$ [32, 33]:

$$C(t) = \frac{\mathrm{d}}{\mathrm{d}t} \ln[I(t)] \tag{2.3}$$

A new event is then triggered only when this variation exceeds a threshold:

$$|C(t)| > C_{\text{thr}}$$

This threshold is typically set between 10% and 25% [31, 34]. It can be adjusted independently for positive (ON) and negative (OFF) intensity changes, which often results in an asymmetric sensor response. In low-light conditions, the logarithmic differentiation becomes less reliable as dark-current fluctuations may generate spurious background activity; this issue can be mitigated by fine-tuning the pixel sensitivity biases [34].

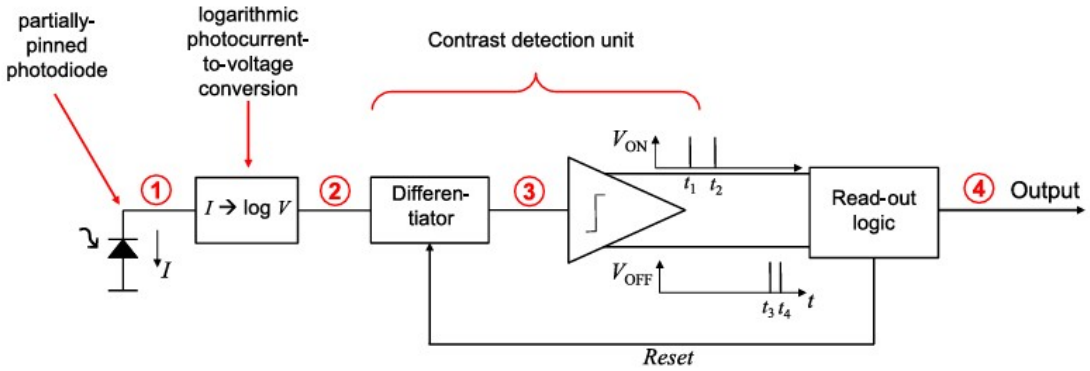


Figure 2.2: Simplified schematic of an Event-Based Vision pixel and associated signals processing at each step [31].

As soon as a threshold crossing is detected, the logical unit initiates an asynchronous readout procedure [31]. Once fully acknowledged, a digital data packet containing the microsecond-accurate timestamp t_i, the polarity p_i, and the spatial coordinates (x_i, y_i) is forwarded to the output data stream. Following transmission, the logical unit resets the pixel reference voltage to the current intensity level ($I_{\text{ref}} = I(t_i)$), concluding the dead time and enabling the system to capture subsequent transients. Fig. 2.3 illustrates this pixel-level event generation mechanism for a tracer particle crossing the photodiode area.

The overall array sensitivity is governed by user-tunable biases that control the detection thresholds. Optimizing these parameters for experimental fluid dynamics represents a major challenge, as environmental variables—such as non-uniform illumination and high particle image density—strongly couple with the dynamic response and latency of the sensor [31].

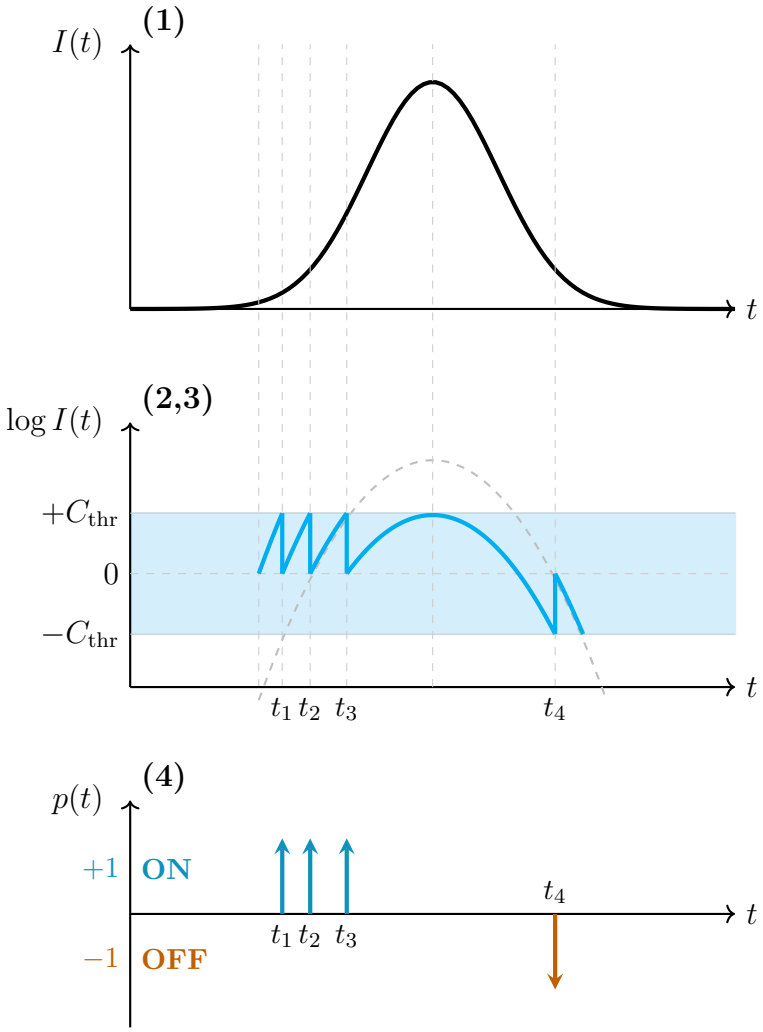


Figure 2.3: Sketch of the event generation process for a single pixel of the sensor: **(1)** time-varying intensity Gaussian signal seen by the photodiode, **(2,3)** log intensity signal, **(4)** asynchronous event stream produced by the pixel.

2.2.1 Latency in EBV Sensors

Latency in event-based sensors is the delay between a contrast change at the photodiode and the timestamp assigned to the event. It consists of two main contributions: pixel latency, caused by pixel-to-pixel hardware variations, and system latency, which arises when the event rate exceeds the sensor read-out bandwidth, leading to timestamp inaccuracies [31].

Pulsed illumination can be used to characterize latency through the event arrival histogram. Distinct peaks indicate that events are correctly associated with each laser pulse, whereas peak broadening or overlap reveals excessive latency. To prevent arbiter saturation, the light intensity, particle image density (ppp), and active Region of Interest (ROI) can be adjusted [31]. A smaller ROI reduces the arbitration load, while appropriate sensor bias settings, such as suppressing negative-polarity events, can further increase the usable particle density. The pulse frequency f_p should be chosen so that the event burst generated by one pulse decays before the next pulse arrives.

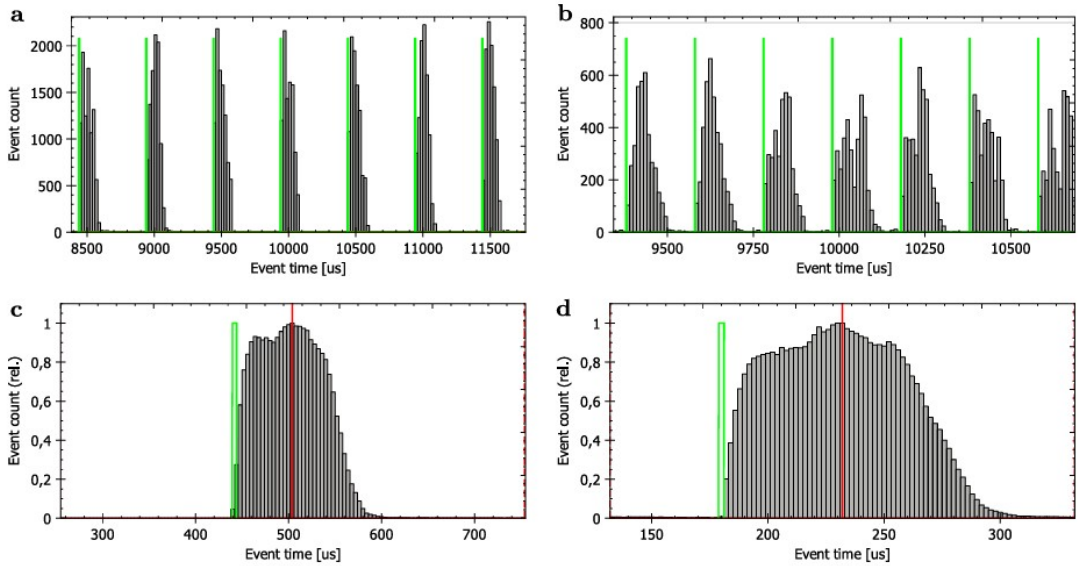


Figure 2.4: Histograms of recorded event times for pulsed-EBIV measurements. The green lines indicate the actual time and width of the laser trigger pulses. The top row (a, b) shows a random sample within the record , whereas the lower row (c, d) provides the averaged temporal distribution of events. The vertical red line marks the peak of the event distribution [31].

2.3 Processing of event-data

Pseudo-images are generated by accumulating events around each maximum of the event histogram (Fig. 2.4), exploiting the known pulsing frequency. When laser trigger pulses are recorded in the event stream, the temporal association of events is straightforward; otherwise, pulse timing is estimated from the fixed repetition rate. The conversion of the raw event stream into pseudo-images follows three steps.

The first one consists of estimate the temporal position of each light pulse from the known pulsing frequency (required only if trigger pulses are not recorded) [31].

After that, it is necessary to accumulate all events belonging to a given pulse into a single pseudo-image, assigning equal intensity to all active pixels regardless of their individual timestamps [31].

Finally, it is possible to apply a Gaussian low-pass filter to convert single-pixel events (Dirac-delta-like) into approximately Gaussian particle images, as required by standard PIV cross-correlation algorithms [31].

Chapter 3

Experimental set-up

This chapter provides a comprehensive description of the experimental set-up developed of the present work.

3.1 Wind tunnel and vortex gust generator

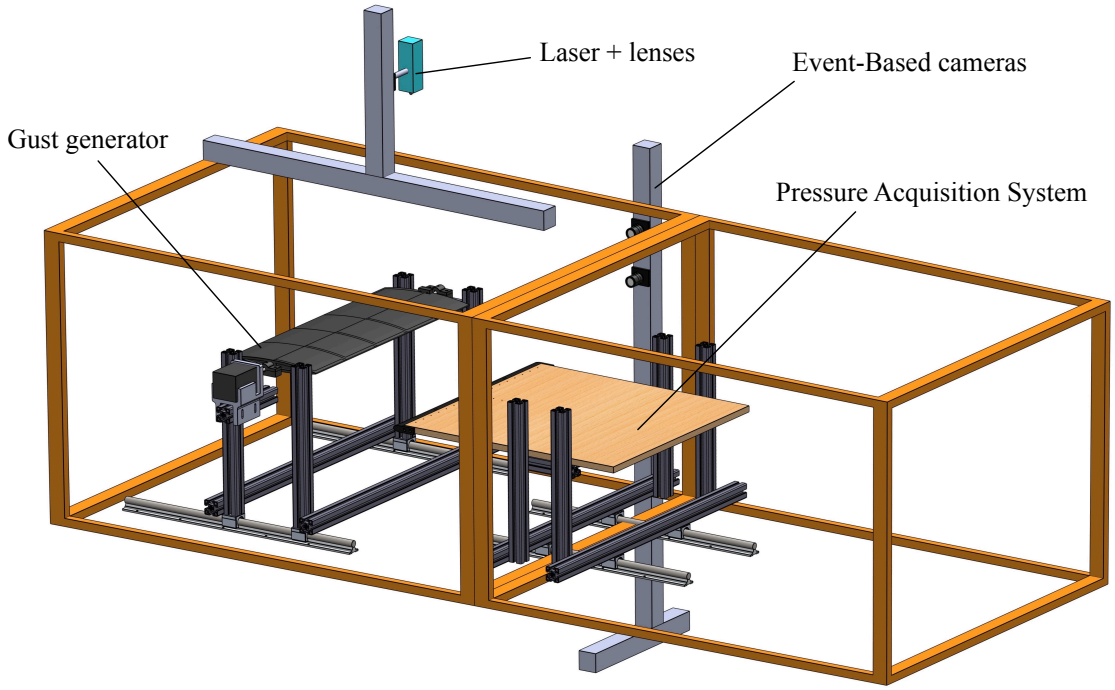


Figure 3.1: Isometric view of the wind tunnel facility and experimental vortex-gust generator setup.

The experiments are carried out in the open-circuit wind tunnel at Politecnico di Torino. The flow is accelerated by two fans located upstream of a stagnation chamber, and it is then conveyed to the test section through a convergent. The test section has a rectangular cross section 0.9 x 1.2 m (height $\times$ width) and a length of 6.5 m; it is characterized by a small divergence angle of 1% to account for the growth of the boundary layer on the wind tunnel walls [35]. A Pitot tube, installed

at the outlet of the convergent, is used to measure the experimental flow speed. In particular, a dedicated system was installed to automatically control the needed flow speed U_∞.

The vortex gust generator used for these experiments basically is a Polylactic Acid (PLA) flat plate with an aspect ratio of $AR \simeq 2.67$ (30 cm chord, 80 cm span). The vortex gust was induced by a 180° clockwise rotation of a flat plate generator centered at its midchord (fig. 3.1). At the start of the motion, due to the negative direction of rotation imposed on the gust generator, an intense vortex characterized by counter-clockwise rotation and positive circulation values is shed from the trailing edge of the flat plate. The present study focuses exclusively on the characterization of this coherent structure, which is formally identified as the primary vortex gust. Conversely, the second vortex released from the leading edge is found to be weak, unstructured, and negligible for the analysis of the gust [13]. It is important highlight that the reference system for the campaign was located at the trailing edge (see fig. 3.5).

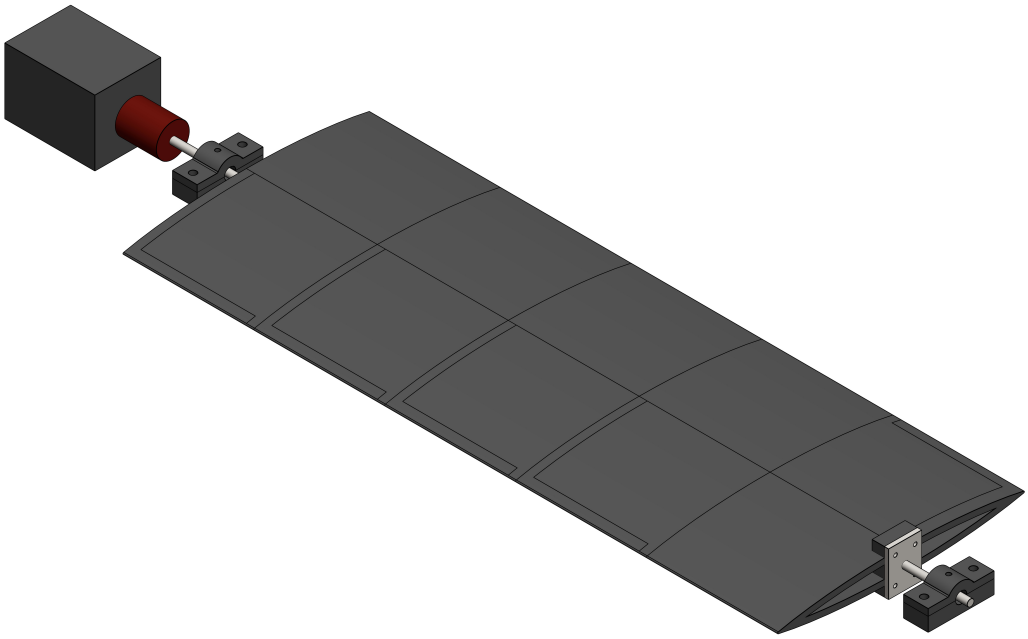


Figure 3.2: Isometric view of vortex-gust generator.

3.2 Control and acquisition systems

The control system (which architecture is outlined in fig. 3.4, upper) is designed to manage the motion of the flat plate, ensuring synchronization between mechanical movement and data acquisition. The system is powered by a 220V AC mains line connected to the servo drive. This unit acts as the primary power converter and controller, regulating the energy flow to the motor based on the control signals. A

secondary 5V DC source provides stabilized power to the logic components of the control unit, in order to avoid background noise and shield the system from electromagnetic interferences. The control unit integrates an Arduino UNO R4 WiFi microcontroller and TTL (transistor-transistor logic) sensors. The unit interfaces with Workstation 2 (PC) via a serial connection, receiving commands. The Arduino translates these commands into specific instructions for the Servo Drive. The rotation is generated by a servo motor mechanically coupled to the flat plate. To achieve precise positioning and velocity control, the system employs a feedback loop. An integrated encoder on the motor monitors the rotation in real-time, sending differential signals back to the TTL sensors through the servo drive. These quadrature signals are processed by the DAQ (Data Acquisition) system as A and B phases. This allows the acquisition system to correlate each event-based data packet with the exact angular position of the motor (i.e. the vortex gust generator position).

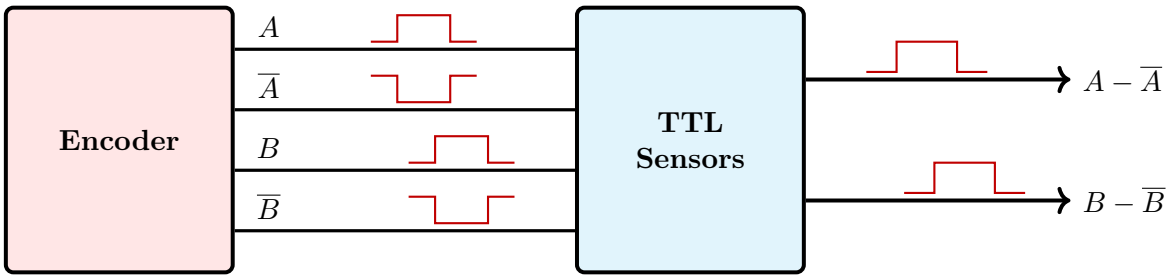


Figure 3.3: Feedback loop line: the encoder digital signals flows to the DAQ through TTL sensors, which transform the differential quadrature signals into a single-ended quadrature signals.

The actuation system is based on a 1 kW AC servo drive (200–240 V), coupled with a 17-bit absolute encoder. This configuration ensures high-resolution position feedback and a 2 kHz speed loop bandwidth, enabling accurate positioning and a fast dynamic response even when driving the shaft under load. The encoder generates two differential digital signals in quadrature, maintaining a constant $\pi/2$ electrical phase shift. These signals were acquired by the DAQ with a sampling frequency of $f_s = 100\,\text{kHz}$. By evaluating their phase relationship, the system determines the exact angular displacement and direction of rotation, as one signal leads or lags the other depending on the rotation (see the algorithm in fig. 4.5).

The flow velocity Acquisition System is made up of two main components. A Pitot tube was used for measuring the dynamic pressure. Within the measurement chain, it is positioned at the outlet of the convergent. A capacitive pressure transducer (SETRA mod. 239 C) was employed. The instrument has a measurement range of ± 0.2 psi (± 13.79 kPa), corresponding to a full-scale value of 0.4 psi (27.58 kPa). The output signal is analog, with a voltage range of ± 2.5 V with an accuracy of 0.14% of full scale. The actual wind tunnel flow velocity was obtained by associating the output voltage level of the differential pressure transducer with the pressure difference. Basically, we have a linear law

$$\Delta p = k_T \Delta E \tag{3.1}$$

where

$$\Delta E = E_{out} - E_0 \tag{3.2}$$

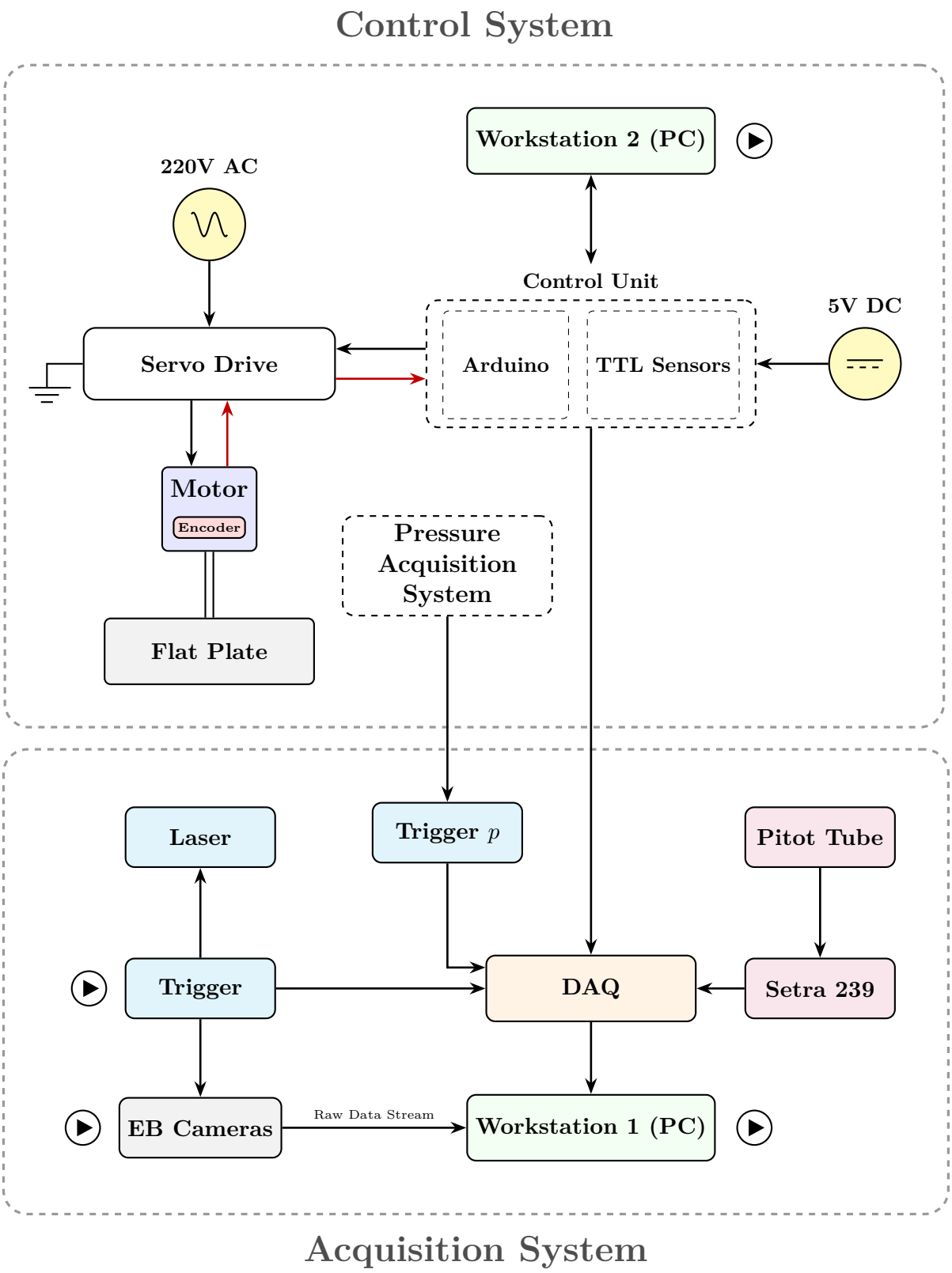


Figure 3.4: Architectural scheme of the Control System and the Acquisition System for the experimental set-up.

with E_0 indicating the offset voltage value measured when a zero pressure difference is applied to the transducer; the linear coefficient k_T is given by the manufacturer. Once the Δp is known, the flow velocity can be obtained from Bernoulli's equation $U_\infty = \sqrt{2\Delta p/\rho}$. For the sake of completeness, the value obtained by the Pitot's measure it has been compared with the one obtained through PIV (i.e., event-based cameras) measurements because they might slightly deviate each other.

3.3 Flowfield measurements

The EBIV (Event-Based Imaging Velocimetry) set-up is a subsystem integrated within the Acquisition System, as sketched in fig. 3.4 (lower). Its primary function is to capture high-resolution data of the physical phenomena occurring downstream to the half-rotating vortex gust generator. The set-up, which is sketched in fig. 3.5, includes four interconnected hardware components.

Flow seeding was provided by a LaVision HFSB (Helium-Filled Soap Bubbles) generator. These flow tracers are characterized by a diameter of ≈ 300 μm and adjusted to be neutrally buoyant in air. The bubbles are introduced upstream of the test section to achieve a homogeneous seeding distribution. Their relaxion time $t_p = 11\,\mu$s ensures that they follow the flow dynamics in accordance with the Stokes' hypothesis $\mathrm{St} \ll 1$ [36].

Flow visualization is achieved using a Lasertree LT-4LDS-V2 laser module, which delivers an optical power output of approximately 20 W at a wavelength of 455 ± 10 nm. For this specific experimental campaign, the pulsing frequency was set to 500 Hz with a 25% duty cycle. The laser beam is shaped into a ≈ 1 mm thick light sheet by using a custom optical train; a combination of two Thorlabs piano-concave cylindrical lenses ($f_1 \approx -20$ mm, $f_2 \approx -9$ mm) and a telescopic spherical system is employed. The resulting planar illumination is sketched in fig. 3.5 (bottom).

Image acquisition was performed simoultaneously by using two event cameras arranged in a vertical stack configuration. Thus, the cameras allowed to extend the overall field of view downstream to the vortex gust generator, with a little overlapped region (see the sketch 3.5, upper). We employed two Prophesee EVK-4 (30x30x36 mm) event-based camera equipped with a Sony IMX636 sensor (resolution: $1280\times720\,\mathrm{px}^2$). Both cameras were fitted with Nikon AF Nikkor 28 mm $f/2.8$D lenses. Using two cameras may lead to a spatial misalignment, which needs to be quantified. For this purpose, a dedicated stiching procedure was carried out using a rotating pinwheel target with high-contrast black-and-white pattern. Both cameras acquired simultaneous pseudo-images of the rotating target, following the same event accumulation procedure described above in sec. 2.3. The spatial offset between the two cameras was estimated by computing the normalized 2D cross-correlation between the pseudo-images. A Gaussian smoothing filter (kernel $5 \times 5\,\mathrm{px}^2$) was applied to both pseudo-images in order to reduce noise and improve the sharpness of the correlation peak, resulting in a spatial shift of $(\Delta x, \Delta y) = (-592, -6)$ px. The large horizontal offset reflects the partial overlap (fig. 3.6) between the two fields of view. The residual vertical misalignment of 6 px is attributed to a slight mechanical misalignment between the cameras, which is negligible. Figures 3.6 and 3.7 show the stitching results and a raw merged pseudo-snapshot of the flow field, respectively.

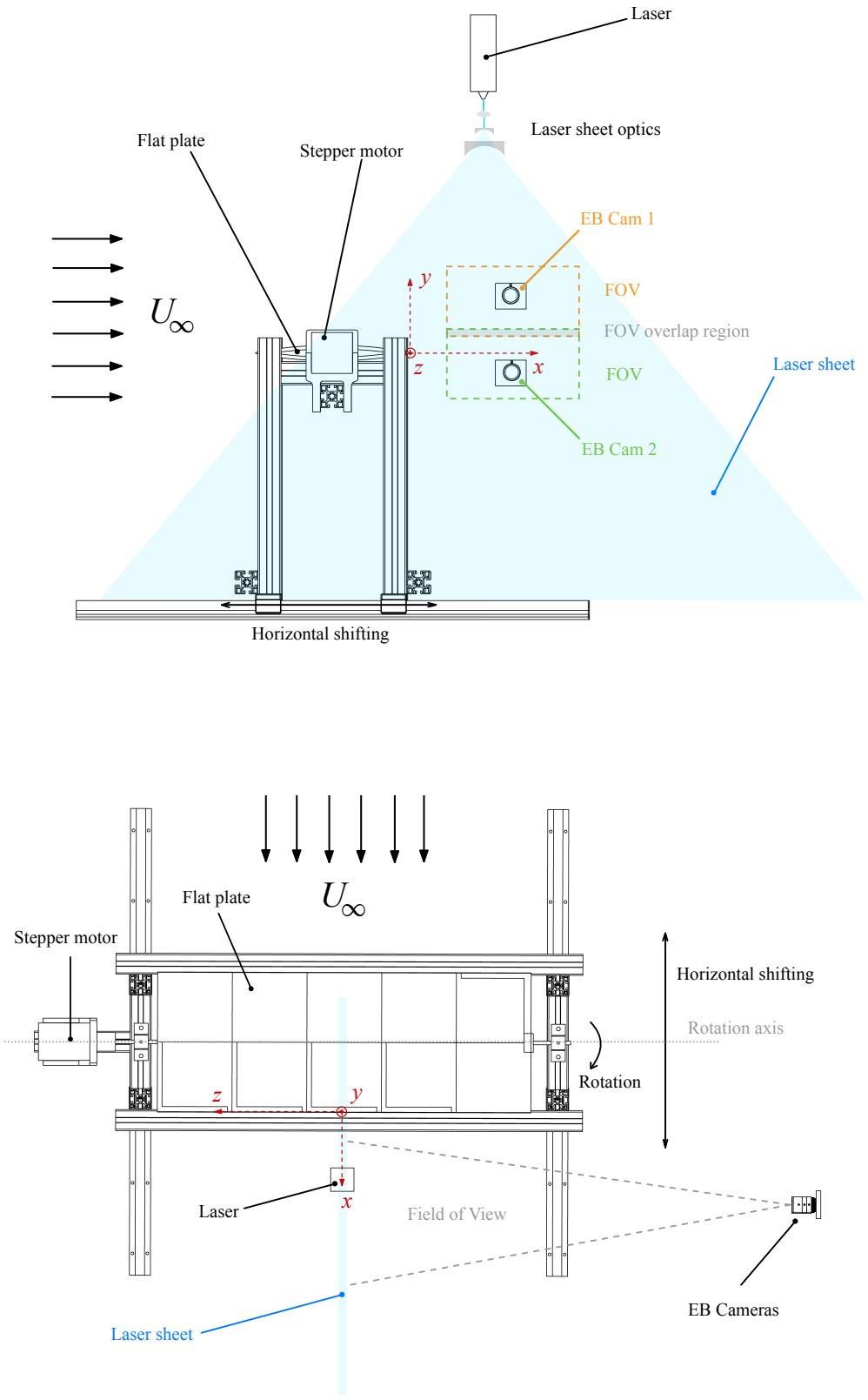


Figure 3.5: Side (top) and upper (bottom) views of the vortex gust generator and EBIV set-up for the characterization of the isolated vortex gust.

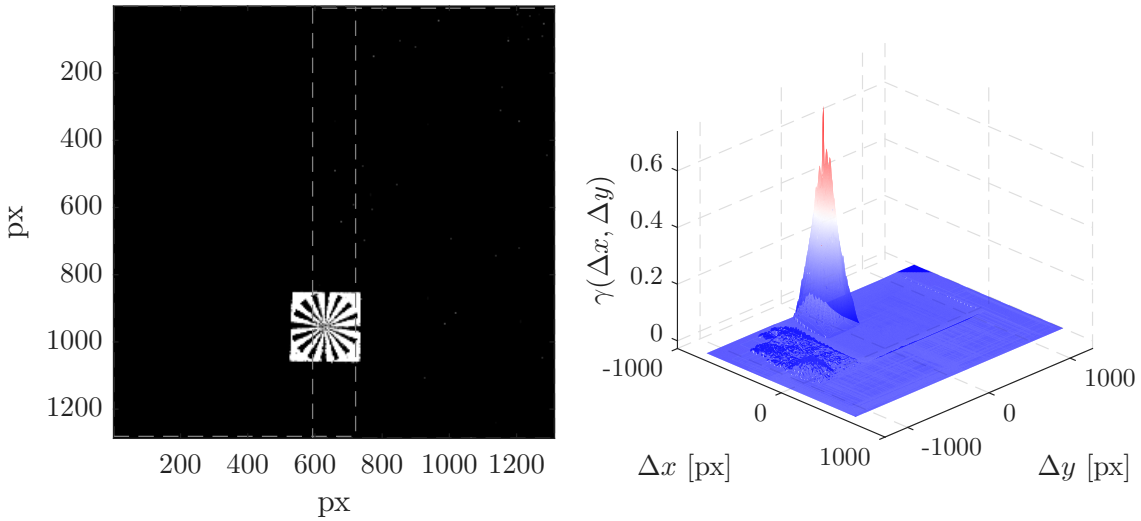


Figure 3.6: Overall field of view of both cameras; the region within dashed lines represents the overlapped region (left). Cross-correlation map $\gamma(\Delta x, \Delta y)$ between cameras (right).

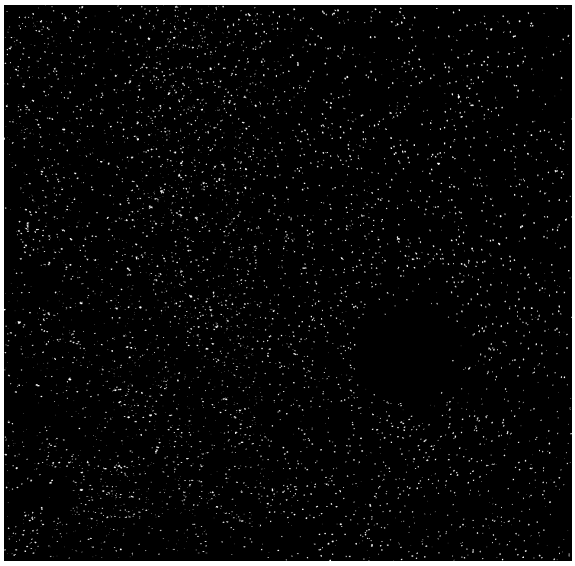


Figure 3.7: Merged raw pseudo-snapshot of the flow field captured by the (two) event cameras vertical stacked at a laser pulsing frequency of 500 Hz and $U_\infty \approx 1\,\mathrm{ms}^{-1}$. White spots illustrates the distribution of HFSB acting as flow tracers.

3.3.1 Triggering

Triggers allows the perfect synchronization for timing between the continous flux of events, thus the acquisition of event-based cameras, and illumination source pulsing. A Digilent Analog Discovery hardware unit was performed for trigger generation, which is distributed to the illumination source, both Event-based cameras and it is simultaneously read by DAQ (as sketched in fig. 3.4). The logic of synchronization and timing diagram of the acquisition system for signals is sketched below in the fig. 3.8 and follows a similar scheme proposed by [37]. The raw data stream is managed via the Metavision SDK software, which is employed for bias configuration, Region of Interest definition, and event acquisition. The events are accumulated into temporal windows (ΔT_{trig}) aligned with the trigger edges; this approach minimizes the jitter between illumination and acquisition.

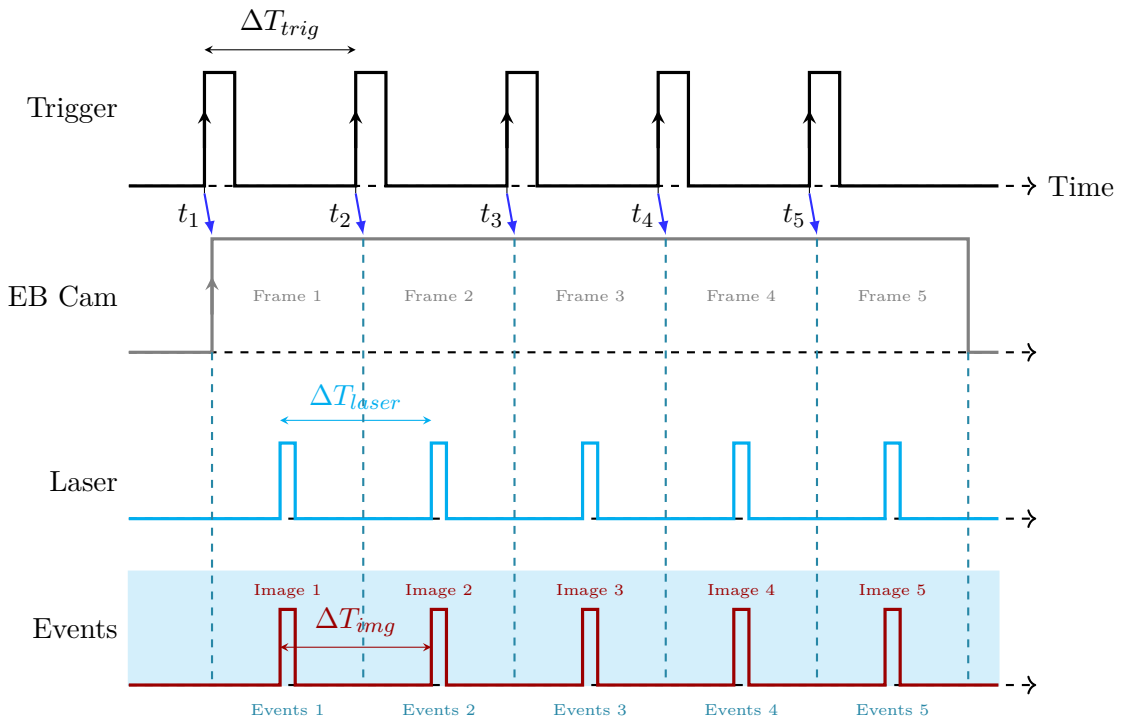


Figure 3.8: Timing diagram of the acquisition system for synchronization among trigger, laser and event-based cameras.

3.3.2 Image processing for vortex characterization

Velocity fields for EBIV datasets were computed using the PaIRS-UniNa (Particle Image Reconstruction Software) software. Raw merged images were processed using a multi-pass cross-correlation (CC) algorithm with interrogation window sizes of 128×128, 64×64, 48×48 pixels and 50%, 75%, 75% overlap respectively. A vector validation was employed among passes. The spatial resolution was found to be 3.44 px/mm. Each test case (see the tab. 5.1) was characterized by the sampling of 20 isolated vortices, for each of which 500 pseudo-snapshots were acquired. The resulting raw data were subsequently phase-averaged.

3.4 Pressure acquisition system

Once the characterization of the vortex gust has been made, a pressure acquisition system has been developed to study the interaction of the vortex gust with aerodynamic surfaces.

A nearly square sensing flat plate made of wood has been employed, measuring 72 cm in width, 74 cm in length and 2 cm in thickness. A 3 cm long super-ellipse shaped leading edge was chosen to avoid flow separation whenever the vortex gust interacts with the sensing plate. Regarding its positioning within the experimental setup, the leading edge of the sensing plate is located at $x/c = 0.7$ (corresponding to 21 cm) and $y/c = -0.45$ (corresponding to -13.5 cm) with respect to the origin of the reference system.

The sensing flat plate was equipped with 5 Honeywell pressure transducers, which were placed near the leading edge underneath the lower edge. These 5 sensors are equally spaced: the first transducer is positioned 4.5 cm from the beginning of the leading edge, while the subsequent sensors are spaced 1.5 cm apart from each other; in tab. 3.1 are reported the absolute positions relative to the origin of the reference system. The sensors feature a differential pressure range of $\pm$15 psi ($\pm$103.4 kPa), with an accuracy of $\pm$0.25% full-scale span. The transducers were connected through dual pressure ports to the pressure taps on the sensing plate. The hole diameter of the sensing plate is 0.5 mm (fig. 3.9, bottom). Furthermore, during the campaign test, the sampling rate was set at 1 kHz and the data were recorded for 230 s. The pressure acquisition system was located downstream the vortex gust generator (fig. 3.9, top). The sampled data were read through an Arduino board UNO Rev3, which is also responsible to generate a trigger signal read by DAQ. This second trigger is crucial to chose correctly the needed instant to read pressure sampling. Subsequently, in order to post-process the data, pressure measurements were synchronized with PIV measurements. Particullarly, following the same logic of synchronization in fig. 3.8, the trigger was synchronized with encoder signal and properly associated with the cameras trigger. In this way, it is possible to post-process the final results by having three different synchronized signals: the encoder's signal, the PIV's images and the pressure's sampling.

Table 3.1: Positions of the 5 pressure transducers on the sensing flat plate, expressed relative to the origin of the reference frame. c is the chord of the gust generator.

	Sensor 1	**Sensor 2**	**Sensor 3**	**Sensor 4**	**Sensor 5**
x [cm]	25.5	27.0	28.5	30.0	31.5
x/c	0.85	0.90	0.95	1.00	1.05

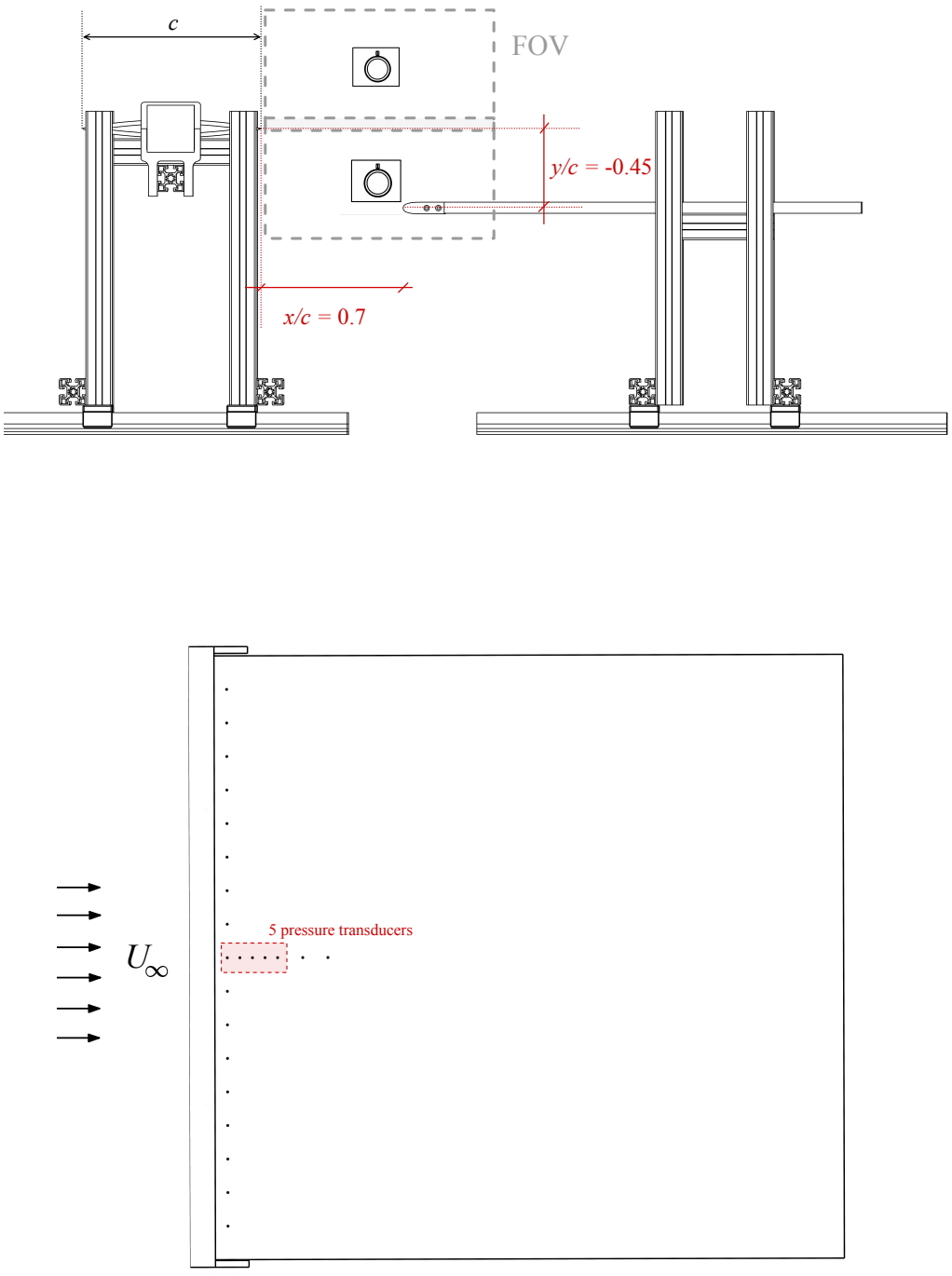


Figure 3.9: Side view (top) of the vortex gust generator and the pressure acquisition system. Upper side (bottom) of the flat plate equipped with 5 pressure sensors. It is worth noting that the high-frequency transducers are located in streamwise direction in the centreline.

3.4.1 Image Processing for vortex–aerodynamic surface interaction

For the pressure-side measurement campaign, a multi-pass CC algorithm with interrogation window sizes of 64×64, 32×32, 16×16 pixels and 75%, 50%, 50% overlap was employed respectively. Each test case comprised 20 isolated vortices, for each of which 450 pseudo-snapshots were acquired. Prior to phase-averaging, images were stitched in groups of 5 vortex realizations in order to increase the effective seeding density (fig. 3.10), thereby enabling the use of smaller interrogation windows (i.e., at the cost of an increased noise level) and achieving a higher spatial resolution of the resulting velocity fields.

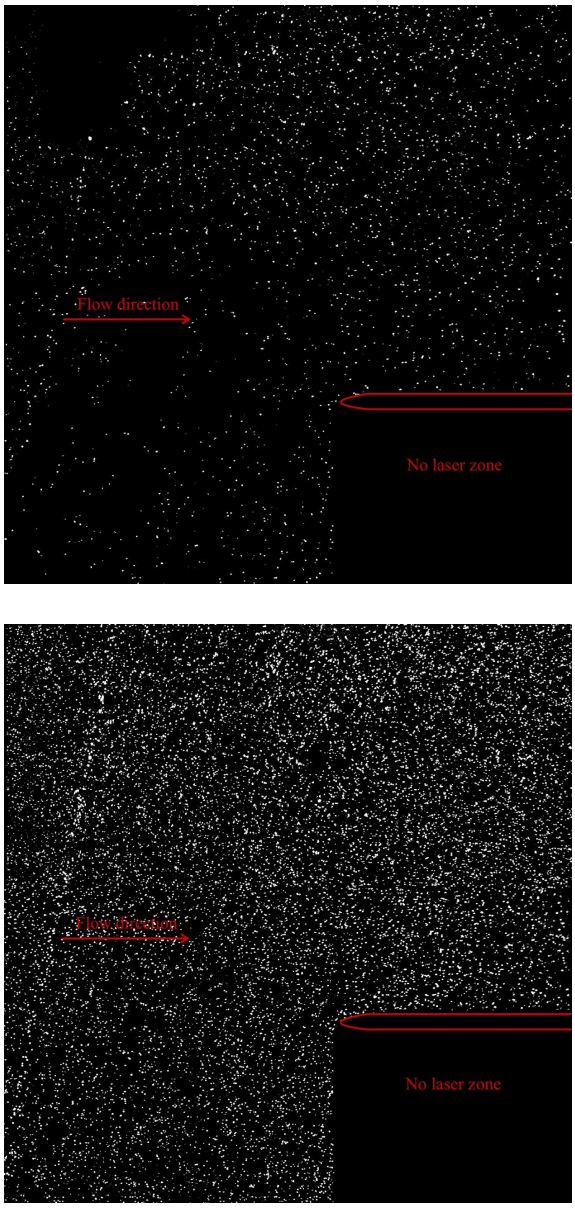


Figure 3.10: Representative raw seeding images before (top) and after (bottom) the stitching procedure.

To sum up, in tab. 3.2 are reported the components for EBIV and pressure acquisition and synchronization.

Table 3.2: Summary of the components for EBIV and pressure acquisition and synchronization.

Component	**Parameter**	**Value**
EB Cameras	Camera Model	Prophesee EVK-4 (×2)
	Sensor resolution	1280×720 px^2
	Lens	Nikon 28 mm
	f/D	2.8
	Spatial resolution	3.44 px/mm
	FOV	377.65×370.59 mm^2
CC algorithm	Interrogation windows (px)	128×128, 64×64, 48×48
	Overlap	50%, 75%, 75%
Laser Source	Laser Model	Lasertree LT-4LDS-V2
	Optical output power	20 W
	Wavelength (λ)	455 ± 10 nm
	Pulsing frequency (f_{laser})	500 Hz
	Duty cycle (DC)	25%
	Pulse width (t_{pulse})	500 μs
	Light sheet thickness	≈ 1 mm
Seeding System	Generator Model	LaVision HFSB
	Mean bubble diameter (d_p)	≈ 300 μm
	$St = t_p/t_0$	0.02-0.034 ($St \ll 1$)
PAS	Sensing plate dimensions	$72 \times 74 \times 2$ cm^3
	Transducer model	Honeywell (×5)
	Sampling rate	1 kHz
	Acquisition sampling	230 s
	Trigger	Arduino UNO Rev3

Chapter 4

Facility characterization

This chapter presents the flow field validation of the wind tunnel facility and the optimization results for the actuation system.

4.1 Hot-wire calibration for flow characterization

The calibration is performed by positioning the hot-wire probe at the center of the test section and measuring the free-stream velocity using a Pitot probe, both located 85 cm downstream to the test section inlet. The procedure involves 11 measurement points (except for the offset point at $U_\infty = 0$), acquired by varying the wind tunnel fan speed from 150 to 650 rpm with a constant increment of 50 rpm (fig. 4.1).

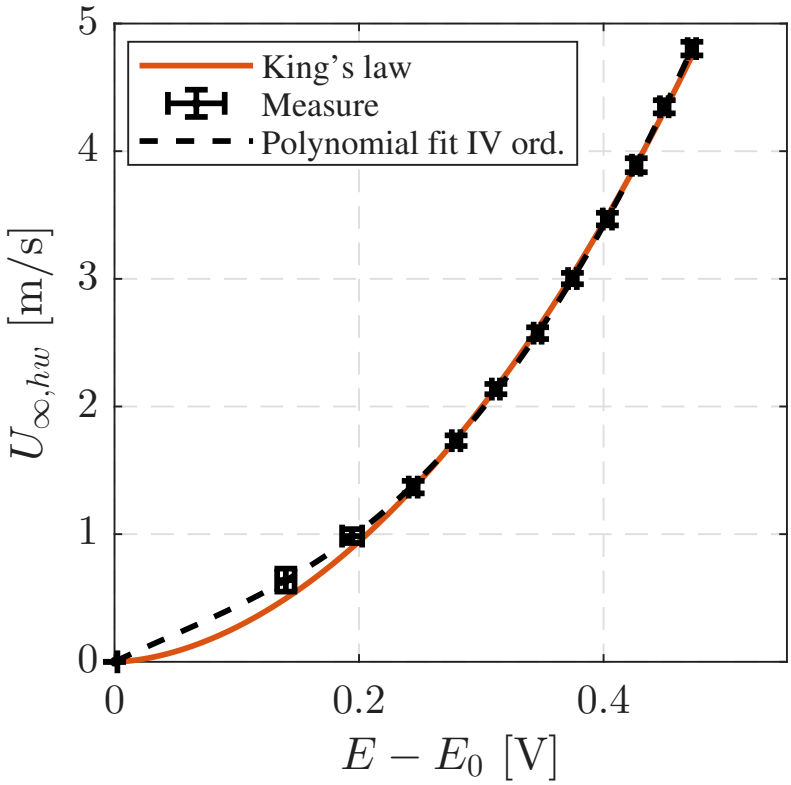


Figure 4.1: Calibration curve for the hot-wire probe.

4.2 Flow field characterization

Prior to the campaign test, a flow characterization was performed to verify velocity uniformity and to quantify the turbulence intensity (TI) [38] across the test section, which is defined as follows

$$TI = \frac{u_{rms}}{U} = \frac{1}{U}\sqrt{\frac{1}{N}\sum_{i=1}^{N}(u_i - U)^2} \tag{4.1}$$

where u_{rms} represents the standard deviation of the velocity fluctuations u': u_i is the instantaneous velocity and U is the mean velocity calculated over the sampling period. The flow characterization was performed by mapping the velocity field across three different longitudinal planes (x_1, x_2, and x_3). The first plane x_1 is located 85 cm downstream of the test section inlet, while x_2 and x_3 are positioned at further downstream intervals of 30 cm each (see tab. 4.1 to see the grid points). Measurements were carried out using a constant temperature Hot-Wire Anemometer (HWA) equipped with a single-wire probe. To sum up, the characterization[1] confirmed that the turbulence intensity remains consistently low across the investigated range, with values of $u_{rms}/U < 5\%$ for all tested freestream velocity, as reported in fig. 4.3.

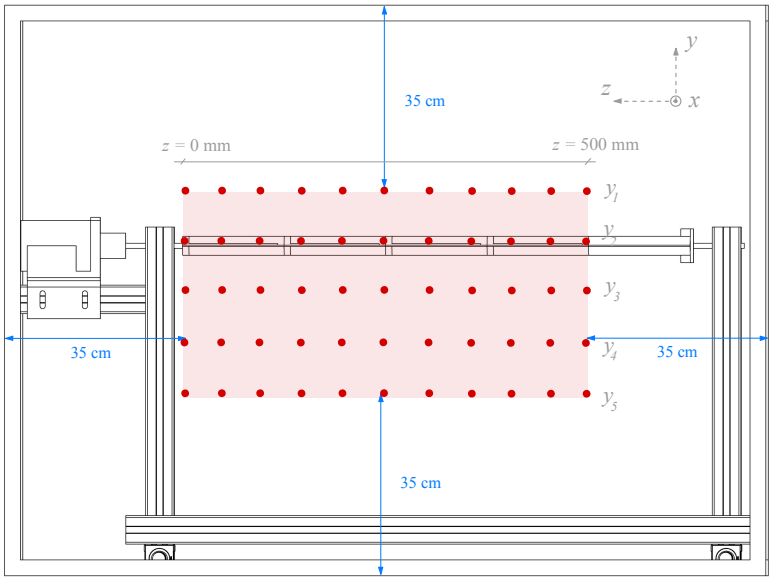
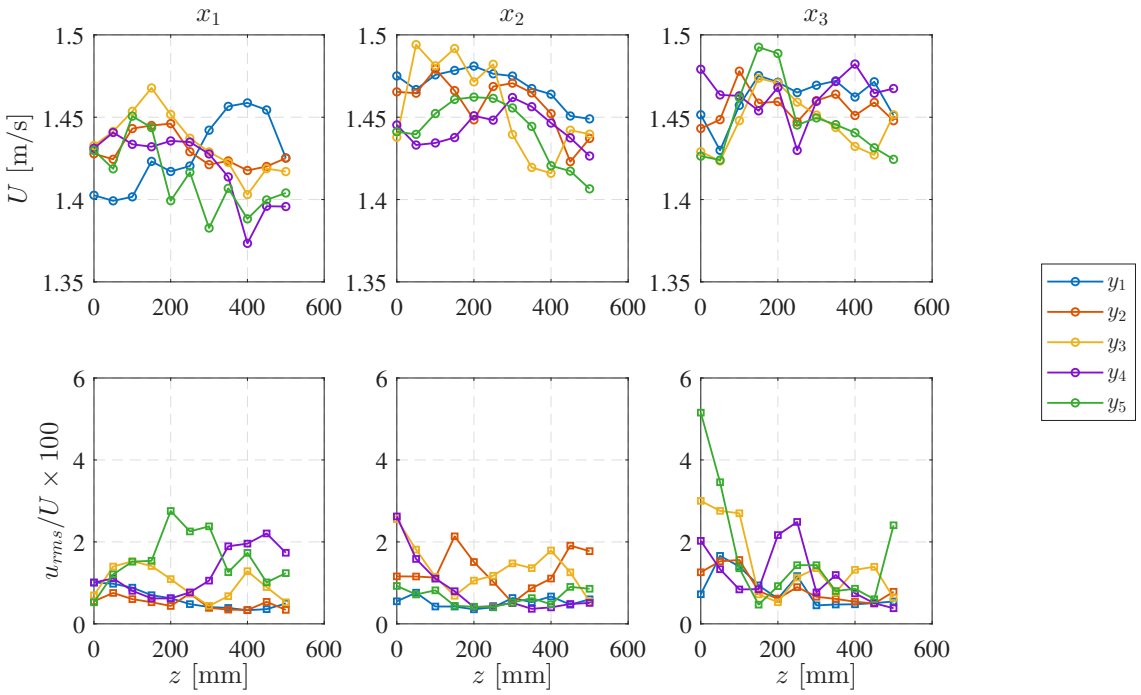
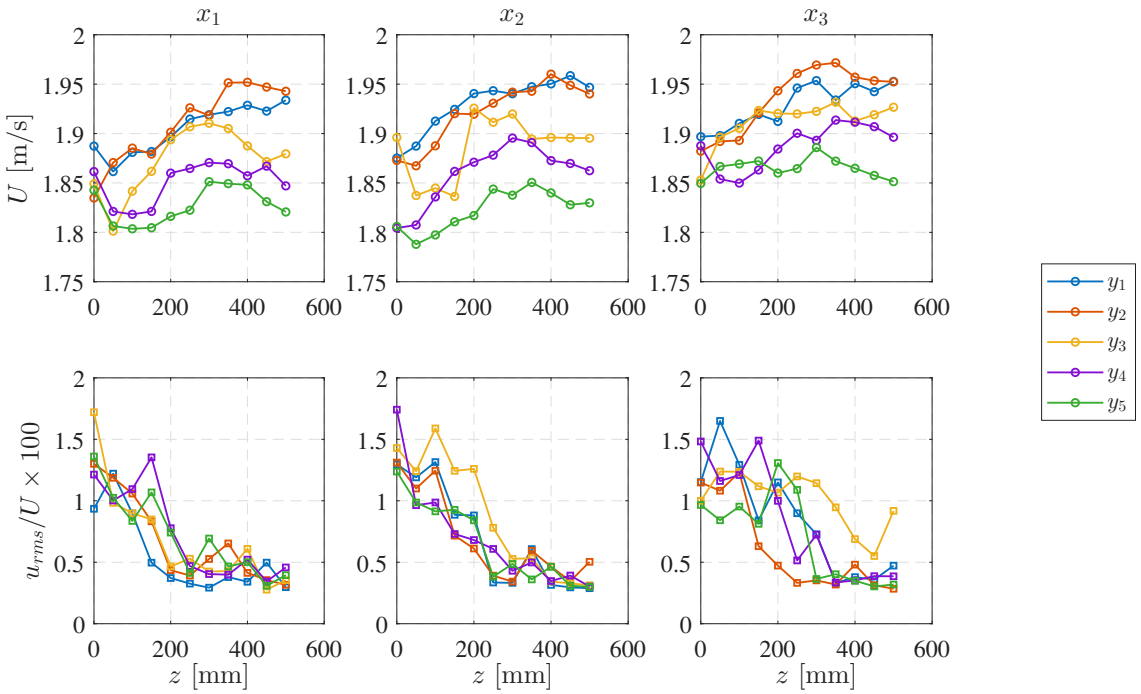


Figure 4.2: For each plane (i.e., x_1, x_2 and x_3), a grid of 55 measurement points was acquired to monitor both flow uniformity and turbulence levels ($t_s = 45$ s, $f_s = 10$ kHz). The vertical measurement points (y_1 to y_5) were spaced 5 cm apart, with y_5 being the closest coordinate to the wind tunnel lower wall.

[1]It should be noted that the freestream velocity $U_{\infty,hw}$ measured by the HWA may slightly deviate from the grid points, as the the velocity in the transversal plane is not perfectly uniform. However, the relative variation is $< 6\%$, ensuring sufficient flow homogeneity.



(a) Flow valitation tests performed at $U_{\infty,hw} \approx 1.5\,\mathrm{ms}^{-1}$.



(b) Flow valitation tests performed at $U_{\infty,hw} \approx 2.1\,\mathrm{ms}^{-1}$.

Figure 4.3: Profiles of mean velocity U (top, within each subfigure) and turbulence intensity u'/U (bottom, within each subfigure) at three axial planes x_1, x_2, x_3. Furthermore, other tests were performed respectively at $U_{\infty,hw} \approx 3\,\mathrm{ms}^{-1}$ and $U_{\infty,hw} \approx 3.5\,\mathrm{ms}^{-1}$ only for the first longitudinal plane x_1 (i.e., 85 cm downstream the test section inlet) and for both cases, the level of TI was found to be $< 5\%$. Ambient conditions: $T_{amb} = 20$ °C, $\rho_{amb} = 1.225$ kg/m^3.

4.3 Optimization actuation system

To ensure the best possible performance, an optimization of the control parameters for actuation system was performed (see sec. 3.2) through the encoder signals (see fig. 3.3). This tuning process focused on refining the speed and position loop gains to minimize overshoot and settling time. All tests were carried out with a sampling time of $t_s = 7$ s.

A campaign of five experimental tests was carried out to optimize the system's dynamic response by iteratively adjusting the control parameters (see fig. 4.4). The tuning focused first on the load-to-motor inertia ratio J_{load}/J_{motor}, a critical factor for stability that can range from 1:1 up to 120:1 for this specific drive. Through experimental observation, an optimal ratio of 7:1 was identified. Subsequently, the stiffness parameter was fine-tuned to achieve the best balance between response speed and vibration damping. This iterative approach allowed for the definition of an optimal configuration. Among the conducted trials, attempt 5 was selected as the optimal configuration ($\Delta t \approx 0.19\,\text{s}$, where Δt is the time between $t = 0$ s and the first peak of the dynamic response). The same campaign was carried out also for a slower rotation speed of the drive and it was found for the second case that $\Delta t \approx 0.46\,\text{s}$.

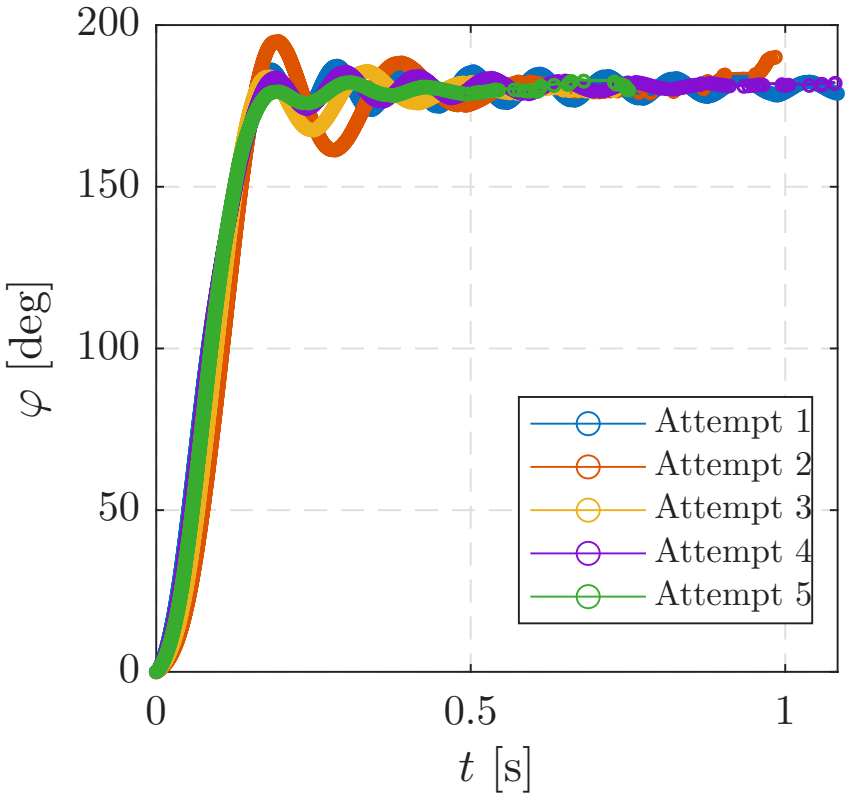


Figure 4.4: Dynamic response $\varphi(t)$ of the system during the optimization campaign. Each trajectory is time-shifted and aligned to the origin to evaluate the repeatability of the motor's dynamic response.

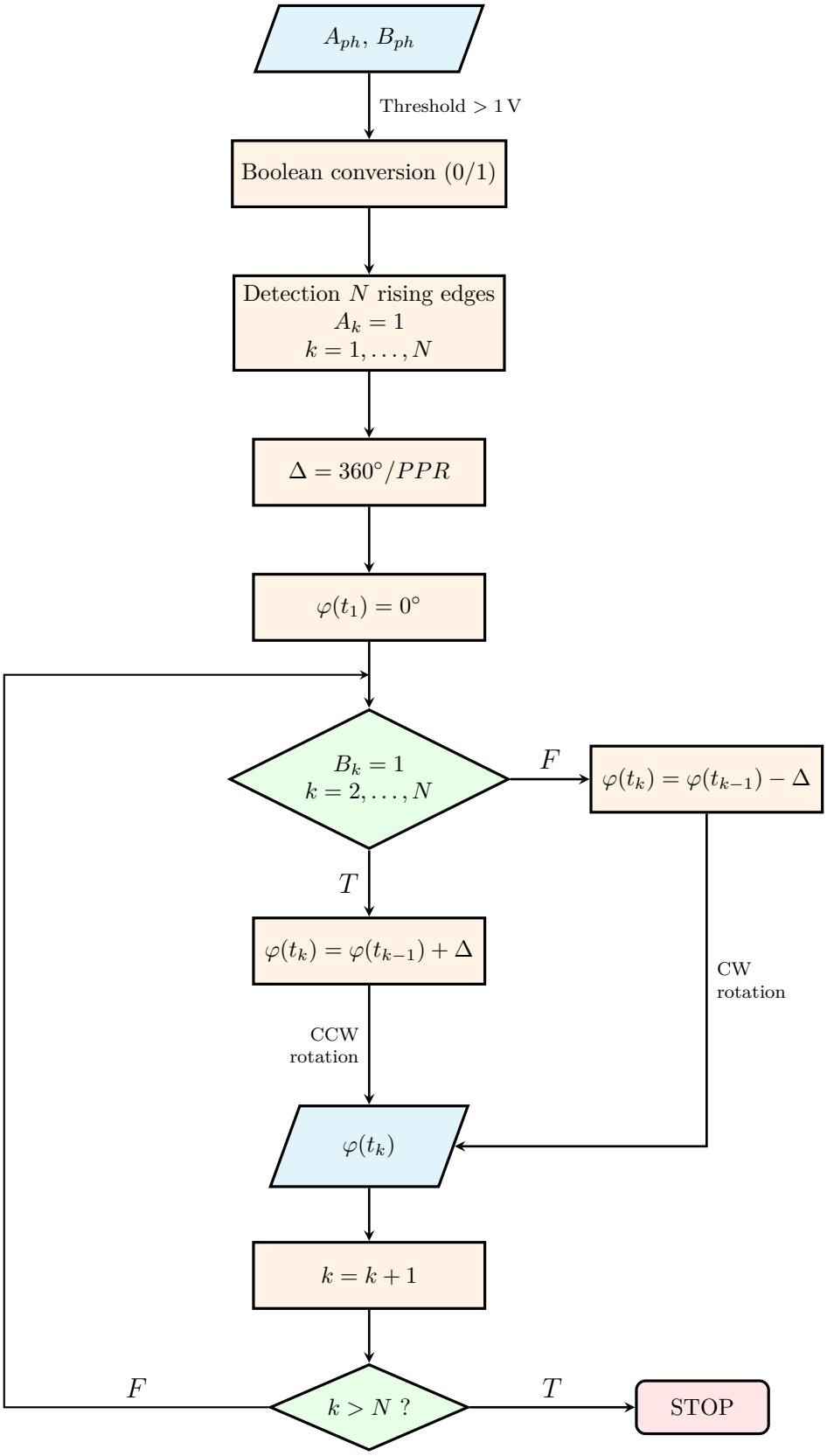


Figure 4.5: Flowchart of the decoding algorithm for dynamic response. Rotation direction is determined by the phase lead between A and B. If A leads over B the rotation will be clockwise (CW), otherwise will be counterclockwise (CCW). PPR represents the pulse per revolution.

Table 4.1: Grid of measurement points in the y–z plane, common to the three planes $x_i = 85$, 115, and 145 cm ($i = 1, \ldots, 3$), where x is measured from the test section inlet.

		z_1	z_2	z_3	z_4	z_5	z_6	z_7	z_8	z_9	z_{10}	z_{11}
y [cm] \ z [cm]		0	5	10	15	20	25	30	35	40	45	50
y_1	0	•	•	•	•	•	•	•	•	•	•	•
y_2	5	•	•	•	•	•	•	•	•	•	•	•
y_3	10	•	•	•	•	•	•	•	•	•	•	•
y_4	15	•	•	•	•	•	•	•	•	•	•	•
y_5	20	•	•	•	•	•	•	•	•	•	•	•

Chapter 5

Experimental results

This chapter details the mathematical formulation of the vortex model used to fit the experimental data and discusses the physical insights obtained from the results. The analysis is structured into two phases: the initial phase focuses on the baseline properties of the isolated vortex gust. It involves tracking the vortex trajectory, defining its characteristic core dimensions, and quantifying the gust ratio (GR).

Once the isolated vortex gust is fully characterized, the second part investigates the dynamic that occurs as the vortex interacts with a sensing flat plate positioned downstream.

5.1 Elliptical Lamb-Oseen Vortex Model

The velocity fields measured using Event-Based Imaging Velocimetry (EBIV) are modelled according to a modified Lamb–Oseen vortex formulation. The classical Lamb-Oseen model features an axisymmetric tangential velocity distribution [39, 40]. However, since experimental observations revealed that the vortex gust undergoes a progressive deformation throughout its spatial and temporal evolution, an elliptic core formulation was adopted to accurately capture this non-axisymmetric behaviour.

The fluctuating velocity components are extracted by subtracting the phase-averaged free-stream velocity (U_∞, V_∞) from the phase-averaged fields $(\bar{U}, \bar{V})$:

$$u'(\mathbf{x}, t) = \bar{U}(\mathbf{x}, t) - U_\infty, \tag{5.1}$$

$$v'(\mathbf{x}, t) = \bar{V}(\mathbf{x}, t) - V_\infty. \tag{5.2}$$

This subtraction isolates the velocity perturbation induced only by the vortex, removing the mean convective contribution. The elliptical Lamb–Oseen model is then applied to the perturbation field (u', v') only.

The global spatial coordinates are non-dimensionalised by the flat-plate chord length c, after shifting the origin to the trailing edge of the vortex gust generator

(see fig. 3.5):

$$X = \frac{x - x_0}{c},$$
$$Y = \frac{y - y_0}{c}.$$

5.1.1 Model formulation

The vortex centre is located at coordinates (x_c, y_c). A local reference frame is introduced, centred on the vortex core and rotated by the orientation angle ϑ of the semi-major axis with respect to the streamwise direction:

$$\begin{bmatrix} X_{\text{rot}} \\ Y_{\text{rot}} \end{bmatrix} = \begin{bmatrix} \cos\vartheta & \sin\vartheta \\ -\sin\vartheta & \cos\vartheta \end{bmatrix} \begin{bmatrix} x - x_c \\ y - y_c \end{bmatrix}. \tag{5.3}$$

The elliptic aspect ratio is defined as:

$$e = \frac{b}{a} \leq 1, \tag{5.4}$$

where a and b are the semi-major and semi-minor axes of the elliptic core, respectively. An effective radius that maps the elliptic domain onto a scalar distance is then introduced:

$$R_{\text{eff}} = \sqrt{X_{\text{rot}}^2 + \left(\frac{Y_{\text{rot}}}{e}\right)^2}. \tag{5.5}$$

For $e = 1$ the classical axisymmetric Lamb–Oseen vortex is recovered. The tangential velocity follows the Lamb–Oseen profile scaled to R_{eff}:

$$u_\theta(R_{\text{eff}}) = \frac{\Gamma}{2\pi R_{\text{eff}}} \left[1 - \exp\left(-\frac{R_{\text{eff}}^2}{a^2}\right)\right], \tag{5.6}$$

where Γ is the total circulation of the vortex. This velocity is projected onto the rotated axes to obtain the local Cartesian components:

$$U_{\text{rot}} = -u_\theta \frac{Y_{\text{rot}}}{e \cdot R_{\text{eff}}}, \tag{5.7}$$

$$V_{\text{rot}} = \quad u_\theta \frac{X_{\text{rot}}}{R_{\text{eff}}}. \tag{5.8}$$

Rotating back to the global frame gives the final model velocity field:

$$U_{\text{mod}} = U_{\text{rot}} \cos\vartheta - V_{\text{rot}} \sin\vartheta, \tag{5.9}$$

$$V_{\text{mod}} = U_{\text{rot}} \sin\vartheta + V_{\text{rot}} \cos\vartheta. \tag{5.10}$$

5.1.2 Vortex centre detection and initial parameter estimation

Before the nonlinear optimisation is launched, an initial estimate of the model parameters is computed directly from the experimental vorticity field $\omega = \partial v'/\partial x - \partial u'/\partial y$.

As far as the vortex centre is concerned, a binary mask is constructed by retaining grid points where $|\omega| \geq 0.6\,\max(|\omega|)$. Connected regions are identified and the largest one is selected. Its vorticity centroid provides the initial estimate $(x_c^{(0)}, y_c^{(0)})$. The threshold value was selected empirically by verifying that lower values caused background noises unrelated to the actual vorticity.

The shape and orientation of the elliptic core are estimated from the spatial distribution of the vorticity field. A small background threshold is subtracted before to remove noise outside the core region; the resulting field is denoted as $\tilde{\omega}$. The idea is to treat ω as a scalar weight function and compute its second-order central moments M_{20}, M_{02} and M_{11}

$$M_{20} = \frac{\sum_i (x_i - x_c^{(0)})^2\,\tilde{\omega}_i}{\sum_i \tilde{\omega}_i},$$

$$M_{02} = \frac{\sum_i (y_i - y_c^{(0)})^2\,\tilde{\omega}_i}{\sum_i \tilde{\omega}_i},$$

$$M_{11} = \frac{\sum_i (x_i - x_c^{(0)})(y_i - y_c^{(0)})\,\tilde{\omega}_i}{\sum_i \tilde{\omega}_i}.$$

which measure how the vorticity is spread and correlated along the two spatial directions. These three moments are assembled into the inertia matrix $\mathbf{M}$:

$$\mathbf{M} = \begin{pmatrix} M_{20} & M_{11} \\ M_{11} & M_{02} \end{pmatrix}. \tag{5.11}$$

Since $\mathbf{M}$ is symmetric, its eigen-decomposition yields two orthogonal principal directions and two eigenvalues $\lambda_{\max} \geq \lambda_{\min} > 0$, which represent the variance of the vorticity distribution along each axis. The initial semi-axes and orientation angle are then estimated as:

$$a^{(0)} = \sqrt{\lambda_{\max}}, \qquad b^{(0)} = \sqrt{\lambda_{\min}}, \qquad \vartheta^{(0)} = \operatorname{atan2}(v_2,\, v_1), \tag{5.12}$$

where (v_1, v_2) is the eigenvector associated with $\lambda_{\max}$.

5.1.3 Model Fitting and Optimisation

The optimisation seeks the parameter vector

$$\mathbf{p} = \left[x_c,\ y_c,\ a,\ b,\ \Gamma,\ \vartheta\right] \tag{5.13}$$

that minimises the L_2 residual between the model (5.9)–(5.10) and the experimental perturbation field (u', v') over the entire measurement domain. The parameters U_0, V_0 (uniform background translation) and the linear shear gradients $\partial U/\partial y$, $\partial V/\partial x$ are included in the model implementation but are constrained to zero, as the free-stream subtraction (5.2) already removes the mean convective contribution.

To limit the influence of localised measurement noise, such as laser reflections near the flat plate or artefacts in the EBIV data, a pseudo-Huber penalty is applied to each velocity residual $\Delta u = u' - U_{\mathrm{mod}}$ and $\Delta v = v' - V_{\mathrm{mod}}$, with an adaptive threshold $\delta = 0.1 \max\left(\|\mathbf{u}'\|_\infty, \|\mathbf{v}'\|_\infty\right)$ computed for each snapshot. This formulation behaves quadratically for small residuals and linearly for large outliers, reducing their influence on the final result.

The optimisation is carried out with MATLAB's `lsqnonlin`, with step and function tolerances of 10^{-8} and a maximum of 12 000 iterations.

From the second snapshot onwards, the initial guess and the parameter bounds are inherited from the previous frame to ensure physically consistent tracking. Specifically, the semi-axes (a, b), orientation angle (ϑ) and circulation (Γ) are constrained within their previous values; the vortex centre is re-estimated from the vorticity centroid of the current snapshot but bounded within a narrow spatial tolerance. This adaptive windowing prevents unphysical jumps between frames while tracking the gradual deformation of the vortex core.

5.1.4 Circulation measurments

After the nonlinear fit, the circulation shed from the trailing edge is re-estimated directly from the experimental vorticity field to enforce physical consistency between the model and the measurements. By using Stokes theorem, the circulation contained within the fitted elliptic core σ is:

$$\Gamma_{\mathrm{exp}} = \iint_\sigma \omega_z \, \mathrm{d}A, \qquad \sigma = \left\{ (x, y) : \left(\frac{X_{\mathrm{rot}}}{a}\right)^2 + \left(\frac{Y_{\mathrm{rot}}}{b}\right)^2 \leq 1 \right\}.$$

For a Lamb–Oseen vortex, the fraction of total circulation enclosed within a circle of radius $r = a$ is:

$$\frac{\Gamma(r \leq a)}{\Gamma_\infty} = 1 - e^{-1} \approx 0.632. \tag{5.14}$$

Inverting this relation, the total circulation Γ_∞ is recovered from the core-integrated measurement:

$$\Gamma_\infty = \frac{\Gamma_{\mathrm{exp}}}{1 - e^{-1}}. \tag{5.15}$$

This value is then substituted back into the model (5.6) (5.10), overwriting the fitted Γ. This two-step procedure (i.e., fit the geometry, then enforce the circulation from data) decouples the shape optimisation from the circulation estimate, improving the overall robustness of the model. Lastly, the circulation is later non-dimensionalized using the freestream velocity U_∞ and the flat plate chord length c.

5.2 Isolated Vortex Gust

The facility used for the vortex gust characterization was widely explained before in the previous chapter 3. The vortex gust was generated by one half of a clockwise rotation of a gust generator plate. Imposing a negative rotation on the gust generator at the start of the motion induces the shedding of an intense vortex from the flat plate's trailing edge. This vortex exhibits a counter-clockwise rotation and positive circulation Γ. The characterization of the isolated vortex gust relies on this first and intense vortex.

In order to characterize the vortex gust, for all test cases, we adopted the normalized convective time criteria, which also means a fixed streamwise coordinate x/c. After an iterative method, it was picked $x/c = 0.6$. This specific position was selected because it captures the vortex development at a downstream coordinate that ensures a complete characterization of the isolated gust just before it impacts the sensing flat plate located downstream for the second phase of the experiment. It is worth noting that the outputs of the vortex characterization strongly depend on the specific physical instant selected for the analysis. As the vortex is advected downstream, its shape, core dimensions, and deformation evolve continuously due to convective transport and interaction with the ambient flow.

Furthermore, for all test cases, the rotation time of the flat plate maneuver is $\Delta t \approx 0.46$ s (see sec. 4.3), which can be quantitatively non-dimensionalized to yield the convective rotation time

$$\Delta t^* = \frac{U_\infty \Delta t}{c}.$$

The experimental gust ratio $GR(\vartheta)$ was computed by evaluating the velocity field along the perimeter of the elliptical core. At each point, the local velocity was projected onto the tangent direction of the ellipse to obtain the tangential velocity component. The mean absolute tangential velocity $\overline{u}_\vartheta$ was then averaged over the entire perimeter and normalized by the free-stream velocity U_∞, yielding the gust ratio

$$GR(\vartheta) = \frac{\overline{u}_\vartheta}{U_\infty}.$$

The parameters for all test cases are summarized below in tab. 5.1.

Table 5.1: Experimental test matrix for vortex gust characterization.

	$U_\infty\,[\mathrm{ms}^{-1}]$	Re	Δt^*	t^*
Test case 1	1	2×10^4	1.533	1.270
Test case 2	1.4	2.8×10^4	2.146	1.306
Test case 3	1.8	3.6×10^4	2.760	1.396

5.2.1 Results overview

Tab. 5.2 show a detailed overview of vortex gust characterization results. Figures 5.1, 5.4, 5.7 show the normalized out of plane vorticity contourplots for all investigated cases. Figures 5.2, 5.5, 5.8, show instead the normalized longitudinal (U_g/U_∞) and trasnversal (V_g/U_∞) gust components for experimental and model data. Lastly, figures 5.3, 5.6, 5.9, show the spatio-temporal evolution of the gust ratio and non-dimensionalized vortex core diameter ($D_c/c = 2\sqrt{a \times b}/c$). ε represents the relative error between experimental data and model results.

Table 5.2: Comparison among vortex gust characterization results for all experiments.

	Test 1	**Test 2**	**Test 3**
U_∞ [ms^{-1}]	1.0	1.4	1.8
t^*	1.270	1.306	1.396
t [s]	0.381	0.280	0.231
x_c/c	0.602	0.604	0.605
y_c/c	-0.437	-0.418	-0.339
D_c [cm]	8.027	8.201	8.484
D_c/c	0.268	0.273	0.283
Γ_{exp} [m^{2}s^{-1}]	0.324	0.426	0.474
Γ_{mod} [m^{2}s^{-1}]	0.313	0.424	0.457
ε_Γ	3.43%	0.59%	3.45%
$GR_{\text{exp}}(\vartheta)$	1.295	1.197	1.003
$GR_{\text{mod}}(\vartheta)$	1.251	1.188	0.967
ε_{GR}	3.40%	0.80%	3.50%
$\lvert U_{g,\max}\rvert/U_\infty$	1.387	1.038	0.664
$\lvert V_{g,\max}\rvert/U_\infty$	1.391	1.017	0.688

Based on the instant of the characterization, the vortex core size was found to be approximately constant. This means that for all experiments, the gust width (i.e., the equivalent vortex core dimension) was found to have a constant width-to-chord ratio of $D_c/c \approx 0.27$ at $t^* = 1.3$. Unlike the vortex core dimension, the gust ratio $GR(\vartheta)$ slightly decrease with freestream velocity, whereas the circulation shows an opposite trend. The findings does have a physical basis because the time rotation of the vortex gust generator is the same for all experiments, which was $\Delta t \approx 0.46\,\text{s}$.

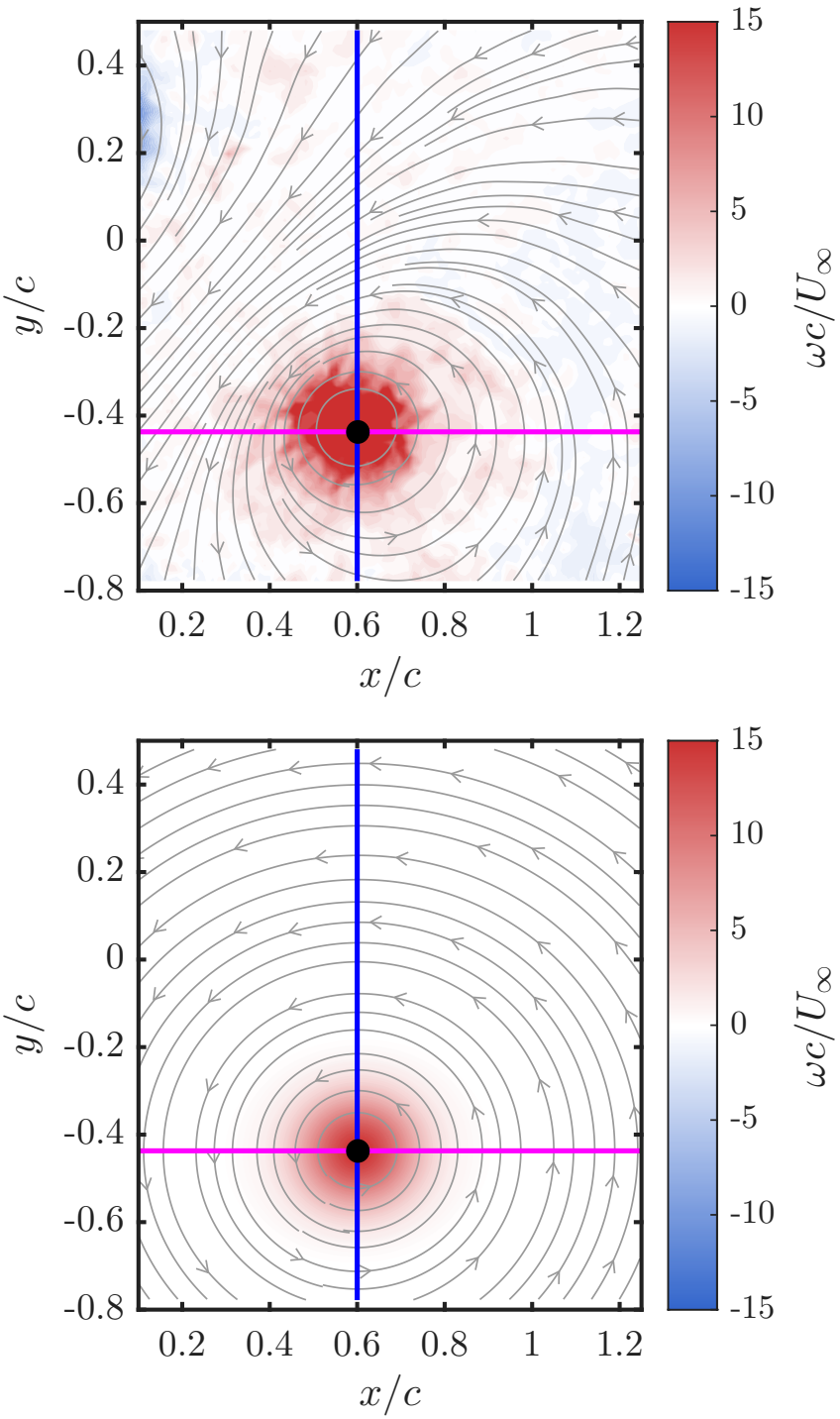


Figure 5.1: Normalized out of plane vorticity contourplots at the coordinate $x/c = 0.6$: comparison between the experimental phase-averaged field (top, one velocity vector plotted every 4 grid points) and the fitted elliptical model (bottom) for $U_\infty \approx 1.0\,\mathrm{ms}^{-1}$ and $Re \approx 2 \times 10^4$.

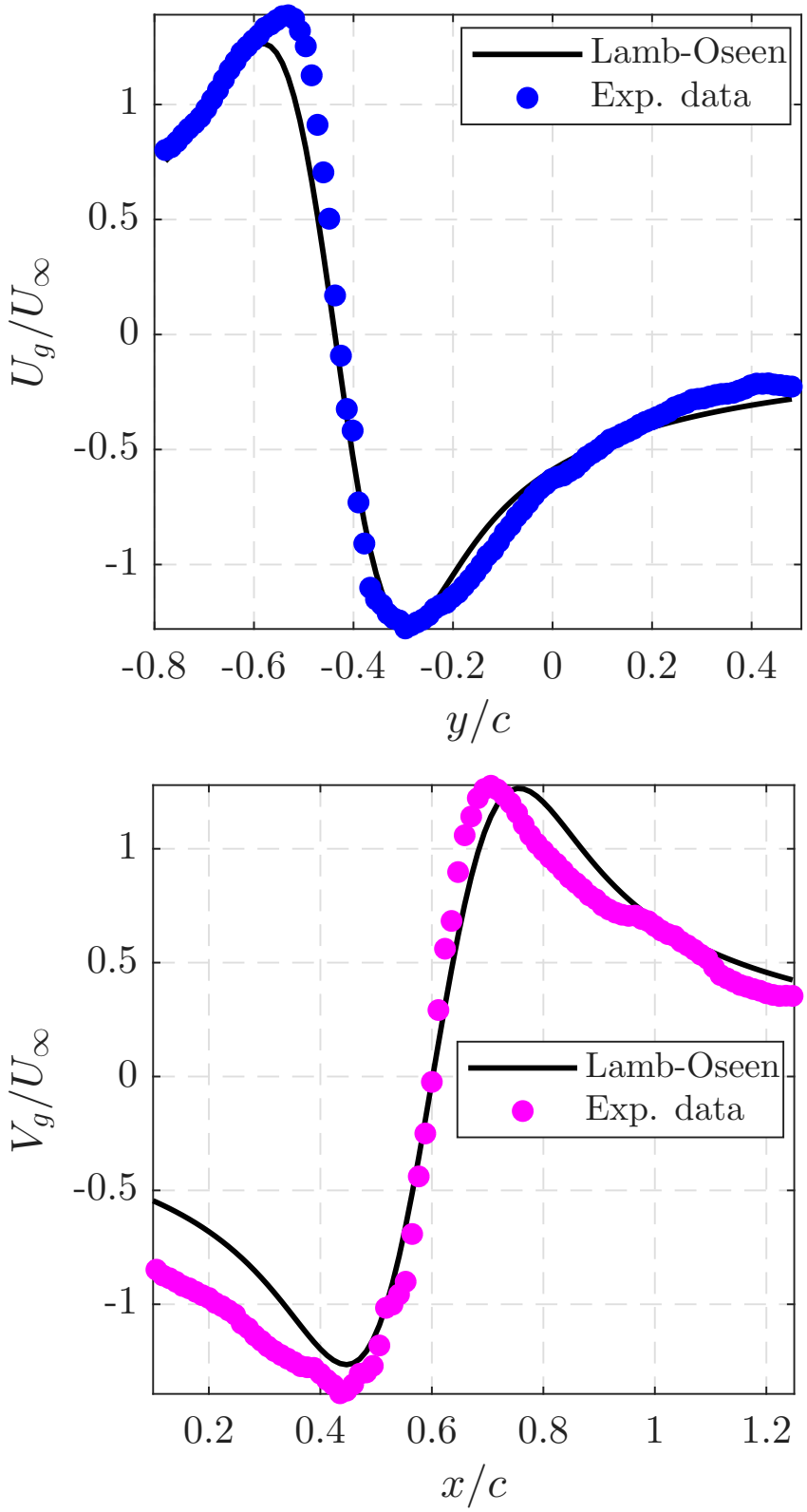


Figure 5.2: Normalized longitudinal gust velocity U_g/U_∞ (•) and normalized transversal gust velocity V_g/U_∞ (•) at $x/c = 0.6$ for $U_\infty \approx 1.0\,\mathrm{ms}^{-1}$ and $Re \approx 2{\times}10^4$.

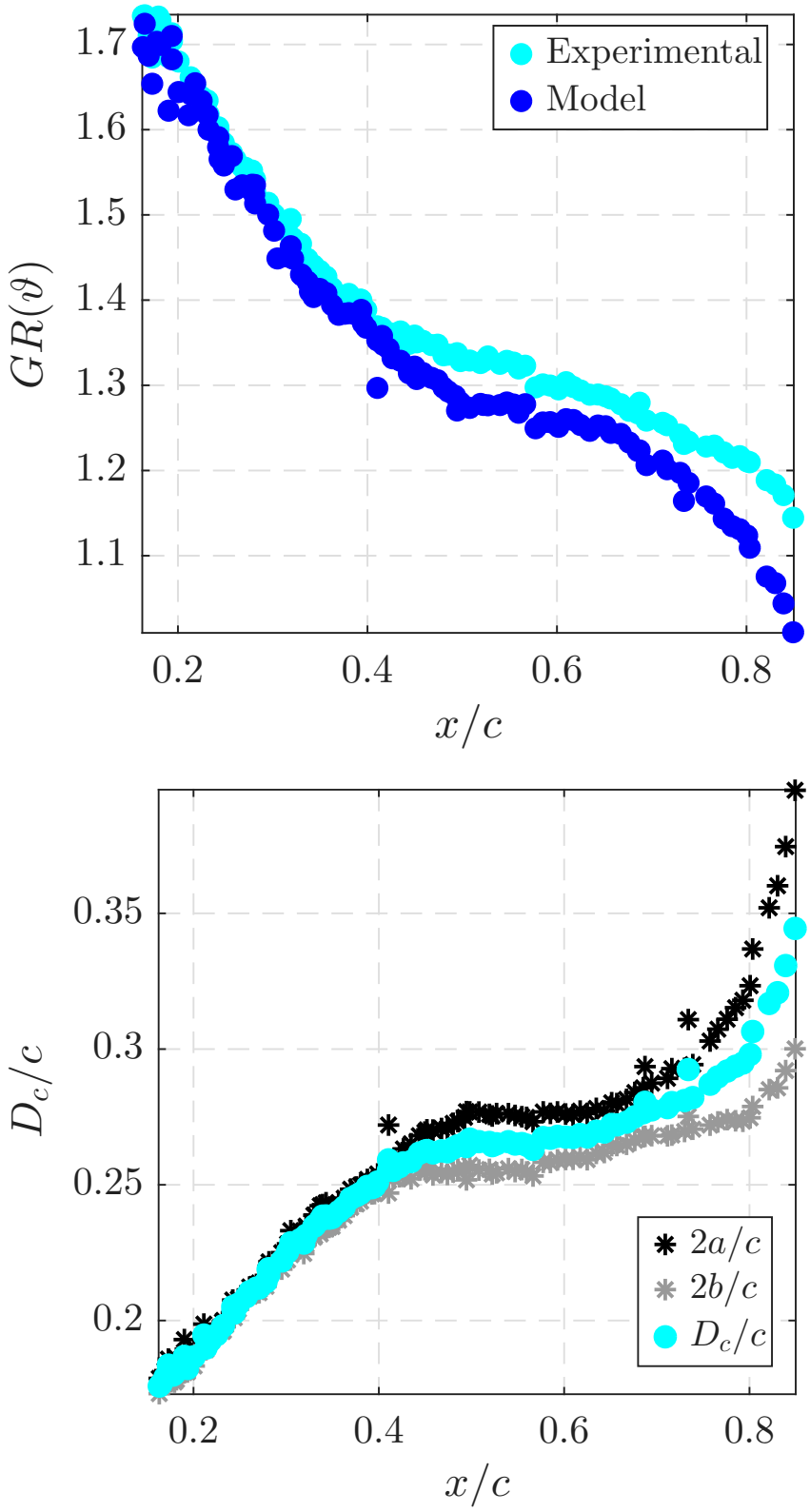


Figure 5.3: Experimental and numerical gust ratio $GR(\vartheta)$ (top) and normalized vortex core diameter D_c/c (bottom) during their spatio-temporal evolution for $U_\infty \approx 1.0\,\mathrm{ms}^{-1}$ and $Re \approx 2 \times 10^4$.

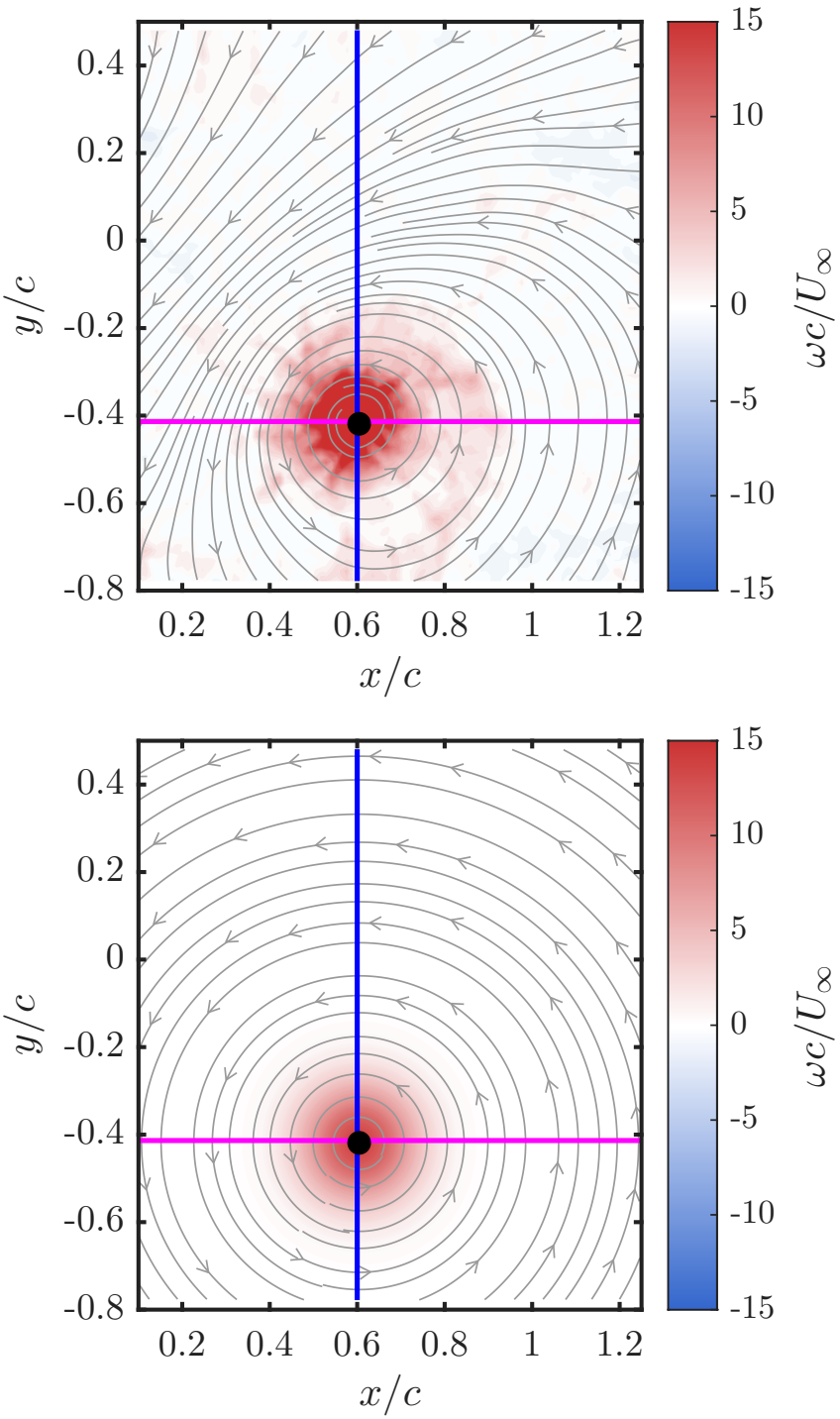


Figure 5.4: Normalized out of plane vorticity contourplots at $x/c = 0.6$: comparison between the experimental phase-averaged field (top, one velocity vector plotted every 4 grid points) and the fitted elliptical model (bottom) for $U_\infty \approx 1.4\,\mathrm{ms}^{-1}$ and $Re \approx 2.8 \times 10^4$.

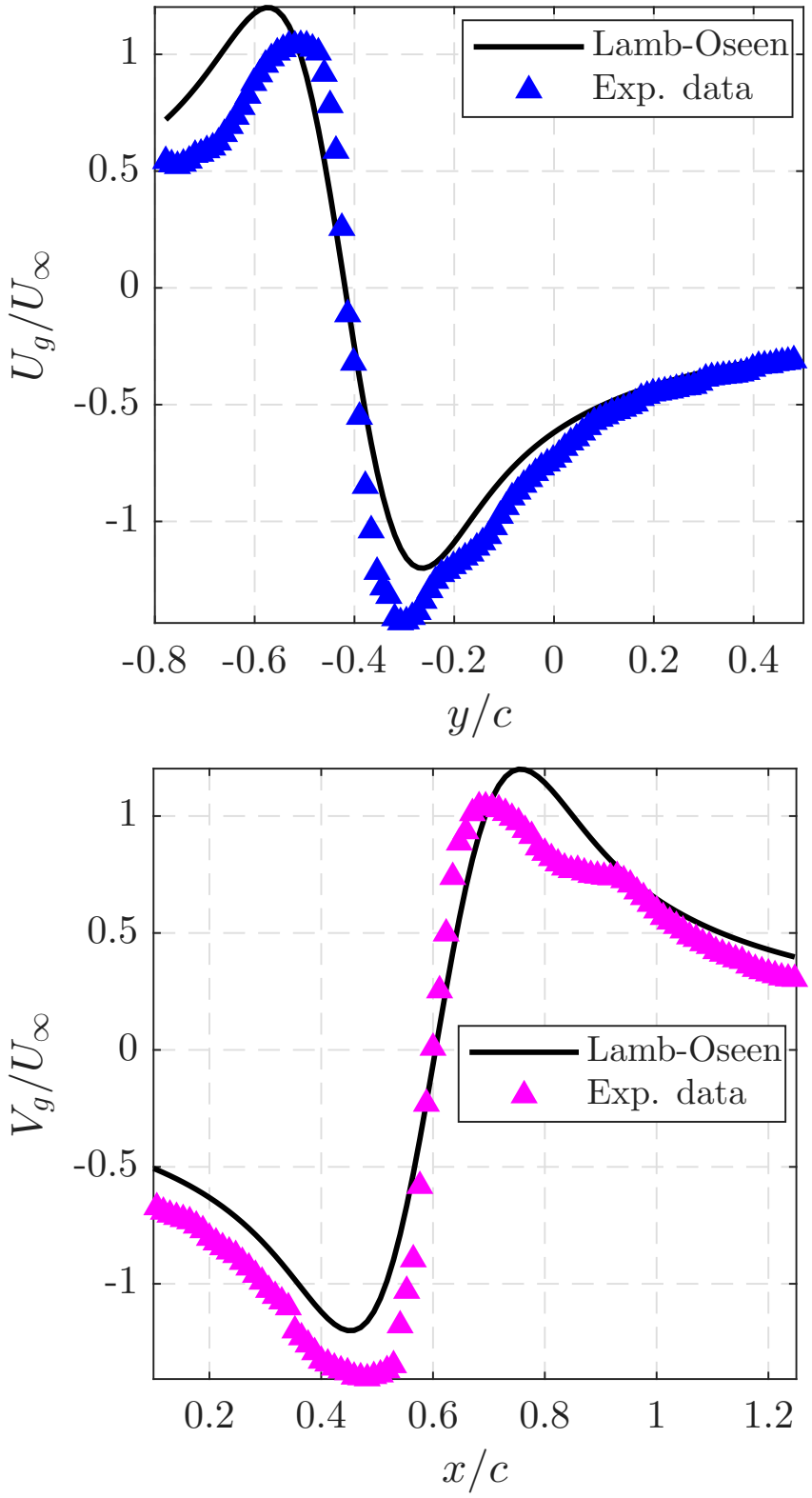


Figure 5.5: Normalized longitudinal gust velocity U_g/U_∞ (▲) and normalized transversal gust velocity V_g/U_∞ (▲) at $x/c = 0.6$ for $U_\infty \approx 1.4\,\mathrm{ms}^{-1}$ and $Re \approx 2.8 \times 10^4$.

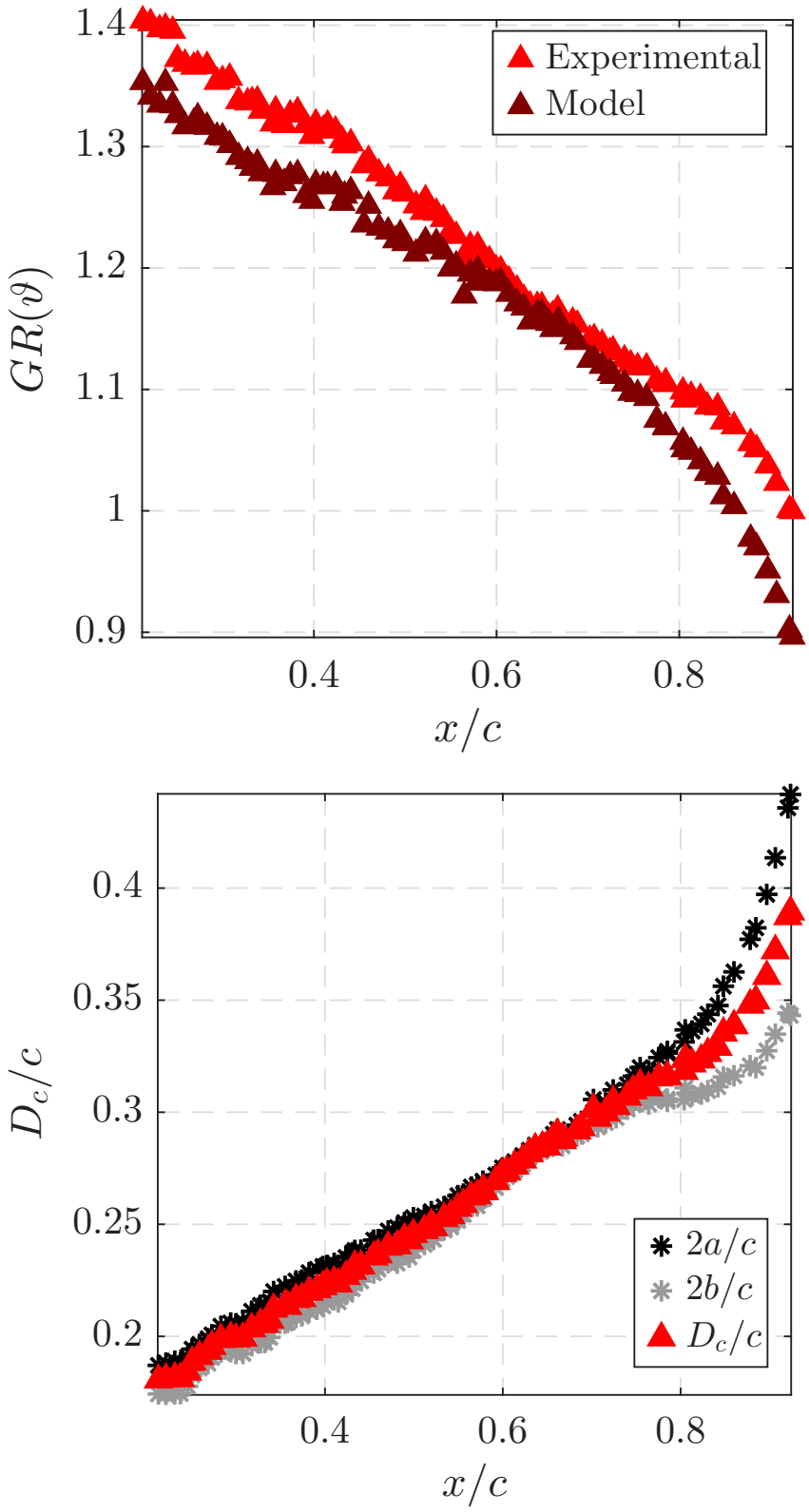


Figure 5.6: Experimental and numerical gust ratio $GR(\vartheta)$ (top) and normalized vortex core diameter D_c/c (bottom) during their spatio-temporal evolution for $U_\infty \approx 1.4\,\mathrm{ms}^{-1}$ and $Re \approx 2.8 \times 10^4$.

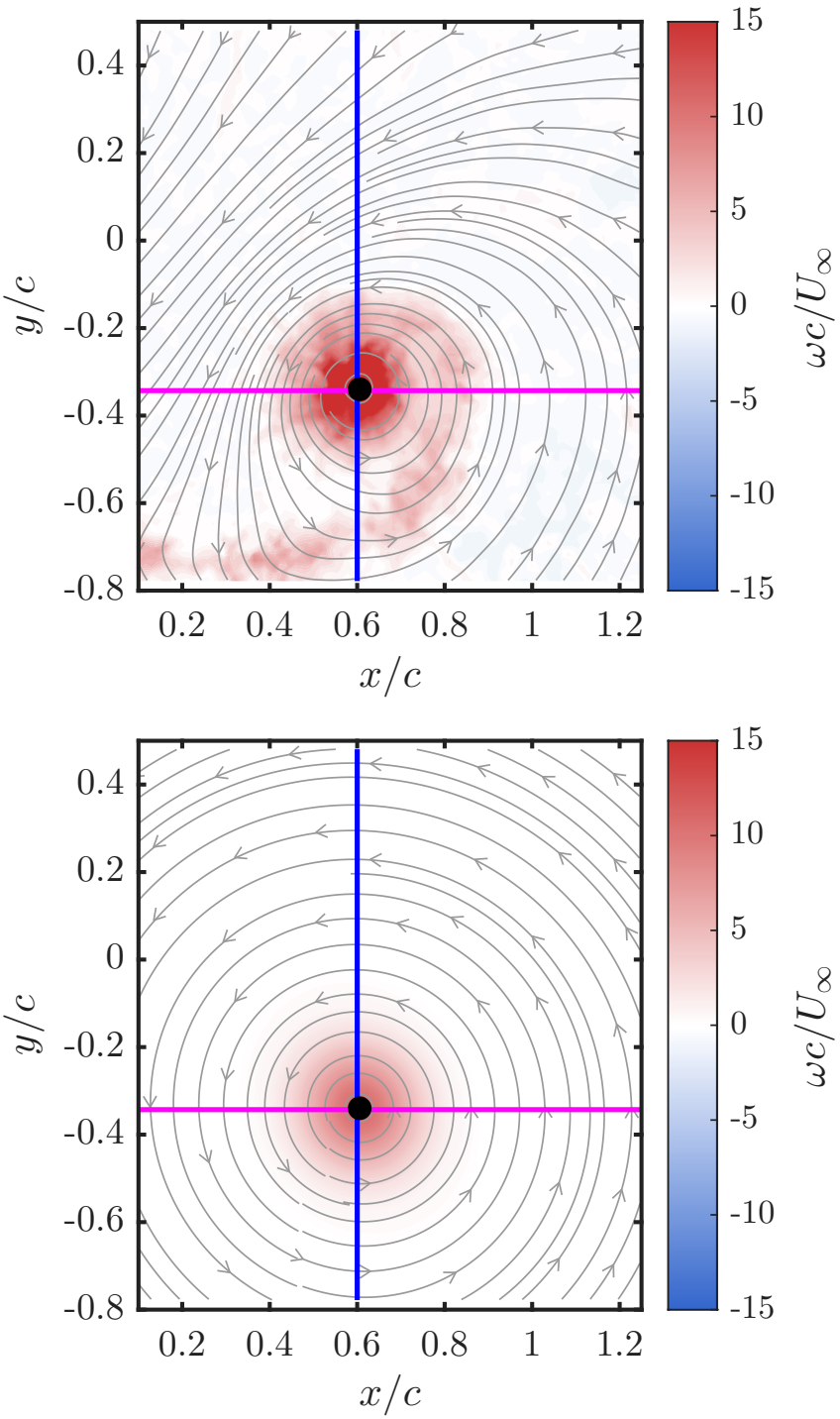


Figure 5.7: Normalized out of plane vorticity contourplots at $x/c = 0.6$: comparison between the experimental phase-averaged field (top, one velocity vector plotted every 4 grid points) and the fitted elliptical model (bottom) for $U_\infty \approx 1.8\,\mathrm{ms}^{-1}$ and $Re \approx 3.6 \times 10^4$.

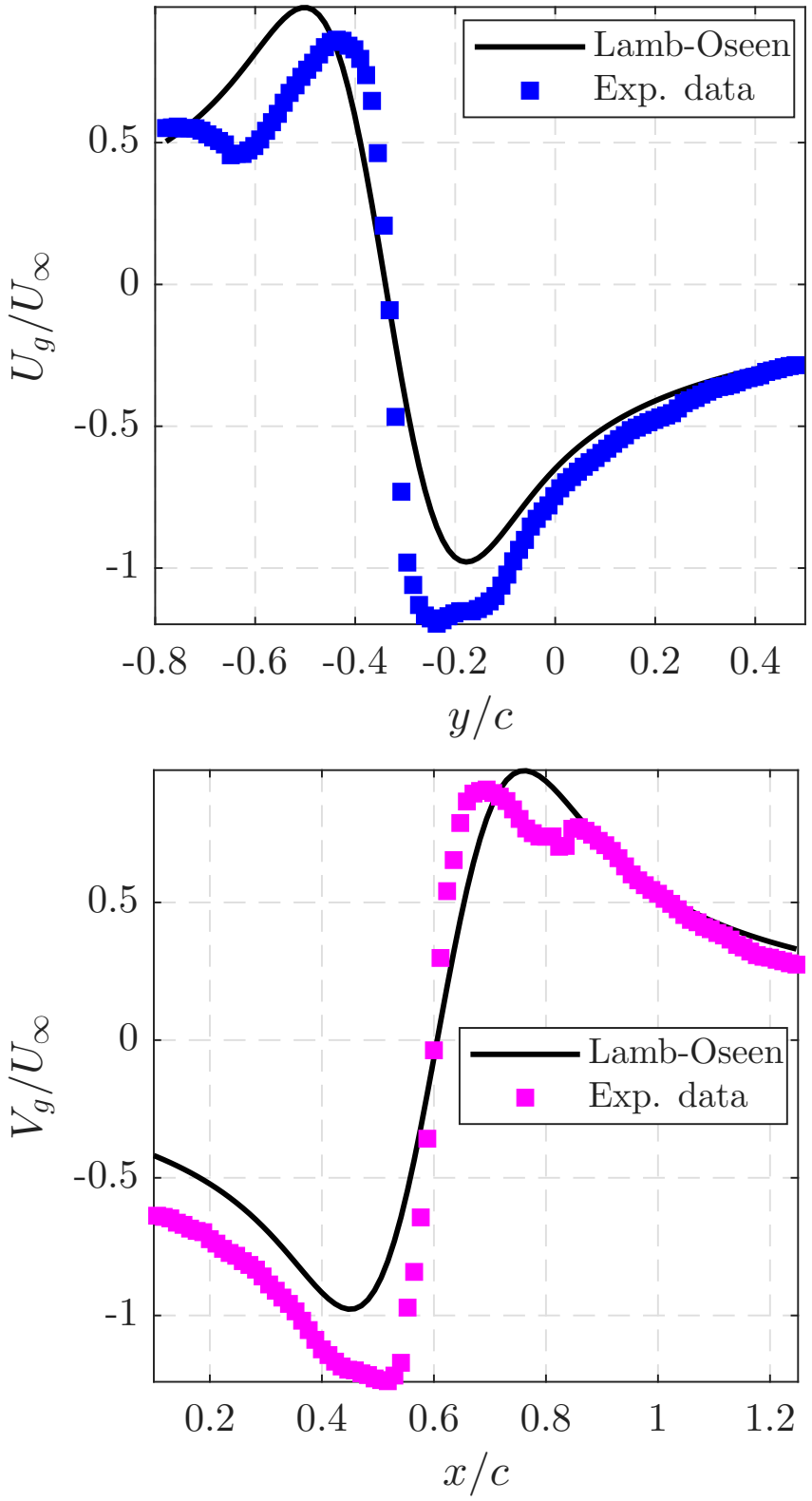


Figure 5.8: Normalized longitudinal gust velocity U_g/U_∞ (■) and normalized transversal gust velocity V_g/U_∞ (■) at $x/c = 0.6$ for $U_\infty \approx 1.8\,\mathrm{ms}^{-1}$ and $Re \approx 3.6 \times 10^4$.

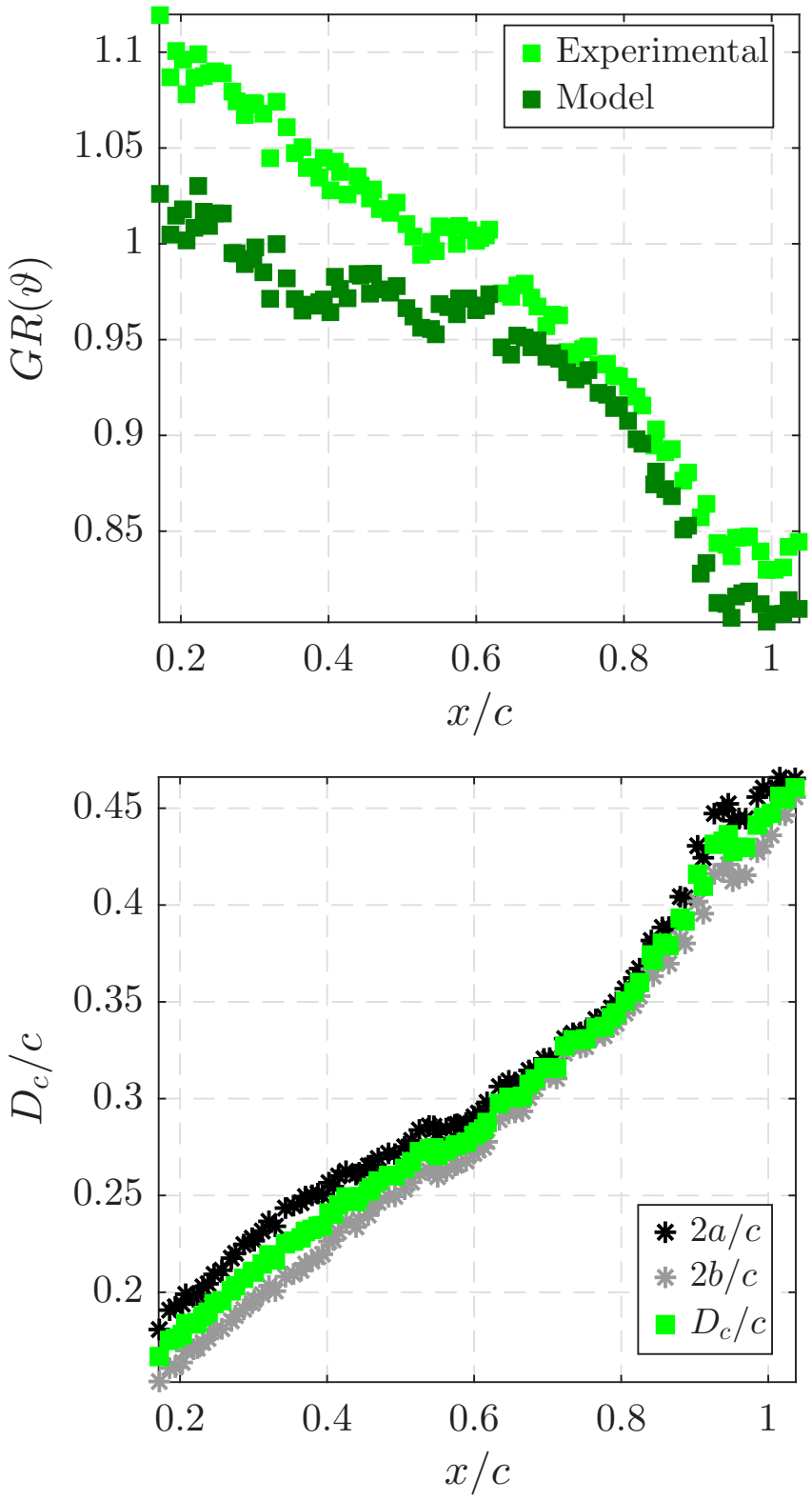


Figure 5.9: Experimental and numerical gust ratio $GR(\vartheta)$ (top) and normalized vortex core diameter D_c/c (bottom) during their spatio-temporal evolution for $U_\infty \approx 1.8\,\mathrm{ms}^{-1}$ and $Re \approx 3.6 \times 10^4$.

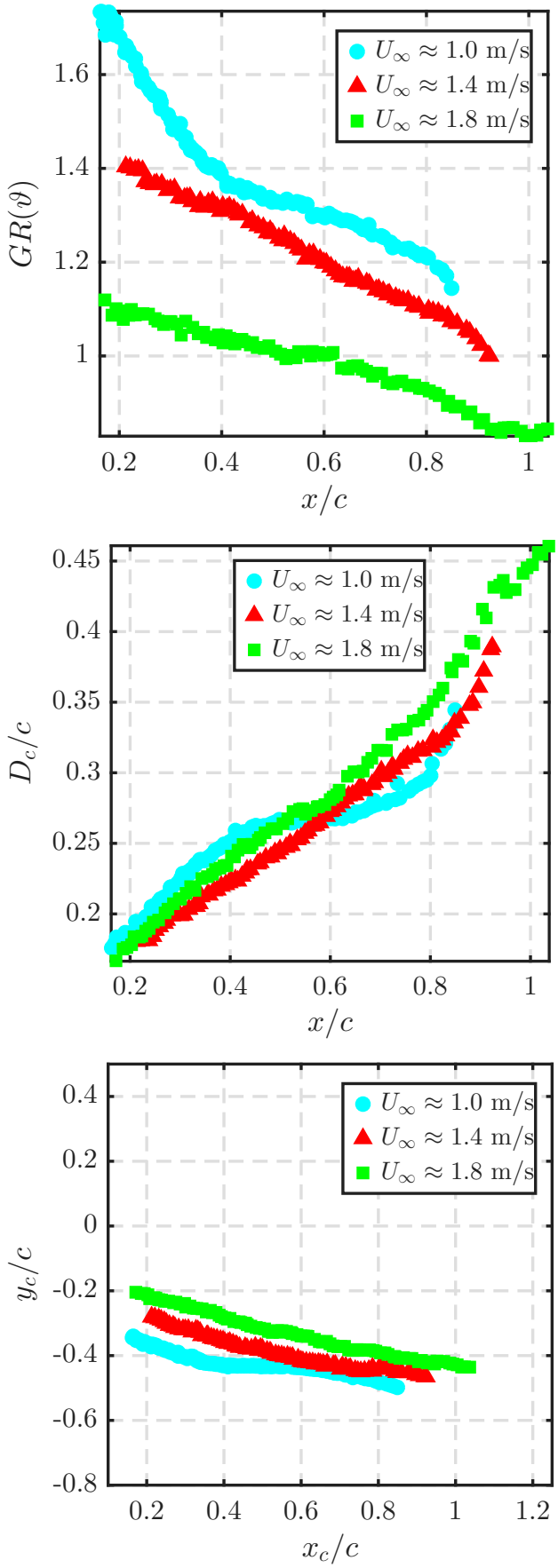


Figure 5.10: Evolution of gust ratio $GR(\vartheta)$ (top), vortex core diameter D_c/c (middle), and vortex core center trajectories (bottom) across all flow conditions.

Given that, the tangential speed $\overline{u}_\vartheta$ stays roughly constant; hence the gust ratio slightly drops with U_∞. On the other hand, both gust velocity components U_g and V_g raise with freestream velocity, as does the vortex core circulation Γ. The key relies on the fact that we are characterizing the isolated vortex at the same coordinate x/c but the physical time t from the start of motion of gust generator differs among tests; this aspect means that the freestream velocity has a crucial impact on the deformation of the core during its evolution.

Lastly, in fig. 5.10 is outlined the comparison among experiments. It is important to notice how the evolution of gust ratio for the first case presents a non-linear behaviour while travelling rather than the other cases, which show a linear behaviour with decreasing slope for the second and third case respectively.

5.2.2 Model validation

The results represent another metric to validate the elliptical model. Across all three flow conditions, the numerical model shows good overall agreement with the experimental data, correctly capturing the general trend of circulation growth along the chord. For the first test case, the non-dimensionalized circulation begins near unity and rises moderately, reaching ≈ 1.25 toward the trailing edge. The model slightly underpredicts the experimental values in the region $x/c > 0.4$. The relative error ε_Γ shows excellent trend, which remains below 6% for most of the traveled distance. As we expect, ε_Γ increase with Γ/cU_∞. In particular, when the vortex core approaches the boundaries of the overall FOV, the relative error tends to increase.

For the second freestream condition, the circulation starts at a lower value but rises more steeply, exceeding 1.2. Agreement here is excellent throughout most of the chord, except for $x/c > 0.8$ where the model slighlty deviate from experimental data. Also in this case, the relative error ε_Γ remains below 6% up to $x/c < 0.8$.

In the third case, the trend is similar but more gradual in the initial region, with values rising from ≈ 0.6 to ≈ 1.15. The model again follows the data well. The relative error distribution shows a somewhat distinctive behaviour compared to the other two speeds; the relative error is much larger when the vortex core appears to the FOV. Then, it shows a decreasing trend up to $x/c \approx 0.7$, followed by a rising trend.

Generally speaking, the model fits pretty well experimental data, showing an error which overall remains below 12% for all flow condition. It is worth noticing that the data were processed only by phase-averaging data. No Gaussian filter has been applied to the data.

To prove the quality of the elliptical model, the root mean square error (RMSE) was computed over the evolution of gust ratio for each experiment

$$\widetilde{GR} = \sqrt{\frac{1}{N}\sum_{i=1}^{N}\left[GR_{\text{exp}}\left(\frac{x_i}{c}\right) - GR_{\text{mod}}\left(\frac{x_i}{c}\right)\right]^2}, \tag{5.16}$$

where N is the considered number of frames. While the model (see sec. 5.1.3) defines a set of parameters that need to be optimized, the validation was specifically performed on the gust ratio. In this way, it allows us to identify where the model

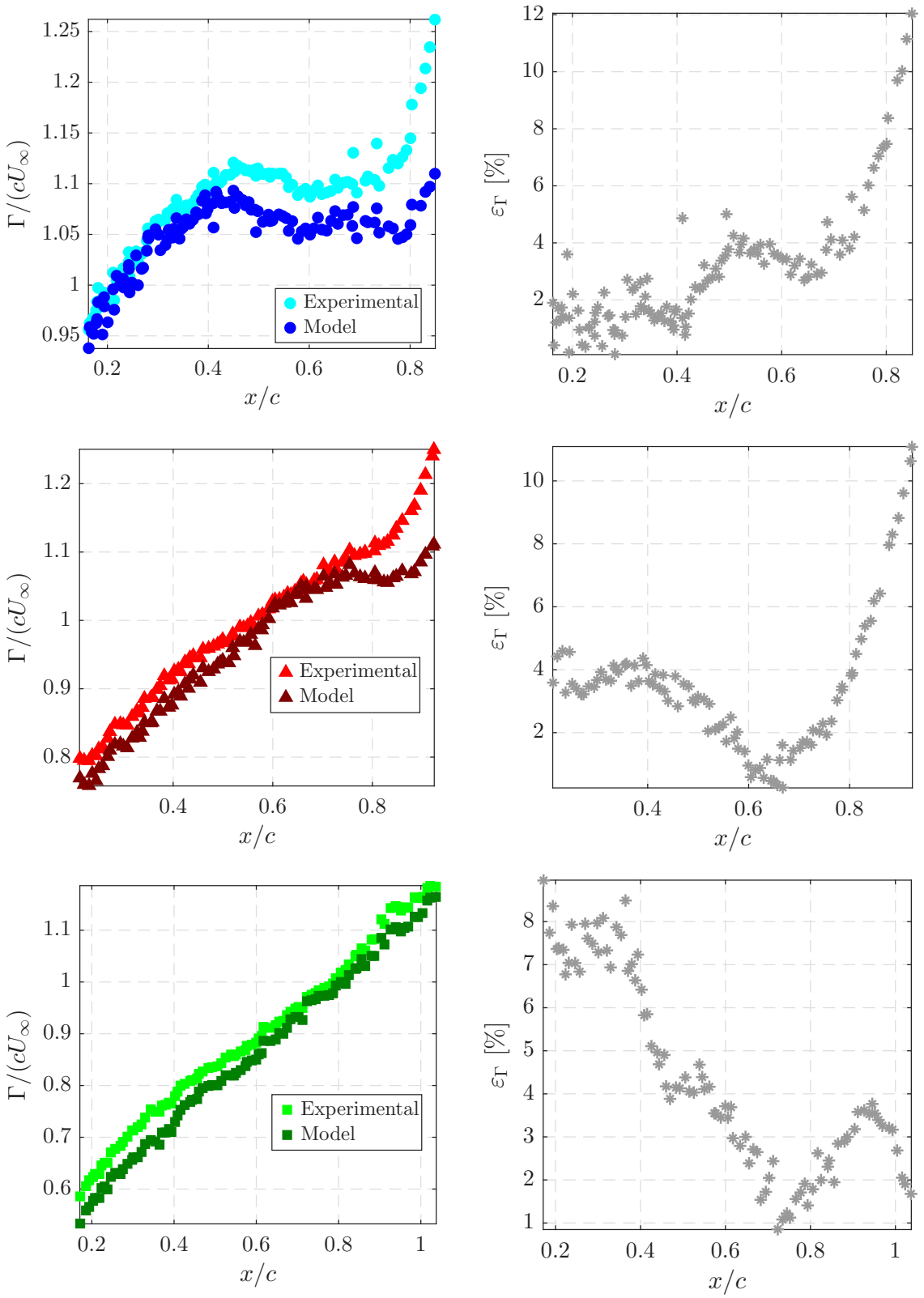


Figure 5.11: Evolution of non-dimensionalized circulation $\Gamma/(cU_\infty)$ and its relative error ε_Γ for the following speeds: $U_\infty \approx 1.0\,\mathrm{ms}^{-1}$ (●, ●), $U_\infty \approx 1.4\,\mathrm{ms}^{-1}$ (▲, ▲) and $U_\infty \approx 1.8\,\mathrm{ms}^{-1}$ (■, ■).

fits well experimental data. The RMSE calculated for the three analyzed cases is reported in tab. 5.3.

To provide additional insights, the relative error between experimental and numerical data was computed. The results are reported in fig. 5.12 as a function of the non-dimensional vortex center position x/c, for all experiments. The model performs well when the vortex core lies within the field of view (FOV), while its accuracy decreases when the vortex is located near the boundaries of the domain, where larger relative errors are observed. Similarly, the model shows increased relative errors in regions where the effects of the vorticity induced by the leading-edge shed vortex. This fact is due to the model, which is not able to capture it. At the characterization point (i.e., $x/c = 0.6$), the relative percentage error remains below 4 % in all three cases analyzed, confirming the good reliability of the model in this region.

Table 5.3: RMSE for the different analyzed inflow conditions.

	$U_\infty\,[\mathrm{ms}^{-1}]$	$\widetilde{GR}$
Test case 1	1.0	4.58×10^{-2}
Test case 2	1.4	4.50×10^{-2}
Test case 3	1.8	5.03×10^{-2}

5.3 Vortex-aerodynamic surface interaction

Once the characterization of the isolated vortex gust has been made, a pressure acquisition system was placed downstream of the vortex gust generator (in fig. 3.9 is sketched the set-up for the second part of the experimental campaign). To examine the aerodynamic impact of the vortex gust with the boundary layer, five pressure transducers were mounted underneath the aerodynamic surface and properly synchronized with the Event-Based cameras. This built-in setup allows to acquires simultaneously EBIV data, pressure data and the encoder signal (i.e., the exact position of the gust generator during its motion). In this way, it is possible to finely get what is going on from a physical and quantitative perspective.

5.3.1 Data post-processing

The raw voltage signals acquired by the five pressure transducers were first corrected by subtracting a sensor-specific offset. The differential signals were then converted in Pascal, yielding the time-resolved pressure traces $\Delta p_s(t)$ for each sensor $s = 1, \ldots, 5$, the position of which is reported in tab. 3.1.

Since the vortex gust generator repeats the same motion cycle for each realisation, the pressure response measured at the sensors is expected to be repeatable as well, and a phase-averaging procedure can therefore be applied to extract the deterministic signal. The DAQ index arrays, previously determined from the encoder

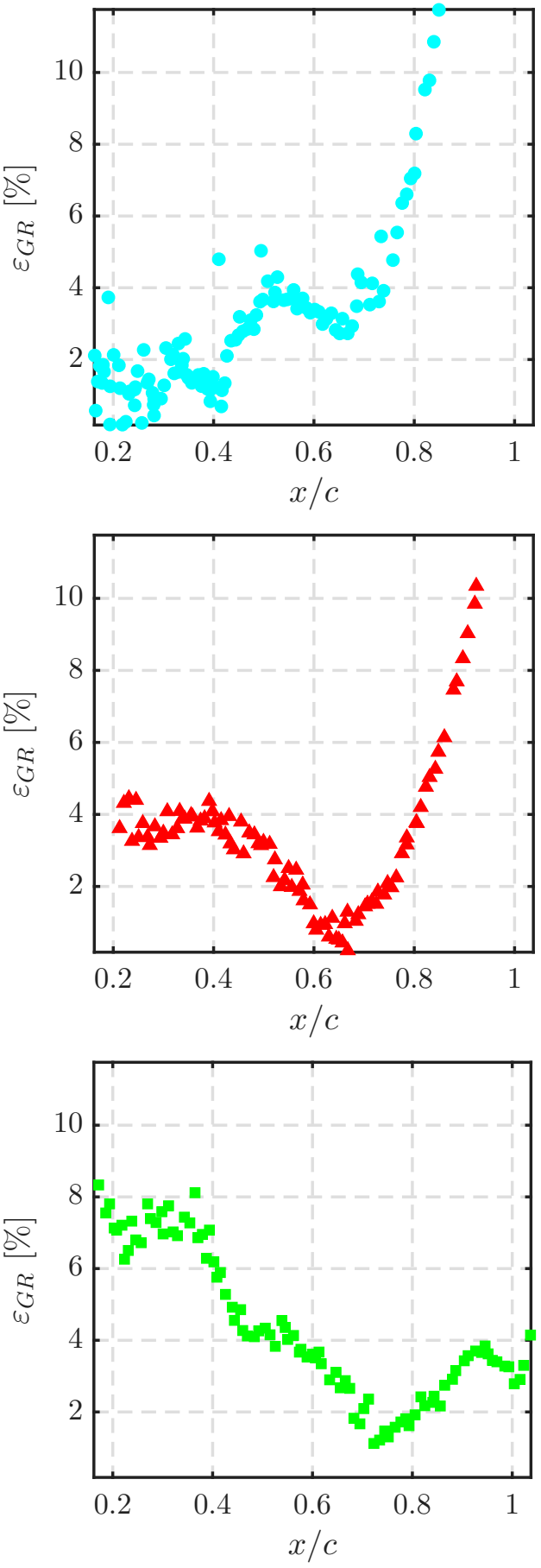


Figure 5.12: Relative error for gust ratio computed for $U_\infty \approx 1.0\,\mathrm{ms}^{-1}$ (●), $U_\infty \approx 1.4\,\mathrm{ms}^{-1}$ (▲) and $U_\infty \approx 1.8\,\mathrm{ms}^{-1}$ (■).

signal, were used to extract the pressure samples corresponding to each passage of the vortex, associating every physical front to its correct phase within the cycle.This procedure yielded, for each sensor, a set of 20 realisations of the pressure history, one per vortex passage.

The pressure signals were sampled by the Arduino at 1 KHz; however the resulting timestamps are not perfectly uniform. Each realisation was therefore resampled onto a common relative time grid at 500 Hz through linear interpolation, matching the same laser pulse frequency so that pressure samples and EBIV frames are perfectly synchronized. The origin $t = 0$ corresponds to the instant at which the vortex gust generator begins its rotation, which coincides with the first acquired frame and the first pressure sample of each realisation.

The phase-averaged pressure at each sensor $s = 1, \ldots, 5$ and at each time grid point t_i is computed as the arithmetic mean of the $N_v = 20$ vortex passages

$$\Delta\overline{p}_s(t_i) = \frac{1}{N_v} \sum_{k=1}^{N_v} \Delta p_s^{(k)}(t_i), \tag{5.17}$$

where $\Delta p_s^{(k)}(t_i)$ denotes the offset-corrected pressure of the k-th vortex passage at sensor s, and $i = 1, \ldots, N_t$ indexes the points of the uniform grid at 500 Hz.

Following the same logic, the standard deviation was then computed for each grid point as follows

$$\sigma_s(t_i) = \sqrt{\frac{1}{N_v - 1} \sum_{k=1}^{N_v} \left[\Delta p_s^{(k)}(t_i) - \Delta\overline{p}_s(t_i)\right]^2}, \tag{5.18}$$

The physical time axis was then non-dimensionalised into a convective time coordinate $t^* = U_\infty\, t/c$, where U_∞ is the free-stream velocity and $c = 0.3\,\mathrm{m}$ is the chord length of the gust generator.

The phase-averaged pressure (5.17) was normalised by the free-stream dynamic pressure to obtain the pressure coefficient for each sensor

$$c_p(t_i^*) = \frac{\Delta\overline{p}_s(t_i^*)}{\frac{1}{2}\rho U_\infty^2}, \tag{5.19}$$

and then the standard deviation, which was obtained from eq. 5.18 as follows

$$\sigma_{c_p}(t_i^*) = \frac{\sigma_s(t_i^*)}{\frac{1}{2}\rho U_\infty^2}. \tag{5.20}$$

After that, the eq. (5.19) was integrated spatially over the five sensor locations using the composite Simpson rule. Given the five uniformly spaced chord-wise positions x_s/c with spacing $\Delta(x/c) = 0.05$ (see tab. 3.1), the spatial integral at each convective time t_i^* is

$$\begin{aligned} \langle C_p(t_i^*)\rangle &= \int_{x_1/c}^{x_5/c} c_p\,(t_i^*)\,\mathrm{d}\left(\frac{x}{c}\right) \\ &\approx \frac{\Delta(x/c)}{3} \sum_{s=1}^{5} w_s\, c_p\,(t_i^*) \end{aligned} \tag{5.21}$$

where $w_s = [1, 4, 2, 4, 1]$ is the vector that contains weights for each sensor. The associated uncertainty propagated linearly as follows

$$\sigma_{\langle C_p \rangle}(t_i^*) = \sqrt{\sum_{s=1}^{5} \left(\frac{\Delta(x/c)}{3} w_s \right)^2 \sigma_{c_p}^2(t_i^*)}. \tag{5.22}$$

To isolate the perturbation induced by the vortex gust from the baseline pressure state, the eq. (5.21), (5.22) were normalised by the value at the initial instant defined as $C_{p_0} = \langle C_p(t^* = 0) \rangle$, yielding

$$\frac{\Delta C_p(t_i^*)}{C_{p_0}} = \frac{\langle C_p(t_i^*) \rangle - C_{p_0}}{C_{p_0}}, \tag{5.23}$$

$$\sigma(t_i^*) = \frac{\sigma_{\langle C_p \rangle}(t_i^*)}{|C_{p0}|}. \tag{5.24}$$

Since the vortex trajectory is not rectilinear (it moves in both x and y), a simple linear fit of x_c/c vs t^* only captures the streamwise component and underestimates the true convective speed. Instead, it is computed as a mean convective velocity over the whole trajectory, using the cumulative arc length traveled by the vortex core divided by the total convective time elapsed:

$$\frac{U_c}{U_\infty} = \frac{s_{\text{tot}}}{t^*_{\text{end}} - t^*_{\text{start}}}, \tag{5.25}$$

where where s_{tot} is the curvilinear abscissa computed by summing the Euclidean distances between consecutive trajectory points

$$s_{\text{tot}} = \sum_{i=1}^{N} \sqrt{\Delta \left(\frac{x_c}{c} \right)_i^2 + \Delta \left(\frac{y_c}{c} \right)_i^2}.$$

5.3.2 Results

Figures 5.13, 5.14, and 5.15 show the normalized pressure response measured by each of 5 sensors during the vortex gust encounter. The results are presented for several gust ratios derived from the flow characterization (see Table 5.2). These figures are obtained as described above in Sec. 5.3.1 and the reference equations are (5.17)-(5.20). The x axis shows the convective time, i.e., chord lengths traveled by the vortex. As mentioned before, the images and pressure sampling are synchronized; so that $t^* = 0$ corresponds to the moment in which the vortex gust generator begins its motion.

Fig. 5.16 shows the normalized pressure coefficient spatially integrated, where the reference equations are (5.21)-(5.24). The x axis shows the convective time. The results are presented for several gust ratios. Before the vortex gust encounters the aerodynamic surface, the $\Delta C_p/C_{p_0}$ experiences an absolute maximum: the value of which decrease as the gust ratio increase. Note that this peak value does have a strong dependence on the freestream velocity as well for the cases investigated here. To better understand the general behavior, all absolute and local maxima have been selected and analyzed across all investigated cases within $0.35 < t^* < 1.37$.

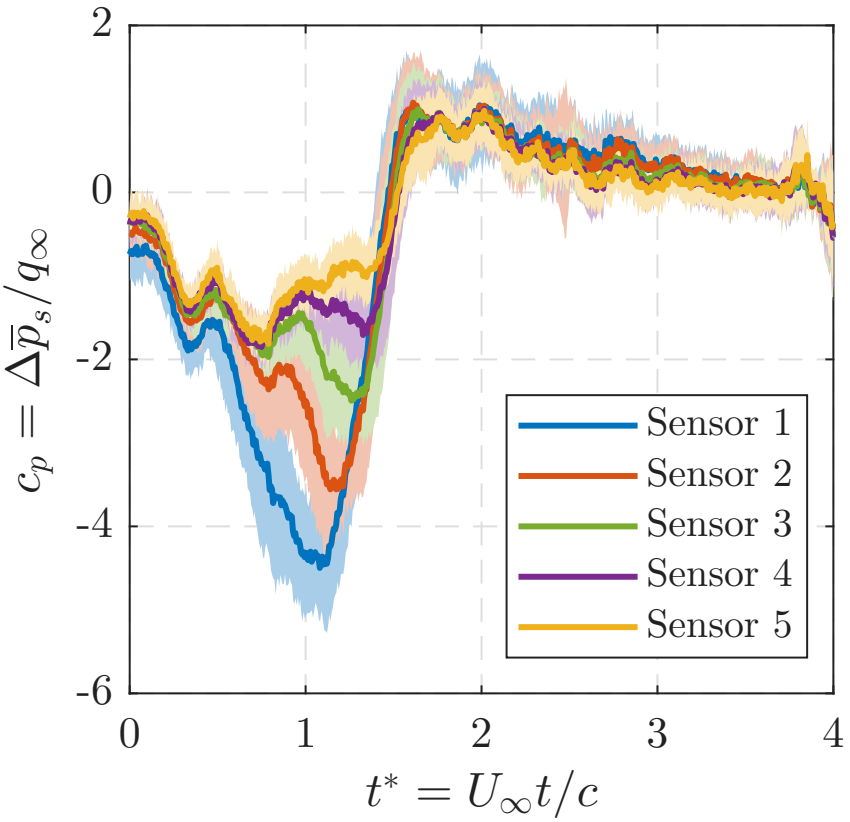


Figure 5.13: Pressure coefficient $c_p(t^*)$ for gust ratios $GR_{\text{exp}}(\vartheta) = 1.295$.

Regarding the initial evolution of the pressure coefficient, the first local maxima for each of the three gust ratios can be identified chronologically in fig. 5.16 at $t^* \approx 0.35$, $t^* \approx 0.49$, and $t^* \approx 0.69$, respectively. Physically, these early peaks are fundamentally driven by the upstream induced velocity field of the approaching vortex gust. As the gust approaches the aerodynamic surface, it causes a progressive upwash that locally tilts the flow streamlines. This streamline curvature induces a significant local increase in the effective angle of attack (AoA), which in turn yields a transient rise in the integrated pressure coefficient before the core interaction occurs. To quantitatively evaluate the transient orientation of the incoming flow at the leading edge (LE) of the flat plate, the effective local angle of attack (α_{LE}) is tracking-calculated at each convective time instant t^*. First, a localized physical control window is established, centered at the following reference coordinates $x/c = 0.62$ and $y/c = -0.45$. The size of this interrogation area is defined by a non-dimensional semi-width of $0.02c$, resulting in a total bounding box of $0.04c \times 0.04c$. This spatial window captures a localized subset of the PIV grid nodes surrounding the target point. To guarantee a robust estimation and filter out high-frequency experimental noise inherent to individual PIV grid vectors, a spatial averaging procedure is implemented. Crucially, the calculation relies strictly on the original, absolute velocity fields, ensuring that the true total flow orientation is captured. The instantaneous velocity components within the control box are obtained as:

$$\bar{U}_{LE}(t^*) = \frac{1}{N} \sum_{i,j \in \text{box}} \bar{U}(i,j,t^*),$$

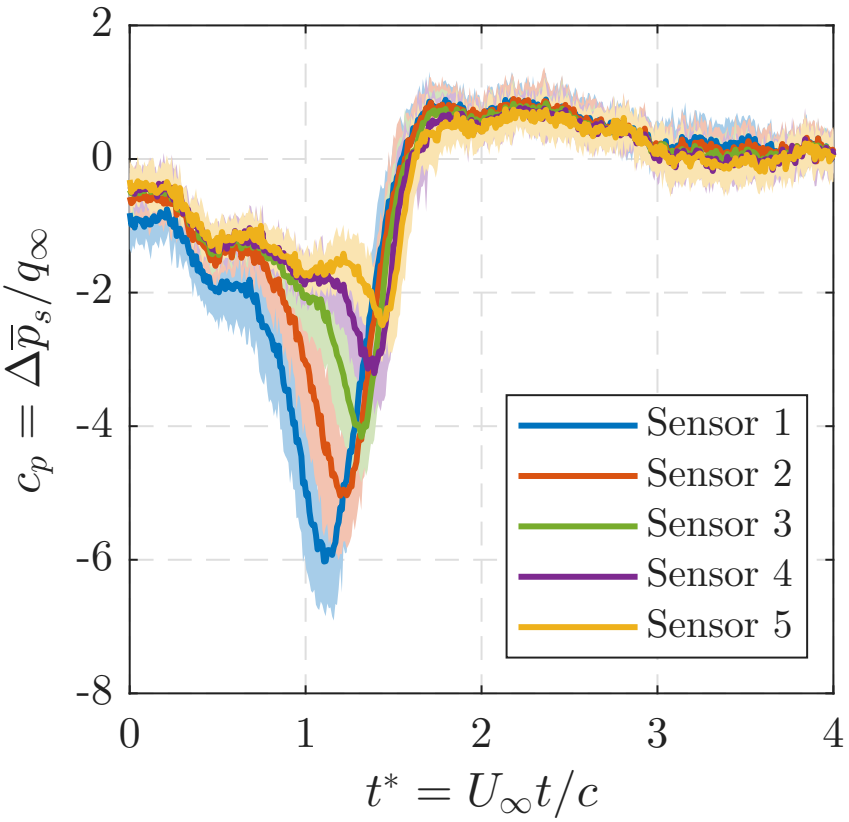


Figure 5.14: Pressure coefficient $c_p(t^*)$ for gust ratios $GR_{\text{exp}}(\vartheta) = 1.197$.

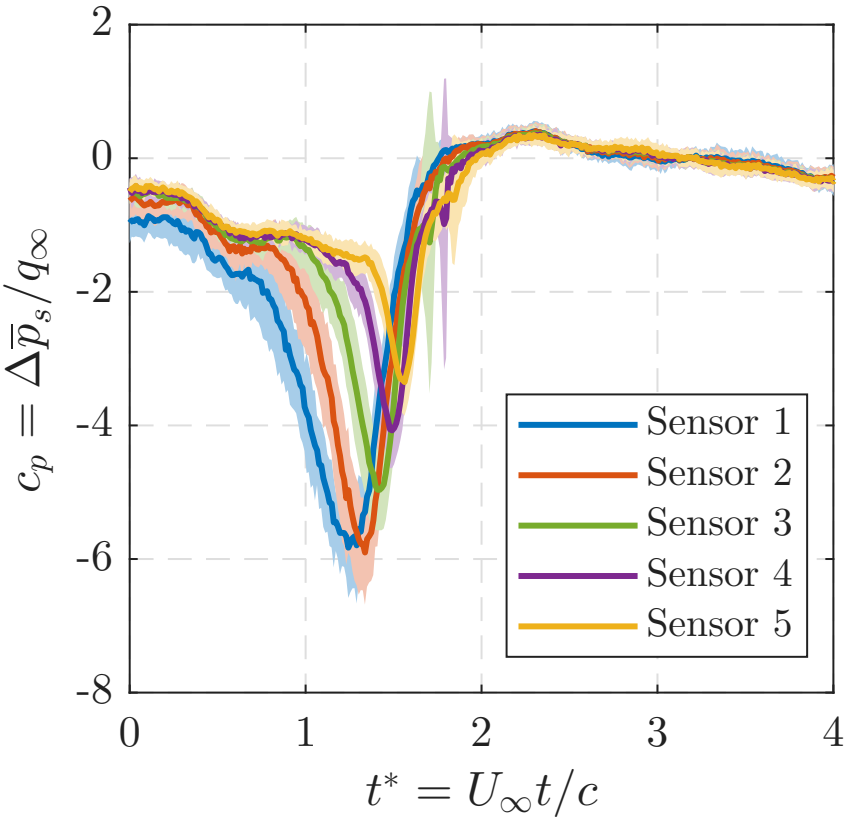


Figure 5.15: Pressure coefficient $c_p(t^*)$ for gust ratios $GR_{\text{exp}}(\vartheta) = 1.003$.

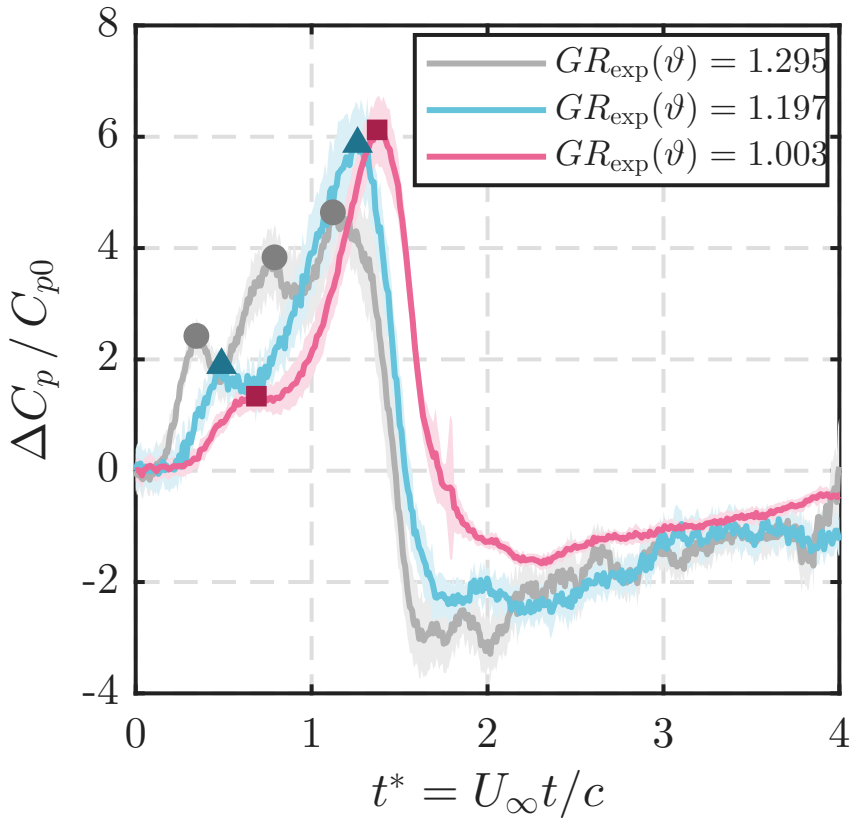


Figure 5.16: Normalized pressure coefficient $\Delta C_p(t^*)/C_{p_0}$ for various gust ratios. The markers (●, ▲, ■) represents the absolute and local maximum values for each of gust ratios.

$$\bar{V}_{LE}(t^*) = \frac{1}{N} \sum_{i,j \in \text{box}} \bar{V}(i,j,t^*),$$

where N represents the total number of valid PIV nodes within the designated window. Finally, the effective instantaneous local angle of attack is computed in degrees via the four-quadrant inverse tangent formulation:

$$\alpha_{LE}(t^*) = \text{atan2}\left(\bar{V}_{LE}(t^*), \bar{U}_{LE}(t^*)\right) \times \frac{180}{\pi}.$$

By applying this methodology to the investigated configurations, a local upwash effect is quantified across all test cases. The results are summerized in the following tab. 5.4.

The non-monotonic trend in α_{LE} arises because $\bar{V}_{LE}$ and $\bar{U}_{LE}$ do not scale at the same rate across test cases: from Test 1 to Test 2, $\bar{U}_{LE}$ increases by 62% while $\bar{V}_{LE}$ increases by only 50%, lowering the ratio and hence α_{LE}, whereas from Test 2 to Test 3 the opposite occurs, with $\bar{V}_{LE}$ growing by 44% against a 30% increase in $\bar{U}_{LE}$, pushing α_{LE} back up despite the lower nominal gust ratio. This indicates that the local induced velocity near the leading edge is not simply proportional to GR_{exp}, but also depends on how closely and how strongly the vortex core interacts with the plate at the specific instant of the pressure peak.

To obtain additional insight into the pressure coefficient response, the flow fields are also examined. The presence of a secondary local peak in the pressure coefficient,

Table 5.4: Summary of the first local pressure coefficient peaks and corresponding maximum effective local angle of attack at the leading edge.

	Test 1	**Test 2**	**Test 3**
GR_{exp}	1.295	1.197	1.003
$\Delta C_p(t^*)/C_{p_0}$	2.42	1.89	1.33
t^*	0.35	0.49	0.69
$\alpha_{LE}\,[^\circ]$	29.82	27.70	30.42
$\bar{U}_{LE}\,[\text{ms}^{-1}]$	0.77	1.25	1.62
$\bar{V}_{LE}\,[\text{ms}^{-1}]$	0.44	0.66	0.95

visible only for Test case 1 in 5.16 ($t^* = 0.79$), can be justified by examining the differences in the vortex trajectories. In the first configuration, the vortex follows a lower vertical path (y_c/c) compared to the other two configurations. Due to this proximity to the wall, the vortex core early on starts to strongly interact with the recirculation bubble formed at the leading edge of the aerodynamic surface. This intense interaction alters the local pressure distribution, generating the secondary relative peak before the main core impact that can be seen from fig. 5.17 as well.

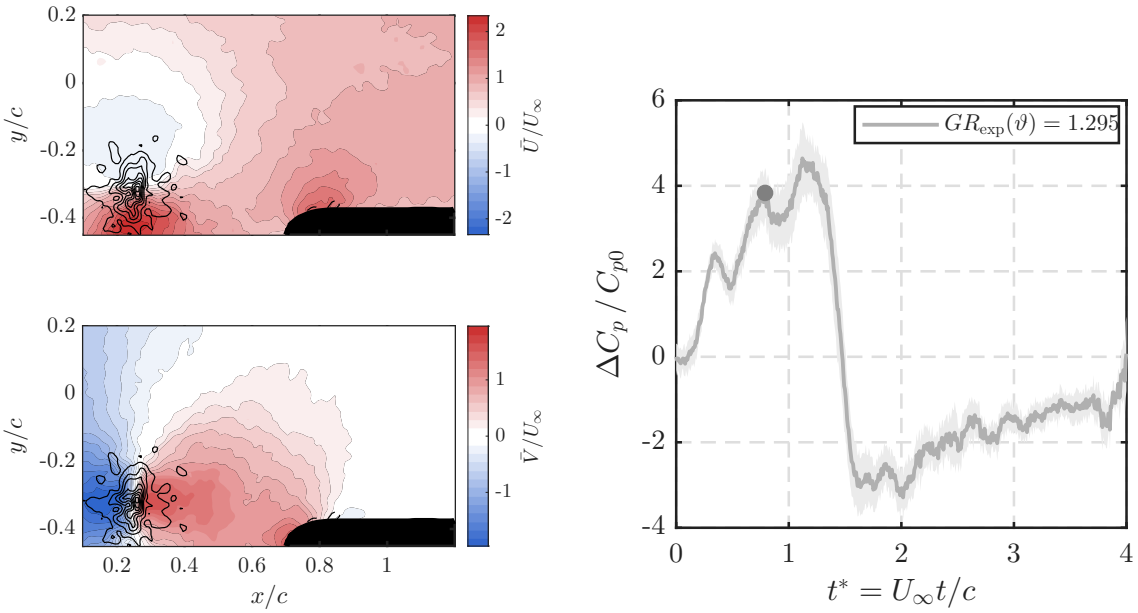


Figure 5.17: Slice of $\bar{U}/U_\infty$ and $\bar{V}/U_\infty$ (left) for $GR_{\text{exp}} = 1.295$ at $t^* = 0.79$. Black solid and dashed lines are isolines of positive and negative vorticity ($\omega c/U_\infty$), respectively. It is possible to visualize the vorticity due to the recirculation bubble; its interaction with the vortex core is the physical cause for the second local peak of the integrated pressure coefficient.

In contrast, for Test case 2 and Test case 3, the vortex is generated at a higher vertical

position (y_c/c) and maintains a more rectilinear trajectory as it moves downstream. Because of this larger vertical clearance, the vortex core remains structurally isolated from the surface boundary layer during the initial stages of the approach. The absence of a premature interaction with the leading-edge separation bubble prevents the formation of a secondary relative peak in these two configurations.

Having characterized the initial transient evolution and the physical mechanisms driving the first local pressure spikes, the analysis now shifts toward the absolute maxima experienced by the pressure coefficient across the three investigated configurations.

Fig. 5.19 represents the results in terms of non-dimensionalised vorticity contour plot ($\omega c/U_\infty$) and non-dimensionalised velocity fields ($\bar{U}/U_\infty$, $\bar{V}/U_\infty$) for $GR_{\text{exp}} = 1.295$ at absolute peak at $t^* = 1.12$. At the specific time instant observed (the value of integrated pressure coefficient is $\Delta C_p(t^*)/C_{p_0} = 4.64$), the center of the vortex core is located at $x/c = 0.428$ and $y/c = -0.312$. Although the core has not yet reached the aerodynamic surface, the interaction between the velocity field induced by the vortex and the boundary layer clearly promotes the formation of a recirculation bubble.

Fig. 5.20 represents the results in terms of non-dimensionalised vorticity contour plot ($\omega c/U_\infty$) and non-dimensionalised velocity fields ($\bar{U}/U_\infty$, $\bar{V}/U_\infty$) for $GR_{\text{exp}} = 1.197$ at absolute peak at $t^* = 1.26$. At the specific time instant observed (the value of integrated pressure coefficient is $\Delta C_p(t^*)/C_{p_0} = 5.87$), the center of the vortex core is located at $x/c = 0.579$ and $y/c = -0.211$. In this configuration, the vortex trajectory has shifted further upward compared to the first case. Furthermore, due to the higher freestream velocity U_∞, the vortex core is located closer to the aerodynamic surface at this stage. As a result of this increased proximity and stronger induced velocity, the interaction with the boundary layer is significantly intensified, leading to a more developed and larger recirculation bubble.

Fig. 5.21 represents the results in terms of non-dimensionalised vorticity contour plot ($\omega c/U_\infty$) and non-dimensionalised velocity fields ($\bar{U}/U_\infty$, $\bar{V}/U_\infty$) for $GR_{\text{exp}} = 1.003$ at absolute peak at $t^* = 1.37$. At the specific time instant observed (the value of integrated pressure coefficient is $\Delta C_p(t^*)/C_{p_0} = 6.12$), the center of the vortex core is located at $x/c = 0.649$ and $y/c = -0.164$. In the third case, the vortex follows yet another trajectory that is both higher and more advanced downstream, which is directly attributed to the faster convection speed of the core. At this stage, the vortex interacts completely with the leading-edge separation bubble; as a result, the two fluid structures appear intensely mixed and fundamentally broken down.

As GR_{exp} decreases, the higher freestream velocity causes the vortex core to reach its peak interaction stage further downstream along the chord. Because the fluid structure must travel a greater physical distance before this critical point, the pressure peak naturally shifts to later non-dimensional time instants, resulting in higher values of t^*. Concurrently, the increase in the integrated pressure coefficient is due to the more downstream position of the vortex core, which places it closer to the aerodynamic surface and consequently intensifies the interaction with the wall.

The normalised convective velocity, U_c/U_∞, is found to be 0.67, 0.76, 0.72 for the three test cases respectively. The absence of a clear monotonic trend with GR_{exp} suggests that the convective velocity of the vortex is weakly sensitive to changes in gust ratio, unlike the vortex trajectory and the resulting pressure response.

The facility used for the vortex gust experiments allows to vary the gust ratio (i.e., the intensity) by modifying the wind tunnel freestream velocity. In Sec. 5.2 indeed it has been shown that the freestream velocity has a direct impact on the gust ratio $GR_{\text{exp}}(\vartheta)$ of the vortex gust. As it can be seen from Fig. 5.10 (bottom), the trajectories follow the same straight path. Since the rotation velocity of the gust generator is the same for all test cases, the freestream velocity has a direct impact on the vertical placement of the vortex core center. In fact, the higher is U_∞, the less the vortex is deflected downward. The aerodynamic trajectory indeed depends on the ratio $|V_{g,\max}|/U_\infty$ (see Tab. 5.2), which decreases with U_∞.

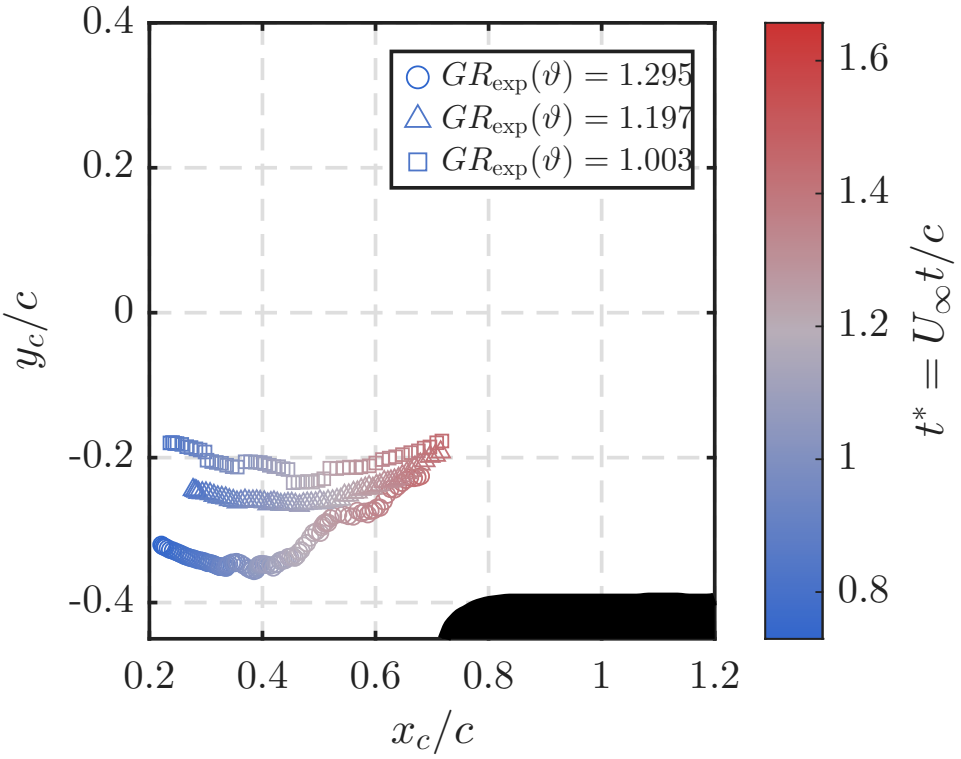


Figure 5.18: Paths of vortex gust for various gust ratios when it encounters an aerodynamic surface, where its leading edge is located at $\Delta y/c = -0.45$.

As mentioned earlier, the vortex gust is shed from the trailing edge of the gust generator plate due to the rotation that it undergoes. Thus, the presence of an aerodynamic surface placed downstream cause the vortex gust to follow different paths that depends on freestream velocity U_∞ and the vertical offset $\Delta y/c$, as it is showed in Fig. 5.18. As the vortex core approaches the plate, all three trajectories exhibit a marked upward curvature before reaching the leading edge, departing from the otherwise straight path observed further upstream. This behaviour is consistent with the influence of the vortex induced by the no-penetration condition at the wall: as the real vortex approaches the solid surface, the induced velocity field deflects the trajectory away from the surface, parallel to the wall. The effect is more pronounced for the lower U_∞ case, where the vortex core travels closer to the plate and therefore experiences a stronger deflection.

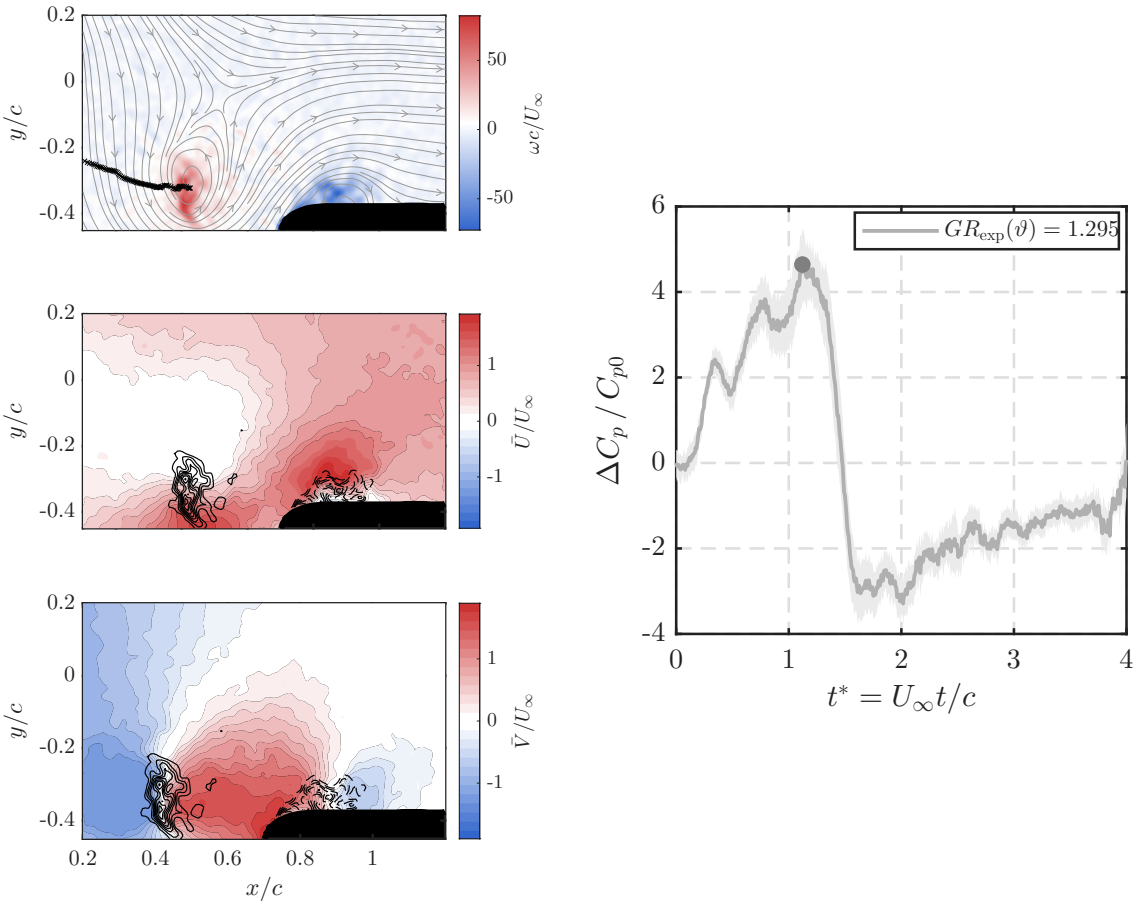


Figure 5.19: Normalized out of plane vorticity contourplots $\omega c/U_\infty$ and slice of $\bar{U}/U_\infty$ and $\bar{V}/U_\infty$ (left) for $GR_{\text{exp}} = 1.295$ at $t^* = 1.12$. Black solid and dashed lines are isolines of positive and negative vorticity, respectively.

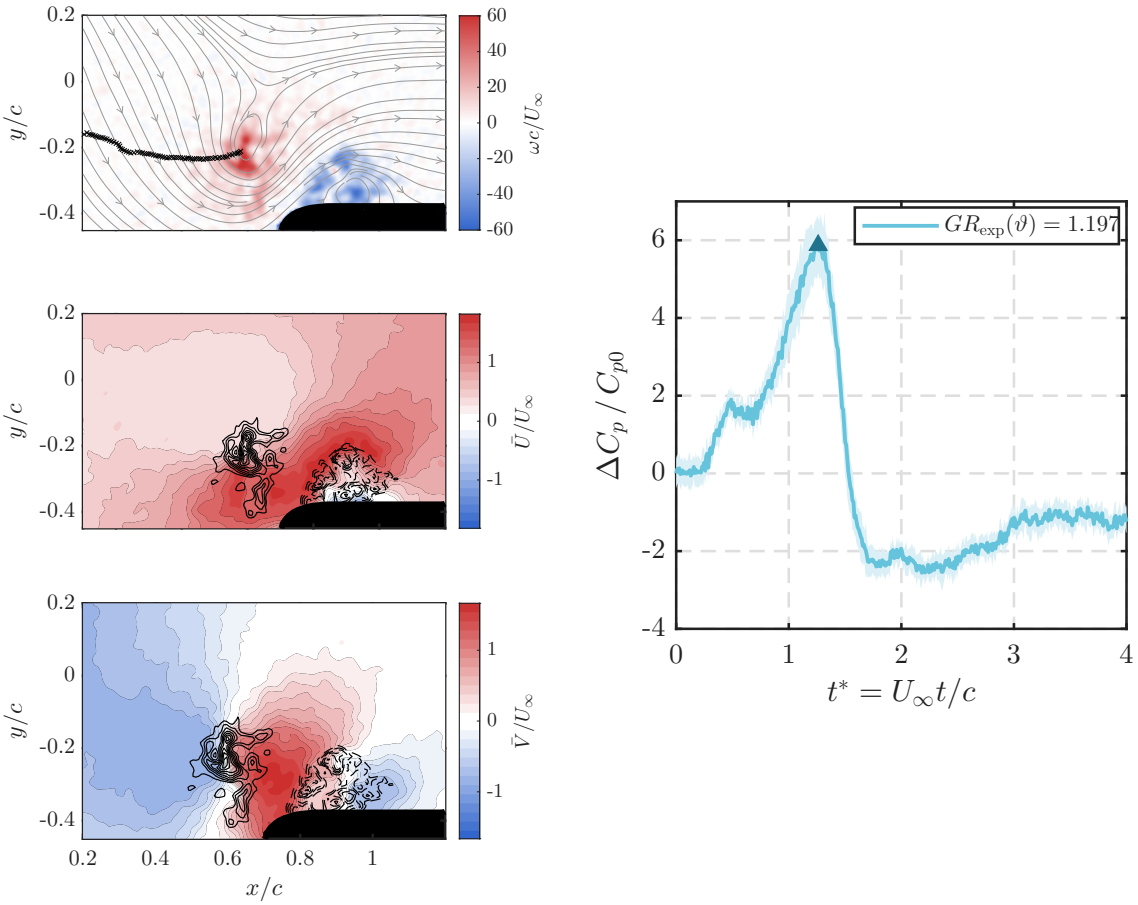


Figure 5.20: Normalized out of plane vorticity contourplots $\omega c/U_\infty$ and slice of $\bar{U}/U_\infty$ and $\bar{V}/U_\infty$ (left) for $GR_{\text{exp}} = 1.197$ at $t^* = 1.26$. Black solid and dashed lines are isolines of positive and negative vorticity, respectively.

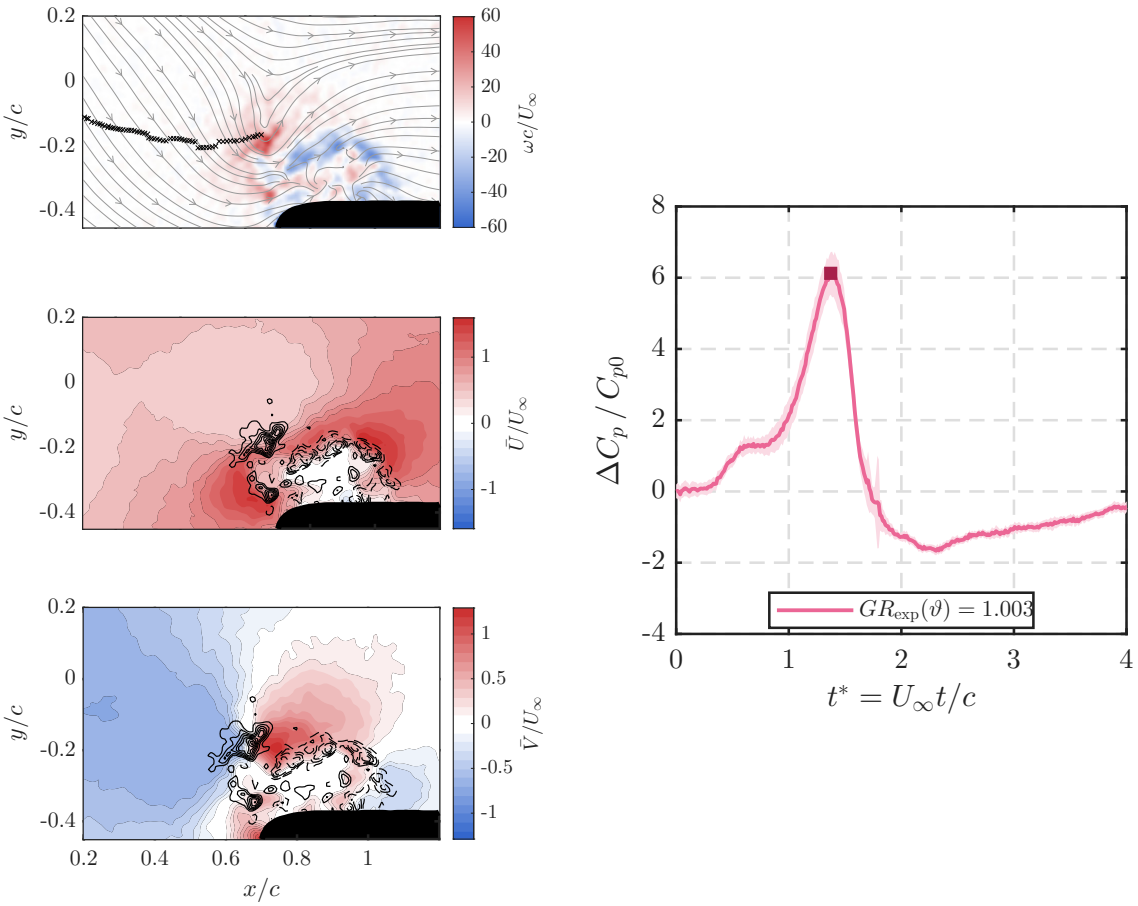


Figure 5.21: Normalized out of plane vorticity contourplots $\omega c/U_\infty$ and slice of $\bar{U}/U_\infty$ and $\bar{V}/U_\infty$ (left) for $GR_{\text{exp}} = 1.003$ at $t^* = 1.37$. Black solid and dashed lines are isolines of positive and negative vorticity, respectively.

Chapter 6

Conclusions

In this work, the development and experimental validation of a innovative build-in set-up in matter of experimental vortex gust generation and gust encounters has been presented and validated across different inflow conditions.

The primary contribution of this research lies in the development of an innovative experimental set-up engineered for wind tunnels, in order to fill the current gap in the literature. Furthermore, this built-in set-up introduce the capability of performing three synchronized measurements, which are the encoder signal (i.e., the precise state of the maneuver of the gust generator), the raw stream data of Event-Based cameras and pressure data.

The experimental campaign was conducted by varying the free-stream velocity across three different conditions ($U_\infty = 1$ m/s, 1.4 m/s, and 1.8 m/s), while keeping the rotation speed of the gust generator constant. In all investigated cases, highly severe aerodynamic conditions were successfully achieved, enabling the exploration of distinct gust ratios, respectively 1.295, 1.197, and 1.003. Achieving a gust ratio greater than unity represents a prominent experimental challenge.

This experimental platform not only expands simultaneous data acquisition capabilities but also ensures high repeatability of the experimental conditions. In this way, it has been made a phase-average of the experimental data.

On the analytical and post-processing front, the implementation of the elliptical Lamb-Oseen model proved highly effective, yielding excellent results for the characterization of the investigated fluid dynamic phenomena. The model was validated directly against the gust ratio and circulation, with an average error bounded between 6% and 8%. Nonetheless, some inherent limitations were identified: the model's predictive performance predictably degrades when the vortex approaches the boundaries of the Field of View (FOV). It neglects the vorticity effects due to the leading-edge vortex.

In conclusion, this work confirms the high potential of this innovative set-up for applications in highly non-uniform and severe conditions. Moving forward, future investigations will focus on providing a comprehensive quantitative explanation of the results obtained regarding the gust-boundary layer interaction on the aerodynamic surface. Keeping the gust ratio fixed, further experimental campaigns will explore different configurations by systematically varying the height of the downstream aerodynamic surface.

Bibliography

[1] Anya R. Jones, Oksan Cetiner, and Marilyn J. Smith. "Physics and Modeling of Large Flow Disturbances: Discrete Gust Encounters for Modern Air Vehicles". In: *Annual Review of Fluid Mechanics* 54 (2022). DOI: 10.1146/annurev-fluid-031621-085520.

[2] Anya R. Jones. "Gust encounters of rigid wings: Taming the parameter space". In: *Phys. Rev. Fluids* 5 (2020). DOI: 10.1103/PhysRevFluids.5.110513.

[3] Esteban A.L. Hufstedler and Beverley J. McKeon. "Vortical Gusts: Experimental Generation and Interaction with Wing". In: *AIAA Journal* (2019). DOI: 10.2514/1.J056914.

[4] Abdulghani Mohamed et al. "Gusts Encountered by Flying Vehicles in Proximity to Buildings". In: *Drones* 7 (2022). DOI: 10.3390/drones7010022.

[5] S. Mohr et al. "Statistical characteristics of convective wind gusts in Germany". In: *Natural Hazards and Earth System Sciences* 17.6 (2017). DOI: 10.5194/nhess-17-957-2017.

[6] Nikolajs Glizde. "Plotting the Flight Envelope of an Unmanned Aircraft System Air Vehicle". In: *Transport and Aerospace Engineering* 4 (2017). DOI: 10.1515/tae-2017-0010.

[7] Simon Watkins, J. Millbank, and B.Loxton. "Atmospheric Winds and their Effects on Micro Air Vehicles". In: *AIAA Journal of Aircraft* 44 (2006).

[8] Yonghonh Zhong et al. "Optimally time-dependent modes of vortex gust-airfoil interactions". In: *Journal of Fluid Mechanics* 1006 (2025). DOI: 10.1017/jfm.2025.9.

[9] Kai Fukami, Luke Smith, and Kunihiko Taira. "Extreme vortex-gust airfoil interactions at Reynolds number 5000". In: *Phys. Rev. Fluids* 10 (2025). DOI: 10.1103/vcbd-tvz1.

[10] Karen Mulleners, Peter Mancini, and Anya R. Jones. "Flow development on a flat-plate wing subjected to a streamwise acceleration". In: *AIAA Journal* 55.6 (2017). DOI: 10.2514/1.J055497.

[11] Flavio Noca et al. "Wind and Weather Facility for Testing Free-Flying Drones". In: *AIAA Journal* (2019). DOI: 10.2514/6.2019-2861.

[12] Anya R. Jones and Oksan Cetiner. "Overview of Unsteady Aerodynamic Response of Rigid Wings in Gust Encounters". In: *AIAA Journal* (2020). DOI: 10.2514/1.J059602.

[13] Hülya Biler, Girguis Sedky, and Anya R. Jones. "Experimental Investigation of Transverse and Vortex Gust Encounters at Low Reynolds Numbers". In: *AIAA Journal* 59.3 (2021). DOI: 10.2514/1.J059658.

[14] Kader Engin et al. "Large Scale Spanwise Periodic Vortex Gusts or Single Spanwise Vortex Impinging on a Rectangular Wing". In: *AIAA Journal* (2018). DOI: 10.2514/6.2018-3086.

[15] H. Dryden. "A Review of the Statistical Theory of Turbulence". In: *Quarterly of Applied Mathematics* (1943). DOI: 10.1090/qam/1943-01-01.

[16] T. von Karman. "Progress in the Statistical Theory of Turbulence". In: *Proceedings of the National Academy of Sciences* 34 (1948).

[17] JW Miles. *The Aerodynamic Force on an Airfoil in a Moving Gust: A Generalization of the Two-dimensional Gust Problem*. Douglas Aircraft Company, 1954.

[18] H. Kussner. "Summary Report on the Unsteady Lift of Wings". In: *Aeronautical Research* 13 (1936).

[19] T. von Karman and W. Sears. "Airfoil Theory for Non-Uniform Motion". In: *Journal of the Aeronautical Sciences* 5 (1938). DOI: 10.2514/8.674.

[20] H. Wagner. "On the Generation of Dynamic Lift of Aerofoils". In: *Journal of Applied Mathematics and Mechanics* 5 (1925). DOI: 10.1002/(ISSN)1521-4001.

[21] T. Theodorsen. "General Theory of Aerodynamic Instability and the Mechanism of Flutter". In: *NACA Annual Report* 20 (1935).

[22] Yuanzhi Qian, Zhijin Wang, and Ismet Gursul. "Interaction of quasi-two-dimensional vortical gusts with airfoils unswept and swept wings". In: *Experiments in Fluids* (2022). DOI: 10.1007/s00348-022-03477-8.

[23] Tong Wang et al. "Airfoil response to periodic vertical and longitudinal gusts". In: *J. Fluid Mech.* 979 (2024). DOI: 10.1017/jfm.2023.1000.

[24] Kunihiko Taira. "Extreme Aerodynamics: A Data-Driven Perspective". In: *Phys. Rev. Fluids* 11 (2026). DOI: 10.1103/8pr4-txmt.

[25] Guillermo Gallego et al. "Event-Based Vision: A Survey". In: *IEEE Transactions on Pattern Analysis and Machine Intelligence* 44.1 (2022). DOI: 10.1109/TPAMI.2020.3008413.

[26] Chiara Bartolozzi, Giacomo Indiveri, and Elisa Donati. "Embodied neuromorphic intelligence". In: *Nature Communications* 13 (2022). DOI: 10.1038/s41467-022-28487-2.

[27] Zaid El Shair and Samir Rawashdeh. "High-temporal-resolution event-based vehicle detection and tracking". In: *Optical Engineering* 62.3 (2022). DOI: 10.1117/1.oe.62.3.031209.

[28] Zhengfa Liu et al. "Mixed Event-Frame Vision System for Daytime Preceding Vehicle Taillight Signal Measurement Using Event-Based Neuromorphic Vision Sensor". In: *Journal of Advanced Transportation* 2022.1 (2022). DOI: https://doi.org/10.1155/2022/2673191.

[29] Guang Chen et al. "Neuromorphic Vision Based Multivehicle Detection and Tracking for Intelligent Transportation System". In: *Journal of advanced transportation* 2018 (2018). DOI: 10.1155/2018/4815383.

[30] Gioacchino Cafiero. *Aerodinamica Sperimentale*. Lecture notes. Politecnico di Torino, 2025.

[31] Christian Willert. "Event-based imaging velocimetry using pulsed illumination". In: *Experiments in Fluids* 64 (2023). DOI: 10.1007/s00348-023-03641-8.

[32] Christoph Posch et al. "Retinomorphic Event-Based Vision Sensors: Bioinspired Cameras With Spiking Output". In: *Proceedings of the IEEE* 102 (2014). DOI: 10.1109/JPROC.2014.2346153.

[33] Luca Franceschelli et al. "An assessment of event-based imaging velocimetry for efficient estimation of low-dimensional coordinates in turbulent flows". In: *Experimental Thermal and Fluid Science* 164 (2025). DOI: 10.1016/j.expthermflusci.2025.111425.

[34] Christian E. Willert and Joachim Klinner. "Event-based imaging velocimetry: an assessment of event-based cameras for the measurement of fluid flows". In: *Experiments in Fluids* 63 (2022). DOI: 10.1007/s00348-022-03441-6.

[35] Enrico Amico, Gioacchino Cafiero, and Gaetano Iuso. "Deep reinforcement learning for active control of a three-dimensional bluff body wake". In: *Physics of Fluids* 34 (2022). DOI: 10.1063/5.0108387.

[36] Fulvio Scarano et al. "On the use of helium-filled soap bubbles for large-scale tomographic PIV in wind tunnel experiments". In: *Experiments in Fluids* 56 (2015). DOI: 10.1007/s00348-015-1909-7.

[37] E. Amico et al. "Event-based versus particle image velocimetry for cardiac flow analysis in a left-heart simulator". In: *Physics of Fluids* 38 (2026). DOI: 10.1063/5.0315234.

[38] Daniela Tordella. *Flussi Turbolenti*. Lecture notes. Politecnico di Torino, 2025.

[39] David Fabre, Denis Sipp, and Laurent Jacquin. "Kelvin waves and the singular modes of the Lamb–Oseen vortex". In: *Journal of Fluid Mechanics* 551 (2006). DOI: 10.1017/S0022112005008463.

[40] Philip G. Saffman. *Vortex Dynamics*. Cambridge: Cambridge University Press, 1992. ISBN: 978-0521477390.